Appendix A Derivations

A.1 Kinetics of Electrode Reactions: Butler-Volmer Equation

In this section, a relationship between the potential of the electrode and resulting current is derived for a simple one-electron process. This derivation will serve as a basis for further understanding of observed kinetics in fuel cell electrodes.[41]

A simple one-electron transfer process occurring on the surface of an electrode can be represented as

$$\mathrm{O} + \mathrm{e}^- \underset{k_{ox}}{\overset{k_{red}}{\rightleftharpoons}} \mathrm{R} \tag{A.1}$$

where O represents the oxidized species, R is the reduced species, and k_{red} and k_{ox} are the reduction and oxidation rate constants, respectively. At the equilibrium or standard potential of the redox couple, denoted by E^0, the standard free energy profiles of the reactants and products are as shown in Figure A.1, where $\Delta G_{0c}^{\neq}$ and $\Delta G_{0a}^{\neq}$ represent the cathodic and anodic standard energies of activation, respectively. Changes in electrode potential are reflected by shifts in the free energy profile for O + e^-, and the intersection of the two profiles represents the transition state of the reaction. When the potential of the electrode is changed to E, the free energy of the electron on the electrode changes by $-F\Delta E$, where $\Delta E = E - E^0$. This change is depicted as a shift in the energy profile for O + e^-, downward in this case. At this new state, the barriers for reduction and oxidation are denoted by $\Delta G_c^{\neq}$ and $\Delta G_a^{\neq}$, respectively. Notice that $\Delta G_c^{\neq} > \Delta G_{0c}^{\neq}$ and $\Delta G_a^{\neq} > \Delta G_{0a}^{\neq}$. It can be seen that the barrier for reduction increases by an amount that is a fraction α of the total energy change, while the barrier for oxidation decreases. The new activation barriers are given by

$$\Delta G_c^{\neq} = \Delta G_{0c}^{\neq} + \alpha F\left(E - E^0\right) \tag{A.2}$$

$$\Delta G_a^{\neq} = \Delta G_{0a}^{\neq} - \left(1-\alpha\right) F\left(E - E^0\right) \tag{A.3}$$

where α, the transfer coefficient, gives an indication of the fraction of the potential that assists the reaction. In most cases, α lies between 0.3 and 0.7 but is often approximated as 0.5 in the absence of measurements.[41] Equations (A.2) and (A.3) can be related to rate constants k_{red} and k_{ox} by assuming the rate constants have Arrhenius form,

$$k_{red} = A_{red}\exp\left(-\frac{\Delta G_c^{\neq}}{RT}\right) \tag{A.4}$$

$$k_{ox} = A_{ox}\exp\left(-\frac{\Delta G_a^{\neq}}{RT}\right) \tag{A.5}$$

where A_{red} and A_{ox} are pre-exponential factors. Equations (A.2) and (A.3) are inserted into equations (A.4) and (A.5), respectively, to obtain

$$k_{red} = A_{red}\exp\left(-\frac{\Delta G_{0c}^{\neq}}{RT}\right)\exp\left[-\frac{\alpha F\left(E-E^0\right)}{RT}\right] = k^0\exp\left[-\frac{\alpha F\left(E-E^0\right)}{RT}\right] \tag{A.6}$$

$$k_{ox} = A_{ox}\exp\left(-\frac{\Delta G_{0a}^{\neq}}{RT}\right)\exp\left[\frac{\left(1-\alpha\right) F\left(E-E^0\right)}{RT}\right] = k^0\exp\left[\frac{\left(1-\alpha\right) F\left(E-E^0\right)}{RT}\right] \tag{A.7}$$

where k^0 is the standard rate constant, defined for the case when the interface is equilibrated, $E = E^0$, with an environment in which $C_{\mathrm{O}}^* = C_{\mathrm{R}}^*$. k^0 is a measure of the how facile the reaction kinetics are, i.e., how fast this couple will achieve equilibrium. The net current density ($j = i/A$) for the process is

$$j = j_c - j_a = Fk_{red}C_{\mathrm{O}}(0,t) - Fk_{ox}C_{\mathrm{R}}(0,t) \tag{A.8}$$

$$j = Fk^0\left[C_{\mathrm{O}}(0,t)\exp^{-\alpha F\left(E-E^0\right)/RT} - C_{\mathrm{R}}(0,t)e^{(1-\alpha)F\left(E-E^0\right)/RT}\right] \tag{A.9}$$

where A is the electrode area, and $C_{\mathrm{O}}(0,t)$ and $C_{\mathrm{R}}(0,t)$ refer to concentrations at the electrode surface.

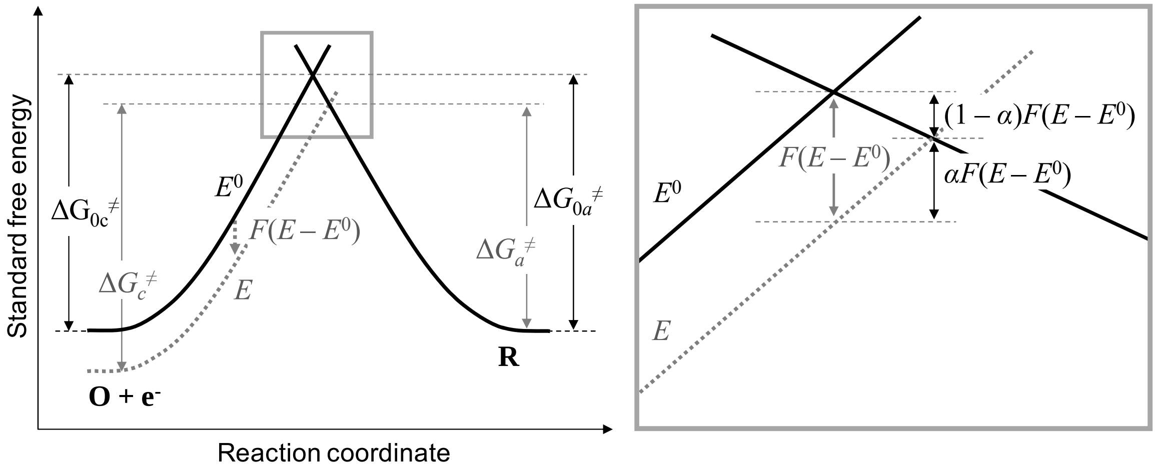

Figure A.1 The effect of potential change on the standard free energy profiles for the reaction, $\mathrm{O} + \mathrm{e}^- \rightleftharpoons \mathrm{R}$.

At equilibrium (E = E_{eq}), the net current is zero, and the surface concentrations are the same as the bulk concentrations, C_{O}^* and C_{R}^* . Equation (A.9) simplifies to the Nernst equation, and the equilibrium potential is related to the standard potential by the concentrations of the species involved.

$$E_{eq} = E^0 + \frac{RT}{F}\ln\frac{C_{\mathrm{O}}^*}{C_{\mathrm{R}}^*} \tag{A.10}$$

The exchange current density, defined as the forward and reverse current densities ($j_0 = j_a = j_c$) at equilibrium, can be expressed in terms of the standard rate constant and the bulk concentrations.

$$j_0 = Fk^0 C_{\mathrm{O}}^{*(1-\alpha)} C_{\mathrm{R}}^{*\alpha} \tag{A.11}$$

The exchange current density, similar to k^0, indicates how likely it is for the reaction to occur in either direction. To obtain a more useful current-overpotential relationship, Equation (A.11) can be used to express Equation (A.9) in terms of the equilibrium potential rather than the standard potential.

$$j = j_0 \left[\frac{C_{\mathrm{O}}(0,t)}{C_{\mathrm{O}}^*} e^{-\alpha\eta F/RT} - \frac{C_{\mathrm{R}}(0,t)}{C_{\mathrm{R}}^*} e^{(1-\alpha)\eta F/RT} \right] \tag{A.12}$$

If mass transfer is not rate limiting, e.g., when convection is high, the surface and bulk concentrations are the same and

$$j = j_0 \left[e^{-\alpha\eta F/RT} - e^{(1-\alpha)\eta F/RT} \right] \tag{A.13}$$

Equation (A.13), historically known as the Butler-Volmer equation, describes the relationship between the overpotential, $\eta = E - E_{eq}$, needed to drive the reaction and the resulting current.

The importance of j_0 can be seen when the Butler-Volmer equation is plotted for various values of j_0. (Figure A.2) For a small j_0, significant current will not flow unless a large overpotential is applied. This can be understood intuitively as well; the exchange current indicates how likely it is for the reaction to occur in either direction. The most effective way to improve the activation overpotential is to increase j_0. This is accomplished by choosing an active catalyst, followed by increasing the electrode roughness or surface area. Improving catalyst site occupancy by increasing reactant concentration or pressure is also possible. For a system that obeys Butler-Volmer kinetics, the slope near the origin provides information about the exchange current and therefore the relative activities of different electrode materials.

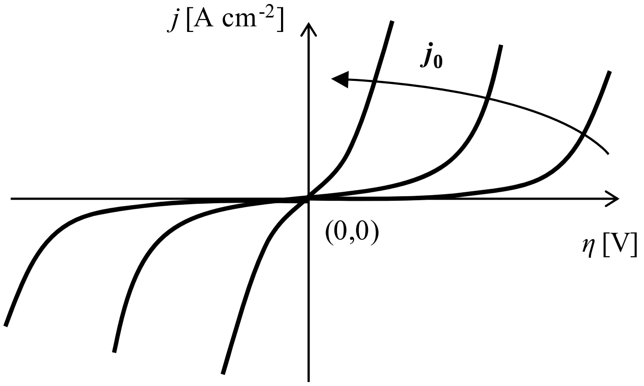

Figure A.2 Effect of exchange current on the current-overpotential behavior.

In low-temperature fuel cells, reaction kinetics are slow and large activation overpotentials are needed at both electrodes. In such systems, the Tafel equation is more useful. The Tafel equation, first introduced empirically, can be obtained from the Butler-Volmer equation. At high positive or negative η, either j_a or j_c can be neglected. For example, at large negative overpotentials,

$$j = j_0 e^{-\alpha\eta F/RT} \tag{A.14}$$

or

$$\eta_{act} = \frac{RT}{\alpha F} \ln\left(\frac{j_0}{j}\right) \tag{A.15}$$

It is common to modify the Tafel equation for a system in which more than one electron is transferred, i.e., $n > 1$ where n denotes the number of electrons transferred in the redox reaction.

$$\eta_{act} = \frac{RT}{n\alpha F}\ln\left(j_0\right) - \frac{RT}{n\alpha F}\ln\left(j\right) \tag{A.16}$$

Experimental data obtained at high overpotentials plotted in the form of ln(j) as a function of η yields a line from which n or α (slope) and j_0 (intercept) can be calculated.

A.2 Finite-Length Warburg with Reversible Bounds

In this section, we will derive the impedance expression for the finite-length Warburg element (Equation 3.1) used to analyze the impedance response of the Pt thin film electrode system. This section is based on derivations in the references, Orazem & Tribollet[33] and Franceschetti & MacDonald.[123] The Pt thin film system can be generalized as shown in Figure A.3 for a electrolyte | metal | gas system, in which a neutral species, A, enters the metal at the metal | gas interface ($x = L$) and diffuses a distance L to the metal | electrolyte interface ($x = 0$) where it is electrochemically oxidized,

$$\mathrm{A}_{(met)} \rightleftharpoons \mathrm{A}^{n+}{}_{(lyte)} + n\mathrm{e}^{-}{}_{(met)} \tag{A.17}$$

In the charge transfer reaction, (A.17), n denotes the number of electrons transferred and, therefore, also the charge of the ionic species, A^{n+}, formed in the electrolyte. "*met*" and "*lyte*" denote that metal and electrolyte phases, respectively. We assume in this system, that supply of A at the metal | gas interface and charge transfer kinetics at the electrolyte | metal interface are fast relative to diffusion.

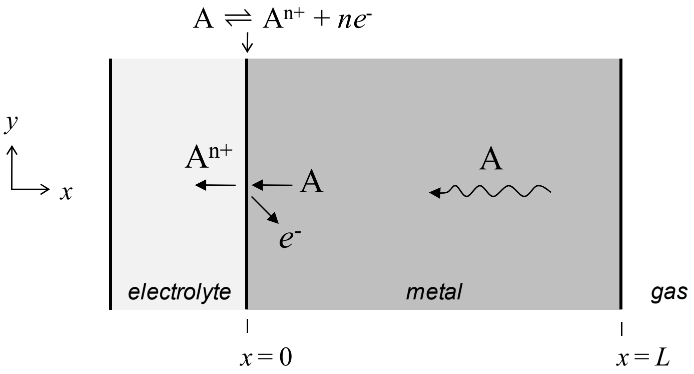

Figure A.3 Diffusion of a neutral species, A, through a metal film of finite thickness, L, to be oxidized at $x = 0$ via the charge transfer reaction A $\rightleftharpoons$ $A^{n+} + ne^-$.

The movement of chemical species under an electrochemical potential gradient is described be the Nernst-Planck equation, which, in general is given by

$$J_k = -D_k \nabla c_k + \frac{\sigma_k}{z_k F} \nabla \phi \tag{A.18}$$

where J_k denotes the flux of species k under both a concentration gradient, ∇c_k, and an electric potential gradient, $\nabla \phi$. D_k is the diffusivity, σ_k is the conductivity and z_k is the charge of the species k. F, R, and T have their usual meanings. In general, for the transport of a chemical species in any medium, the second (migration) term in Equation (A.18) can be neglected if the species is uncharged, i.e., $\sigma_k = 0$, or if the movement of the (charged) species is balanced by fast-moving ions in the diffusing medium, i.e., $\partial \phi / \partial x = 0$. For the problem we are interested in, that is, the diffusion of A in a metal (Figure A.3), we set $\sigma_A = 0$. We also assume that the film extends infinitely in the y- and z-directions, that is, the film is thin by comparison to its lateral dimensions. The resulting equation is simply Fick's first law of diffusion in one dimension, which, written for the transport of species A, is

$$J_{\mathrm{A}} = -D_{\mathrm{A}} \frac{\partial c_{\mathrm{A}}}{\partial x} \tag{A.19}$$

Application of mass conservation yields Fick's second law

$$\frac{dc_{\mathrm{A}}}{dt} = D_{\mathrm{A}} \frac{\partial^2 c_{\mathrm{A}}}{\partial x^2} \tag{A.20}$$

Under a small signal perturbation of a voltage (or current) to the system, a perturbation in the concentration of species A in the film about its steady-state value occurs; the concentration can be separated into its steady-state and time-dependent components

$$c_{\mathrm{A}} = \overline{c}_{\mathrm{A}} + \Delta c_{\mathrm{A}} e^{j\omega t} \tag{A.21}$$

where j is the imaginary number, $\sqrt{-1}$, $\overline{c}_{\mathrm{A}}$ is the steady-state concentration and Δc_{A} is a function of the angular frequency, ω, and corresponds to the perturbation amplitude of c_{A} resulting from the applied perturbation in the electric field. That is, although A is uncharged, its movement is driven by the electrochemical reaction at $x = 0$. Inserting Equation (A.21) into (A.20) and canceling steady-state terms results in Fick's second law expressed in terms of the perturbation amplitude,

$$j\omega \Delta c_{\mathrm{A}} = D_{\mathrm{A}} \frac{\partial^2 \Delta c_{\mathrm{A}}}{\partial x^2} \tag{A.22}$$

The reversible boundary conditions for (A.22) are given by

$$\Delta c_{\mathrm{A}} = 0 \ @ \ x = L \quad \text{and} \quad \Delta c_{\mathrm{A}} = \Delta c_{\mathrm{A0}} \ @ \ x = 0 \tag{A.23}$$

where Δc_{A} at $x = L$ is selected to be fixed at zero, while a finite value of Δc_{A0} is specified at the electrode ($x = 0$). For convenience, we can define dimensionless concentration and length as

$$\theta_{\mathrm{A}} = \frac{\Delta c_{\mathrm{A}}}{\Delta c_{\mathrm{A0}}} \quad \text{and} \quad \delta = \frac{x}{L} \tag{A.24}$$

respectively. Inserting these dimensionless variables into Equation (A.22) and defining the dimensionless frequency,

$$K_{\mathrm{A}} = \frac{\omega L^2}{D_{\mathrm{A}}} \tag{A.25}$$

we obtain

$$\frac{\partial^2 \theta_{\mathrm{A}}}{\partial \delta^2} - jK\theta_{\mathrm{A}} = 0 \tag{A.26}$$

The general solution to Equation (A.26) is well-known and has the form,

$$\theta_{\mathrm{A}} = Be^{\delta\sqrt{jK_{\mathrm{A}}}} - Ce^{-\delta\sqrt{jK_{\mathrm{A}}}} \tag{A.27}$$

where the constants B and C can be determined by the boundary conditions of Equation (A.23) in dimensionless form,

$$\theta_{\mathrm{A}} = 0 \quad @ \quad \delta = 1 \qquad \text{and} \qquad \theta_{\mathrm{A}} = 1 \quad @ \quad \delta = 0 \tag{A.28}$$

Applying these boundary conditions to Equation (A.27), we find that

$$B = \frac{e^{-\sqrt{jK_{\mathrm{A}}}}}{e^{-\sqrt{jK_{\mathrm{A}}}} - e^{\sqrt{jK_{\mathrm{A}}}}} \quad \text{and} \quad C = \frac{e^{\sqrt{jK_{\mathrm{A}}}}}{e^{-\sqrt{jK_{\mathrm{A}}}} - e^{\sqrt{jK_{\mathrm{A}}}}} \tag{A.29}$$

Inserting Equations (A.29) in to (A.27) and employing the relation, $2\sinh(z) \equiv e^z - e^{-z}$, Equation (A.27) becomes

$$\theta_{\mathrm{A}} = \frac{\sinh\left[\left(\delta - 1\right)\sqrt{jK_{\mathrm{A}}}\right]}{\sinh\left(-\sqrt{jK_{\mathrm{A}}}\right)} \tag{A.30}$$

which describes the concentration perturbation profile of A in the film. The dimensionless frequency K_{A}, Equation (A.25), gives the characteristic parameters of the system. Specifically, Equation (A.25) can be written as

$$K_{\mathrm{A}} = \frac{\omega}{\omega_{\mathrm{A}}^{*}} = \omega\tau_{\mathrm{A}}^{*} \quad \text{where } \tau_{\mathrm{A}}^{*} = \frac{L^2}{D_{\mathrm{A}}} \tag{A.31}$$

where ω_{A}^{*} and τ_{A}^{*} are the characteristic frequency and time, respectively, of the diffusion of A through the film.

The diffusion impedance can be obtained from the ratio of the applied perturbation voltage and the resulting current that flows at $x = 0$ (or $\delta = 0$). The current flowing at the electrode is related to the flux of the diffusing species, that is, $\Delta i_{\mathrm{A}}\big|_{\delta=0} = nFA\,\Delta J_{\mathrm{A}}\big|_{\delta=0}$, where n is the number of electrons transferred (as shown in Figure A.3), A is the interfacial area at the electrolyte | metal interface (or the cross-sectional area for diffusion). Thus, the perturbation current at $\delta = 0$ is

$$\Delta i_{\mathrm{A}}\Big|_{\delta=0} = nFA\,\Delta J_{\mathrm{A}}\Big|_{\delta=0} = -\frac{nFAD_{\mathrm{A}}\,\Delta c_{\mathrm{A}0}}{L}\frac{\partial\theta_{\mathrm{A}}}{\partial\delta}\bigg|_{\delta=0} \tag{A.32}$$

for which the relationship between ΔJ_{A} and the gradient of θ_{A} is obtained from Fick's first law, (A.19), under perturbation. The dimensionless concentration gradient at $\delta = 0$ is

$$\frac{d\theta_{\mathrm{A}}}{d\delta}\bigg|_{\delta=0} = \frac{\sqrt{jK_{\mathrm{A}}}\cosh\left[(\delta-1)\sqrt{jK_{\mathrm{A}}}\right]}{-\sinh\left(\sqrt{jK_{\mathrm{A}}}\right)}\Bigg|_{\delta=0} = \frac{-\sqrt{jK_{\mathrm{A}}}}{\tanh\left(\sqrt{jK_{\mathrm{A}}}\right)} \tag{A.33}$$

The expression of the applied voltage perturbation can be determined from recognizing that, under the assumption of rapid charge transfer kinetics, i.e., a reversible boundary condition at $x = 0$, electrochemical equilibrium is reached at the electrode.

$$\tilde{\mu}_{\mathrm{A}^{n+}}^{(lyte)}\Big|_{x=0} + n\tilde{\mu}_{e^-}^{(met)}\Big|_{x=0} = \mu_{\mathrm{A}}^{(met)}\Big|_{x=0} \tag{A.34}$$

where $\tilde{\mu}$ denotes the electrochemical potential, μ is the chemical potential, the subscript denotes the species and the superscript indicates the phase/medium in which the species resides. We assume that Equation (A.34) holds locally upon perturbation

$$\Delta\tilde{\mu}_{\mathrm{A}^{n+}}^{(lyte)}\Big|_{x=0} + n\,\Delta\tilde{\mu}_{e^-}^{(met)}\Big|_{x=0} = \Delta\mu_{\mathrm{A}}^{(met)}\Big|_{x=0} \tag{A.35}$$

We also assume that the transport of A^{n+} in the electrolyte is fast, which combined with fast charge transfer kinetics at $x = 0$, implies that $\Delta\tilde{\mu}_{\mathrm{A}^{+}}^{(lyte)} = 0$. Recognizing that the voltage perturbation, ΔV, is

$$\Delta V = \frac{1}{F}\Delta\tilde{\mu}_{e^-}^{(met)} \tag{A.36}$$

we can obtain from Equations (A.35) and (A.36) that ΔV at $x = 0$ is directly proportional to $\Delta\mu_{\mathrm{R}}^{(met)}\Big|_{x=0}$, that is,

$$\Delta V\Big|_{x=0} = \frac{1}{nF}\Delta\mu_{\mathrm{A}}^{(met)}\Big|_{x=0} \tag{A.37}$$

The perturbation of the chemical potential, $\Delta\mu_{\mathrm{A}}$, can be determined by carrying out a Taylor expansion of μ_{A} about of the steady-state value of $\overline{c}_{\mathrm{A}}$ by the quantity Δc_{A}. This yields

$$\Delta\mu_{\mathrm{A}} = RT\left(\frac{\Delta c_{\mathrm{A}}}{\overline{c}_{\mathrm{A}}}\right) \tag{A.38}$$

Inserting Equation (A.38) into (A.37), the voltage amplitude at $\delta = 0$ can be expressed as

$$\Delta V\Big|_{\delta=0} = \frac{RT}{nF}\left(\frac{\Delta c_{\mathrm{A0}}}{\overline{c}_{\mathrm{A}}}\right) \tag{A.39}$$

Therefore, the impedance response of the system shown in Figure A.3 is

$$Z(\omega) \equiv \frac{\Delta V\big|_{\delta=0} e^{j\omega t}}{\tilde{i}_{\mathrm{A}}\big|_{\delta=0} e^{j\omega t}} = \frac{RT}{(nF)^2 D_{\mathrm{A}} \bar{c}_{\mathrm{A}}} \frac{L}{A} \frac{\tanh\left(\sqrt{jK_{\mathrm{A}}}\right)}{\sqrt{jK_{\mathrm{A}}}} \tag{A.40}$$

or, collecting the constants in the beginning of the expression,

$$Z(\omega) = R_{\mathrm{A0}} \frac{\tanh\left(\sqrt{jK_{\mathrm{A}}}\right)}{\sqrt{jK_{\mathrm{A}}}} \tag{A.41}$$

where

$$R_{\mathrm{A0}} = \frac{RT}{(nF)^2 D_{\mathrm{A}} \bar{c}_{\mathrm{A}}} \frac{L}{A} \tag{A.42}$$

In the limit of zero frequency, i.e., $K_{\mathrm{A}} = 0$, the impedance, Z approaches the value R_{A0}, shown in Equation (A.42). Equation (A.42) is similar to the Nernst-Einstein equation for the transport of a charged species but is derived for the diffusion of a neutral species; n can be thought of as the “effective” charge of the neutral species A, that is, it is the charge of A once it is incorporated into the electrolyte as A^{n+}.

A.3 Reaction Mechanism

In this section, we obtain the $p\mathrm{H}_2$ and $p\mathrm{H}_2\mathrm{O}$ dependences of the hydrogen electro-oxidation for several possible rate-limiting steps. For the Pt thin film presented in Chapter 3, we propose the two-phase reaction pathway for the half-cell reaction, $\mathrm{H}_{2(g)} \underset{k_r}{\overset{k_f}{\rightleftharpoons}} 2\mathrm{H}^+_{CDP} + 2\mathrm{e}^-$ shown in Figure A.4. The reaction steps for this pathway are shown in Equations (A.43)–(A.46).

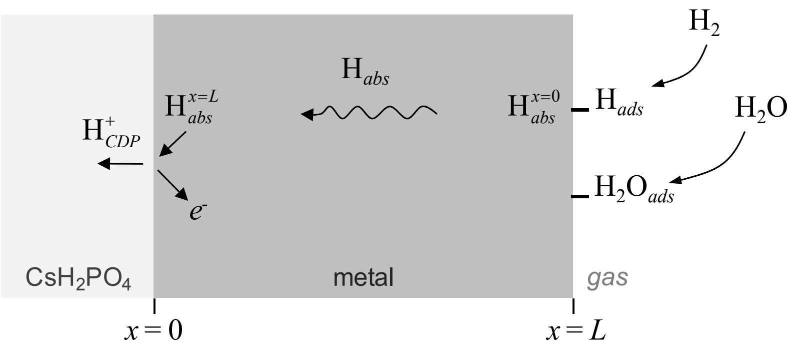

Figure A.4 Two-phase boundary pathway for hydrogen electro-oxidation.

$$\text{dissociative adsorption:}\quad H_{2(g)} + 2S \underset{k_{des}}{\overset{k_{ads}}{\rightleftharpoons}} 2H_{ads} \qquad K_{ads} = \frac{[H_{ads}]^2}{pH_2[S]^2} \tag{A.43}$$

$$\text{absorption:}\quad H_{ads} + I \underset{k_{dsb}}{\overset{k_{abs}}{\rightleftharpoons}} H_{abs}^{x=L} + S \qquad K_{abs} = \frac{\left[H_{abs}^{x=L}\right][S]}{[H_{ads}][I]} \tag{A.44}$$

$$\text{diffusion:}\quad H_{abs}^{x=L} \xleftrightarrow{diffuson} H_{abs}^{x=0} \qquad J_H = -D_H \frac{\left[H_{abs}^{x=0}\right] - \left[H_{abs}^{x=L}\right]}{L} \tag{A.45}$$

$$\text{charge transfer:}\quad H_{abs}^{x=0} \underset{k_{red}}{\overset{k_{ox}}{\rightleftharpoons}} H_{CDP}^{+} + e^{-} + I \qquad K_{CT} = \frac{\left[H_{CDP}^{+}\right] n[I]}{\left[H_{abs}^{x=0}\right]} \tag{A.46}$$

S denotes a surface site on the metal available for adsorption, I denotes an interstitial site in the metal, the subscripts *ads* and *abs* adsorbed and absorbed species. Forward and reverse reaction rate constants, k_i, and equilibrium constants, K_i, are denoted by appropriate subscripts, as indicated in (A.43), (A.44), and (A.46). The flux of hydrogen through the film is denoted as J_H and the diffusion coefficient is D_H. The positions $x = 0$ and $x = L$ are shown in Figure A.4.

Although water is not expected to play a direct role in the reaction, we suspect that water may adsorb reversibly onto surface sites of the metal. We assume that water occupies only one metal surface site,

$$\mathrm{H_2O} + \mathrm{S} \underset{k_{des'}}{\overset{k_{ads'}}{\rightleftharpoons}} \mathrm{H_2O}_{ads} \qquad K_{ads'} = \frac{[\mathrm{H_2O}_{ads}]}{p\mathrm{H_2O}[\mathrm{S}]} \tag{A.47}$$

Consequently, the site balance for the metal surface is:

$$S_T = [\mathrm{S}] + [\mathrm{H}_{ads}] + [\mathrm{H_2O}_{ads}] \tag{A.48}$$

where S_T denotes the total number a surface sites available on the metal. The number of absorption sites in the metal must also be considered, but in the case of platinum (and even palladium) the fraction of the interstitial sites occupied by hydrogen is small,

$$I_T = [\mathrm{I}] + [\mathrm{H}_{abs}] \approx [\mathrm{I}] \tag{A.49}$$

where I_T is the total number of interstitial sites.

We employ the above expressions to determine the $p\mathrm{H_2}$ and $p\mathrm{H_2O}$ reaction orders for hydrogen electro-oxidation for four possible scenarios, each with a different rate-limiting step. Because we measure the impedance response at equilibrium, both the forward and reverse directions of the rate-limiting steps are probed, that is,

$$r_{RLS} = r_{RLS-f} = r_{RLS-r} \tag{A.50}$$

where r_i denotes the rate step i, RLS denotes rate-limiting step, and f and r denote forward and reverse, respectively.

A.3.1 Hydrogen Adsorption as a Rate-Limiting Step

Following Equation (A.50), the rate of the slowest step, hydrogen adsorption, can be expressed as:

$$r_{ads} = k_{ads}pH_2\left[\mathrm{S}\right]^2 = k_{des}\left[\mathrm{H}_{ads}\right]^2 \tag{A.51}$$

Because absorption, diffusion and charge transfer steps are fast relative to adsorption, they reach equilibrium and the concentrations the involved species are expressed by the equilibrium constants in (A.44) and (A.46). In the case of fast hydrogen diffusion, the concentration gradient of absorbed hydrogen in the metal film is negligible, that is,

$$\left[\mathrm{H}_{abs}^{x=0}\right] = \left[\mathrm{H}_{abs}^{x=L}\right] \tag{A.52}$$

Further employing the site balance shown in Equation (A.48) and the equilibrium relation for water adsorption in Equation (A.47), we find that

$$\left[\mathrm{S}\right] = \frac{S_T}{\left(1 + \frac{\left[\mathrm{H}_{\mathrm{CDP}}^{+}\right]n}{K_{CT}K_{abs}} + K_{ads'}pH_2O\right)} \tag{A.53}$$

and, therefore, from the first equality in Equation (A.51), the rate of adsorption is

$$r_{ads} = \frac{{S_T}^2 k_{ads}pH_2}{\left(1 + \frac{\left[\mathrm{H}_{\mathrm{CDP}}^{+}\right]n}{K_{CT}K_{abs}} + K_{ads}pH_2O\right)^2} \tag{A.54}$$

Because the concentrations of protons in the CsH_2PO_4, $\left[\mathrm{H}_{\mathrm{CDP}}^{+}\right]$, and electrons in a metal, *n*, are constant, Equation (A.54) implies that the total reaction rate scales with pH_2 with a reaction order of 1 when pH_2O is held constant.

A.3.2 Hydrogen Absorption as a Rate-Limiting Step

For process limited by the absorption/desorption of hydrogen in the metal film,

$$r_{abs} = k_{abs}\left[\mathrm{H}_{ads}\right]\left[\mathrm{I}\right] = k_{dsb}\left[\mathrm{H}_{abs}^{x=L}\right]\left[\mathrm{S}\right] \tag{A.55}$$

Employing a similar procedure as in the previous section, that is, assuming all other steps reach equilibrium and using the site balances in (A.48) and (A.49), we obtain

$$\left[\mathrm{H}_{ads}\right]=\frac{K_{ads}{}^{1/2}p\mathrm{H}_2{}^{1/2}S_T}{1+K_{ads'}p\mathrm{H}_2\mathrm{O}+K_{ads}{}^{1/2}p\mathrm{H}_2{}^{1/2}} \tag{A.56}$$

and from the first equality in (A.55),

$$r_{abs}=k_{abs}\frac{S_T I_T}{1+\left(\dfrac{1+K_{ads'}p\mathrm{H}_2\mathrm{O}}{K_{ads}{}^{1/2}p\mathrm{H}_2{}^{1/2}}\right)} \tag{A.57}$$

Unlike the case of adsorption as a rate-limiting step, both the $p\mathrm{H}_2$ and $p\mathrm{H}_2\mathrm{O}$ reaction orders cannot be explicitly extracted from a log-log plot of the rate as a function of partial pressure.

It should be noted that if water occupies none or a small fraction of the metal surface sites such that $S_T=\left[S\right]+\left[H_{ads}\right]$, one can obtain a much simpler expression for the rate of the reaction,

$$r_{abs}=S_T I_T k_{abs}K_{ads}{}^{1/2}p\mathrm{H}_2{}^{1/2} \tag{A.58}$$

A.3.3 Hydrogen Diffusion as a Rate-Limiting Step

For the diffusion of hydrogen as the slowest step, we obtained

$$J=-D_H\frac{\left[\mathrm{H}_{abs}^{x=0}\right]-\left[\mathrm{H}_{abs}^{x=L}\right]}{L}=-\frac{D_H I_T}{L}\left(\frac{\left[\mathrm{H}_{\mathrm{CDP}}^{+}\right]n}{K_{CT}}-K_{abs}K_{ads}{}^{1/2}p\mathrm{H}_2{}^{1/2}\right) \tag{A.59}$$

Therefore, the reaction rate when limited by diffusion is not directly proportional to $p\mathrm{H}_2{}^{1/2}$. This is a consequence of the concentration of absorbed hydrogen in the metal at the metal | $\mathrm{CsH_2PO_4}$ interface being fixed by the proton concentration of $\mathrm{CsH_2PO_4}$. (This is in contrast to the rate of hydrogen diffusion in permeation membranes which exhibits a direct proportionality to $pH_2^{1/2}$ due to both sides of the metal being exposed to hydrogen gas.)

A.3.4 Charge Transfer as a Rate-Limiting Step

Following Equation (A.50), the rate of charge transfer near equilibrium is

$$r_{CT} = k_{ox}\left[\mathrm{H}_{abs}^{x=0}\right] = k_{red}\left[\mathrm{H}_{\mathrm{CDP}}^{+}\right]n\left[\mathrm{I}\right] \tag{A.60}$$

Using the appropriate equilibrium relations and site balances, we obtain the concentration of hydrogen in the metal at the metal | CsH_2PO_4 interface to be

$$\left[\mathrm{H}_{abs}^{x=0}\right] = K_{abs}K_{ads}{}^{1/2}I_T\, p\mathrm{H}_2{}^{1/2} \tag{A.61}$$

The rate of a process limited by charge transfer is then proportional to $pH_2^{1/2}$,

$$r_{CT} = k_{ox}K_{abs}K_{ads}{}^{1/2}I_T\, p\mathrm{H}_2{}^{1/2} \tag{A.62}$$

Appendix B Reactivity of Candidate Electrocatalysts with CsH_2PO_4

B.1 Motivation

For low-temperature fuel cells, many metals exist as their oxides at open-circuit conditions and/or under operating voltages. Figure B.1 shows a list of metal oxides and the Gibbs free energy for their formation from their metals in air at 240 ºC.[87] The corresponding equilibrium potentials, with respect to an air reference, are also shown. (To determine the corresponding potential for the cathode of a fuel cell, add the open-circuit voltage of ~ 1.1 V to the *y*-axis.) All metals above the zero line will be stable in air at open-circuit conditions of a fuel cell, whereas all metals below the zero line will be oxidized at open-circuit conditions. However, an applied voltage can change the state of the material (as demonstrated by the electrochemical reduction of Pt oxide in Chapter 3) and keep the metal as the thermodynamically preferred phase. For example, during fuel cell operation, typically at a cell voltage of ~ 0.7 V (or ~ –0.4 V in Figure B.1), metals that will be stable as oxides are all those residing above the –0.4 V line. Thus, thermodynamics predicts that PtO_2, PtO, PdO, IrO_2 and Ir_2O_3 (Figure B.1 inset), while stable in a fuel cell at the open-circuit voltage, will be reduced when current is drawn and the cell operated at 0.7 V.

The state of the electrocatalyst under fuel cell operating potentials is important because it dictates how to construct experiments to screen for or study catalysts. For example, in order to conduct fundamental studies of oxygen electro-reduction over Pt metal, a bias must be applied to the cell, and thus symmetric cell studies are not possible.

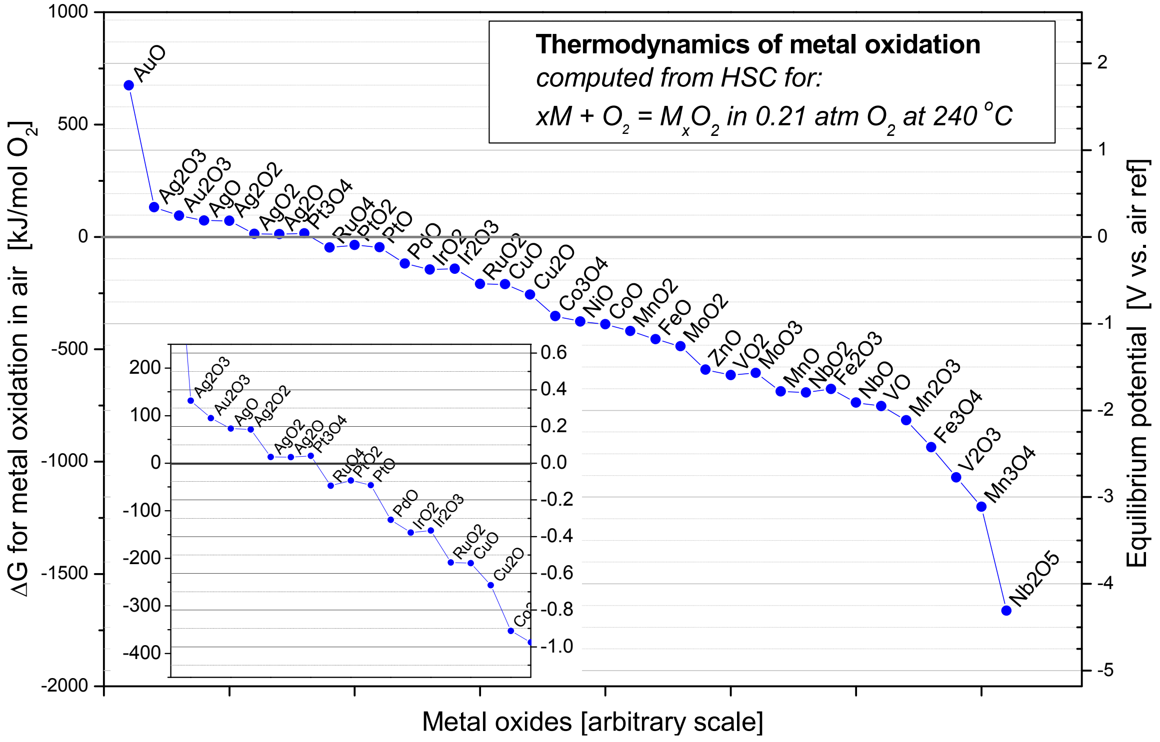

Figure B.1 Plot of Gibbs free energy for metal oxide formation at 240 ºC in 0.21 atm O_2 for various metal oxides.

Both metals and metal oxides can be active electrocatalysts for reducing oxygen. However, some oxides have been observed in the laboratory to react with CsH_2PO_4 and thus would not be viable as electrocatalysts in SAFC electrodes. In this section, we summarize results of a study that evaluates the reactivity between potential electrocatalysts and CsH_2PO_4. We also extend the investigation to metal carbides and nitrides.

B.2 Experimental

B.2.1 Sample Preparation and Heat Treatment

Course CsH_2PO_4 powders were mixed with metal or metal oxide powders (various sources and particle sizes) and a mortar and pestle, placed in a quartz (or Pyrex) cup and heated to various temperatures under humidified air flow (~ 0.4 atm H_2O). In some cases, the mixtures were characterized after heat treatment at 150 ºC for 48 h before heat treatment at 240 ºC to evaluate the effect of the superprotonic transition and kinetics on the reactivity of CsH_2PO_4 with the metal/oxide powders. Samples that did not exhibit reaction at 150 ºC were further heated at 240 ºC for times ranging between 5 and 41 h.

Metal nitrides and carbides were first tested for their resistance to oxidation by heating the powders in quartz (or Pyrex) cups at 240 ºC for 24–82 h under flowing air with ~ 0.4 atm H_2O. Those that did not exhibit signs of oxidation were mixed with CsH_2PO_4 and heated at similar conditions for 24 h.

B.2.2 Characterization

All powders and their mixtures, before and after heat treatment, were characterized by X-ray diffraction using a Phillips X'Pert Pro powder diffractometer with Cu Kα radiation (45 kV, 40 mA) with a 2θ range of 5º to 90º.

B.3 Results and Discussion

Table B.1 tabulates all the oxide materials (with the exception of a tungstic acid which is not an oxide) tested under various conditions, as specified. In the case of the oxides, most products generated from the reaction were unidentified. Reaction products which were identified are noted in the table. Bolded starting material names indicate compounds that did not appear to react with CsH_2PO_4. Note that for Fe_3O_4, all the CsH_2PO_4 peaks disappeared but there were no product peaks.

Table B.2 tabulates the oxidation stability of some nitrides and carbides and their reactivity with CsH_2PO_4. Several of the carbides are readily oxidized in air, whereas almost all the nitrides tested were stable in air. Of the carbides, only TaC and ZrC appeared to be stable with CsH_2PO_4. Of the nitrides, all exhibited no reaction with CsH_2PO_4, with the exception of iron nitride.

It is important to note that the computed thermodynamic driving force for metal carbide oxidation, specifically for NbC, TaC and ZrC (no thermodynamic data was available for B_4C), indicates that these carbides are not stable in air (Figure B.2a). Their apparent resistance to oxidation is likely a consequence of a blocking oxide layer that kinetically limits further oxidation. This also would imply that it is this oxide surface that is relevant for electrocatalysis (and reactivity). However, the observed reactivity of NbC, which is expected to have a layer of oxide on top, after 24 h is surprising since no reaction of Nb_2O_5 with CsH_2PO_4 was observed after 36 h. The oxides of Ta and Zr were not available for testing, so it is unclear what the stability of TaC and ZrC with CsH_2PO_4 implies.

Metal nitrides are generally more stable in air than metal carbides, primarily because of the high partial pressures of nitrogen in air (0.27 atm N_2 compared to < 0.0005 atm). Thermodynamics predicts Fe_2N and Fe_4N are stable in air and, thus, it is unclear why oxidation of Fe_xN was observed.

Table B.1 Reactivity of CsH_2PO_4 (CDP) with metal oxides at various temperatures for as-specified times under flowing air with ~ 0.4 atm H_2O. Bolded means no reaction with CDP.

Starting material		**150 ^{o}C, 48 h**	**240 ^{o}C, + 5 h**		**240 ^{o}C, + 36 h** (unless otherwise noted)	
		Rxn?	*Rxn?*	*Product(s)*	*Rxn?*	*Product(s)*
aluminum oxide	Al_2O_3	N	N		Y	
silver(I) oxide	Ag_2O	Y	Y	$AgPO_3$	—	
copper(II) oxide	CuO	N	Y	unidentified	—	
zinc oxide	ZnO	Y	Y	$CsZnPO_4$ + unidentified	—	
nickel(II) oxide	**NiO**	**N**	**N**		**N**	
palladium	Pd	N	Y	unidentified	—	
ruthenium(IV) oxide	$\mathbf{RuO_2}$	**N**	**N**		**N**	
cobalt(II,III) oxide	Co_3O_4	N	N		Y	unidentified
cobalt (II) oxide	CoO	N	Y	unidentified	—	
iron (III) oxide	$\mathbf{Fe_2O_3}$	**N**	**N**		**N**	
iron(II,III) oxide	$\mathbf{Fe_3O_4}$	**N**	**N?**	**CDP peaks missing**	**N?**	**CDP peaks missing**
molybdenum(VI) oxide	MoO_3	N	Y	unidentified	—	
molybdenum(IV) oxide	MoO_2	N	Y	one new peak unidentified	Y	unidentified
niobium(V) oxide	$\mathbf{Nb_2O_5}$	**N**	**N**		**N**	
manganese(III) oxide	Mn_2O_3	N	Y	unidentified	—	
manganese(II) oxide	**MnO**	**N**	**N**		**N (41 h)**	
chromium(III) oxide	Cr_2O_3	N	—		—	
vanadium(V) oxide	V_2O_5	Y.	Y	$CsHVPO_6$ + unidentified	—	
titanium(IV) oxide	$\mathbf{TiO_2}$	**—**	**—**		**N (41 h)**	
tin(IV) oxide	$\mathbf{SnO_2}$	**—**	**—**		**N (41 h)**	
tungsten oxide	$WO_{2.9}$	—	—		Y (41 h)	
tungstic acid	H_2WO_4	—	—		Y (41 h)	
barium zirconate	$BaZrO_3$	N	Y	one new peak unidentified	—	

Table B.2 Reactivity of CsH_2PO_4 (CDP) with metal nitrides and carbides at 240 ºC for as-specified times under flowing air with ~ 0.4 atm H_2O. Bolded means no reaction with CDP.

Starting material		**240 °C, 24 h** (unless otherwise noted)		**240 °C, 24 h**
		Oxidized?	*Product(s)*	*Rxn w/ CDP?*
boron carbide	B_4C	N		Y
tungsten carbide	WC	Y (34 h)	WO_3	—
tungsten carbide	W_2C	Y (34 h)	WO_3	—
molybdenum carbide	Mo_2C	Y	MoO_3	—
niobium carbide	NbC	N		Y
tantalum carbide	**TaC**	**N**		**N**
vanadium carbide	VC	Y (82 h)	V_2O_5	—
titanium carbide	TiC	Y	TiO_2 anatase	—
zirconium carbide	**ZrC**	**N**		**N**
iron nitride	Fe_xN	N		Y
niobium nitride	**NbN**	**N**		**N**
tantalum nitride	**TaN**	**N**		**N**
titanium nitride	**TiN**	**N**		**N**
zirconium nitride	**ZrN**	**N**		**N**

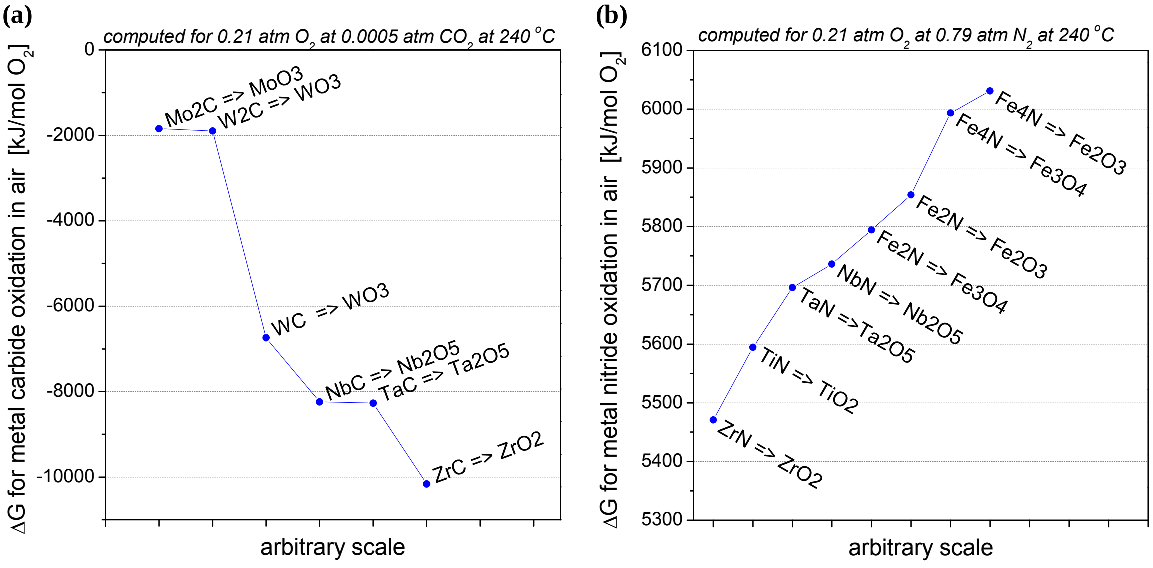

Figure B.2 Stability of select metal carbides and nitrides air at 240 ºC. The Gibbs free energy of oxidation of metal (a) carbides and (b) nitrides. Metal carbides are thermodynamically unstable while metal nitrides are stable.

Appendix C Platinum Thin Film Anodes

C.1 Experimental Setup

Figure C.1 is a schematic of the experimental setup used for symmetric cell studies. The flow rates of gases (H_2 and Ar, in this case) are controlled by digital mass flow controllers (Advanced Energy, 7800 series). Inlet gases were fed into a water bubbler, heated by a gravity convection oven. The resulting humidified flow is delivered to the reactor chamber via stainless steel pipes heated by rope heaters to prevent condensation. At the outlet, water vapor is condensed in a trap (not shown) before the gas stream is vented. The water partial pressure of the gas stream is recorded at the inlet of the reactor. The flow rates of the gases were calibrated using a bubble flow meter.

Three symmetric cell holders are available for multiplexed measurements. A schematic of the holder is shown in the inset of Figure C.1. Cells are placed between two silver ring contacts which in turn are connected to electrical leads (two on each ring for for four-probe configuration). A thermocouple is located ~ 3 mm from the cell to monitor the temperature.

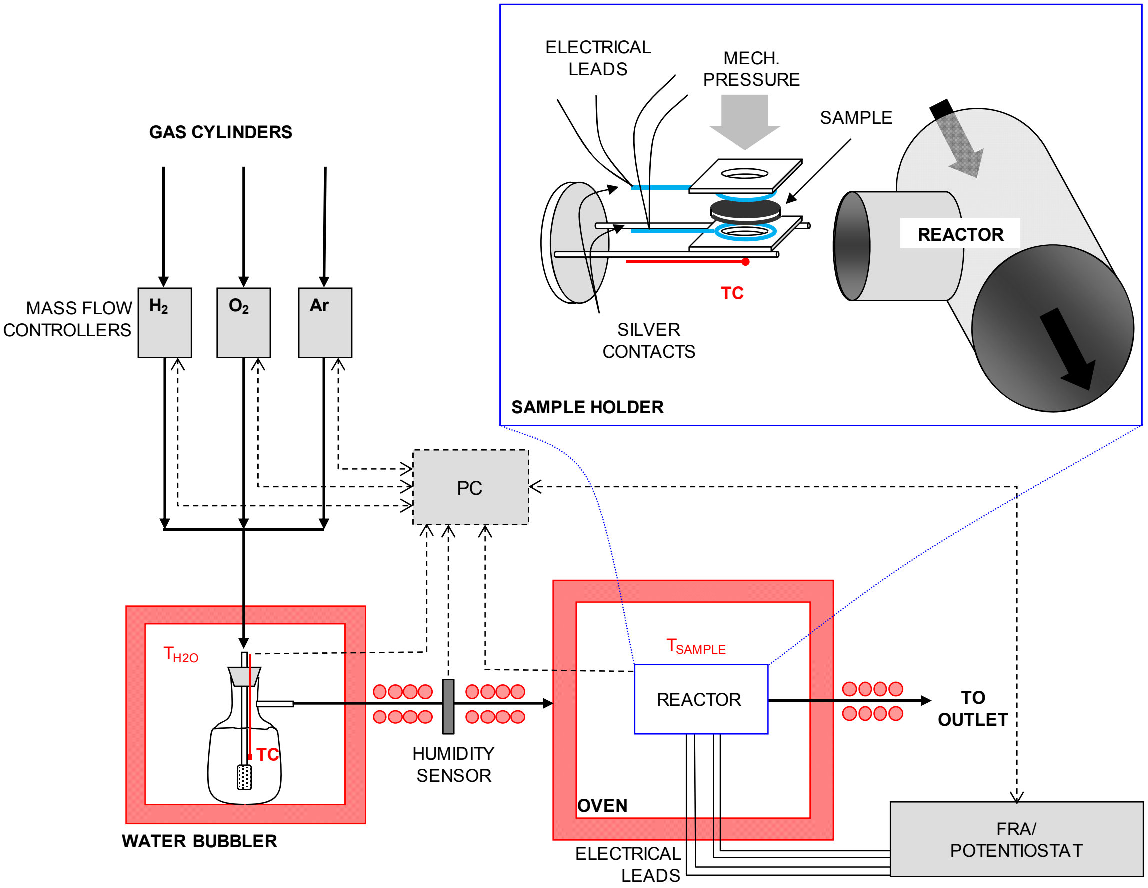

Figure C.1 Drawing of test station for symmetric cell measurements.

C.2 Platinum Film Quality

C.2.1 Before and After Electrochemical Characterization

After electrochemical testing at 250 ºC in H_2-H_2O-Ar environments, Pt films with thicknesses ≥ 7.5 nm remain intact for the most part, as shown in before-after images of 375, 75, and 7.5 nm thick films (Figure C.2, Figure C.3, Figure C.4, respectively). Also shown are images of 7.5, 22.5, 37.5, and 52.5 nm thick films after testing (Figure C.5). Of these four films, 7.5 and 22.5 nm thick films exhibit wave-like features, Figure

C.4(c–d) and Figure C.5(a–b), possibly because the films accommodate microstructural changes in CsH_2PO_4 substrate without breaking.

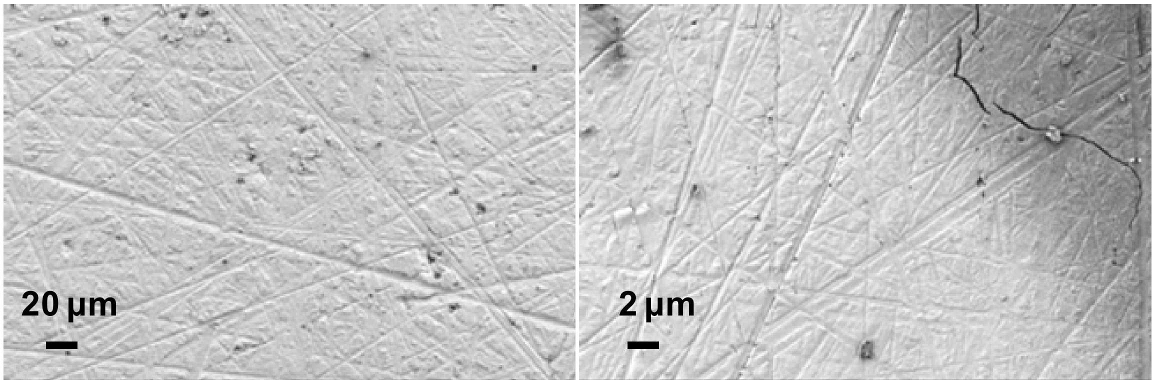

(a) *as-deposited*

(b) *as-deposited*

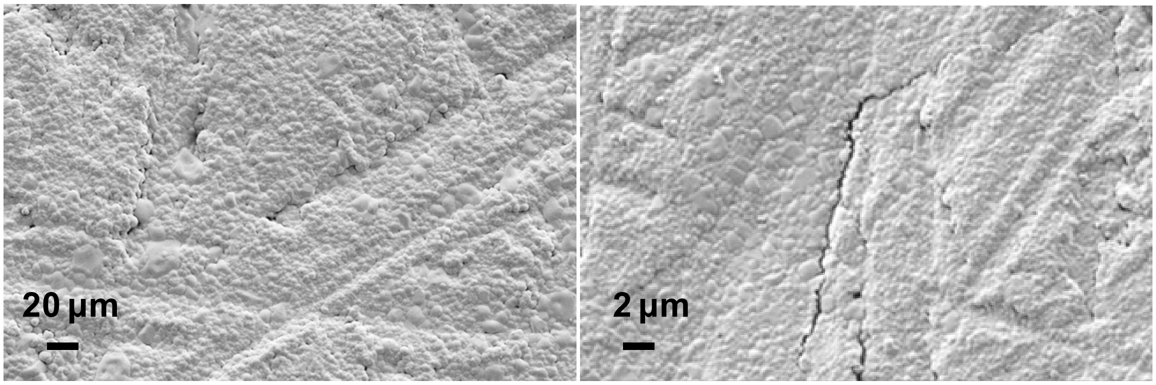

(c) *after electrochem. char.*

(d) *after electrochem. char.*

Figure C.2 Representative SEM micrographs of 375 nm Pt films on top of CsH_2PO_4 before (a–b) and after (c–d) electrochemical characterization at 250 ºC in H_2-H_2O-Ar atmospheres. The Pt-CsH_2PO_4 boundary is visible in (b) in which the darker region is the exposed CsH_2PO_4.

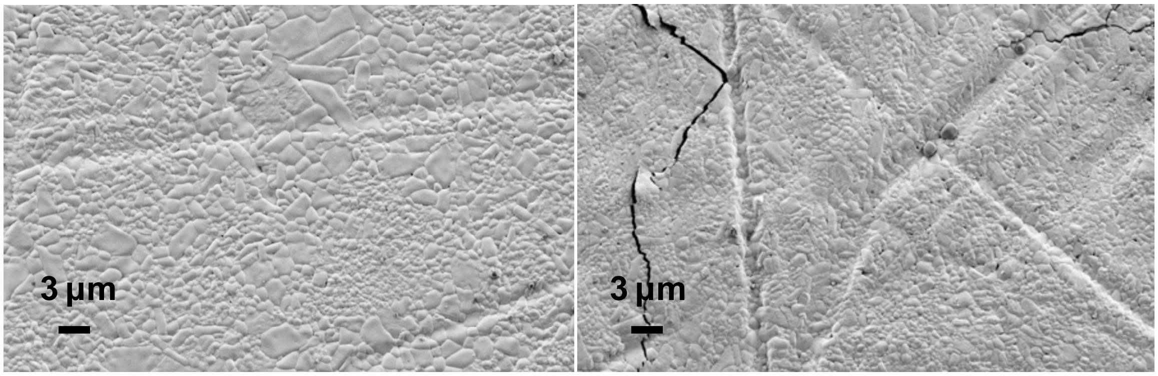
(a) *as-deposited*
(b) *after electrochem. char.*

Figure C.3 Representative SEM micrographs of 75 nm Pt films on top of CsH_2PO_4, before (a) and after (b) electrochemical characterization at 250 ºC in H_2-H_2O-Ar atmospheres. Films with either 10 nm Au on top of or below the Pt film display similar film characteristics.

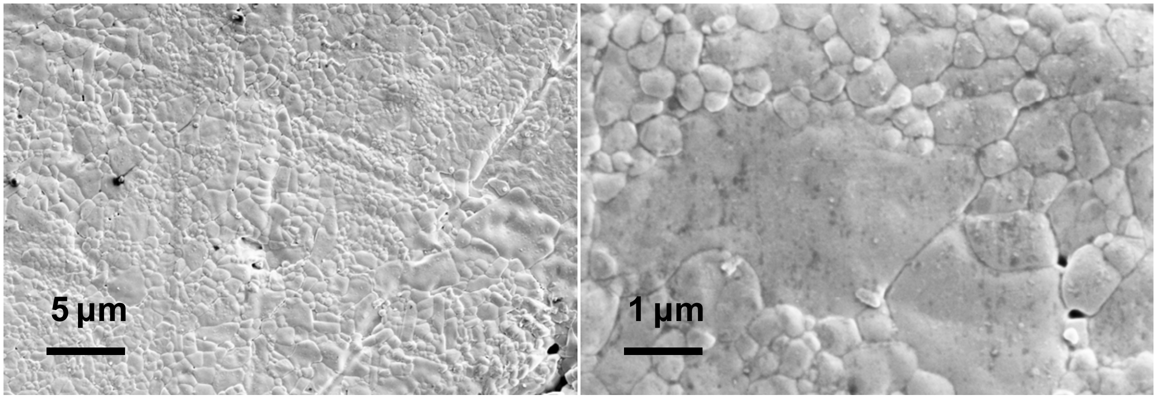
(a) *as-deposited*
(b) *as-deposited*

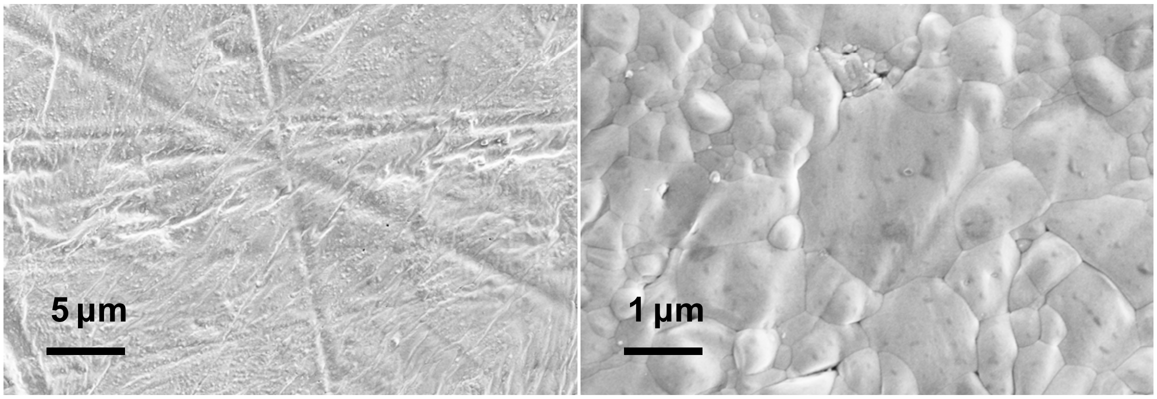
(c) *after electrochem. char.*
(d) *after electrochem. char.*

Figure C.4 Representative SEM micrographs of 7.5 nm Pt films on top of CsH_2PO_4, before (a–b) and after (c–d) electrochemical characterization at 250 ºC in H_2-H_2O-Ar atmospheres.

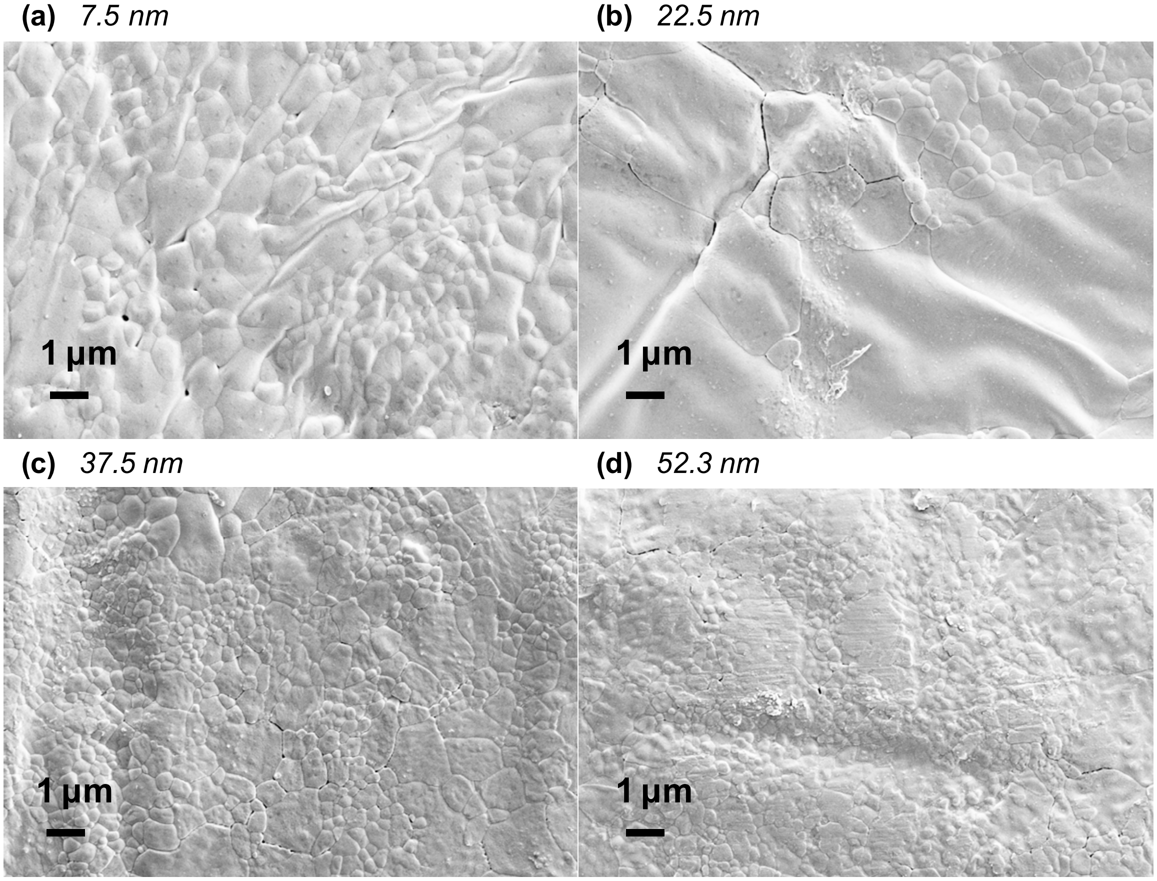

Figure C.5 Representative SEM micrographs of (a) 7.5 nm, (b) 22.5 nm, (c) 37.5 nm and (d) 52.5 nm Pt films on top of CsH_2PO_4 after electrochemical characterization at 250 ºC in H_2-H_2O-Ar atmospheres.

C.2.2 Film Structure and Impedance Response of Sub-5 nm Films

The observation of the electrode response for 7.5 nm films being co-limited by multiple processes, that is, diffusion of hydrogen and one (or more) interfacial processes suggests that furthering reducing the film thickness should given additional reduction in the electrode resistance. Unfortunately, Pt films before and after testing clearly revealed that intact, conformal, as-deposited Pt films degrade after electrochemical testing at superprotonic conditions. SEM micrographs for as-deposited 1.5, 3, and 4.5 nm films appear to be fully intact as indicated by the undersides of the films, Figure C.6(a–c). In these images, cracks in the film are due to the fragility of the films when removing them from their substrates, and white spherical particles, particularly visible in Figure C.6(a,c) are precipitated CsH_2PO_4 particles formed as a result of substrate dissolution processes. The films examined after electrochemical characterization, Figure C.6(d–f), show different characteristics depending on the film thickness. 4.5 nm films (Figure C.6d) appeared relatively intact after electrochemical characterization, with a few microcracks occurring near the grain boundaries of CsH_2PO_4 (inset) and features that appear to be folds and creases in the film, whereas 1.5 nm films (Figure C.6f) aggregated into small islands of different sizes, from 500 nm to below 50 nm (inset). Although temperatures around 250 ºC are not high enough to induce the sintering of Pt metal, the mobile and ductile solid acid substrate,[17, 19, 28] combined with the extremely thin Pt layers deposited, may enable the migration of Pt species on the substrate surface. The film characteristics of the sub-5 nm films are in agreement with the sheet resistance of the films before and after electrochemical characterization, that is, the sheet resistance of the 1.5 and 3 nm films increase by almost three-fold after testing. As expected, based on Figure C.6d, the sheet resistance of the 4.5 nm films after testing increased only slightly, comparable to that observed for 7.5 nm films.

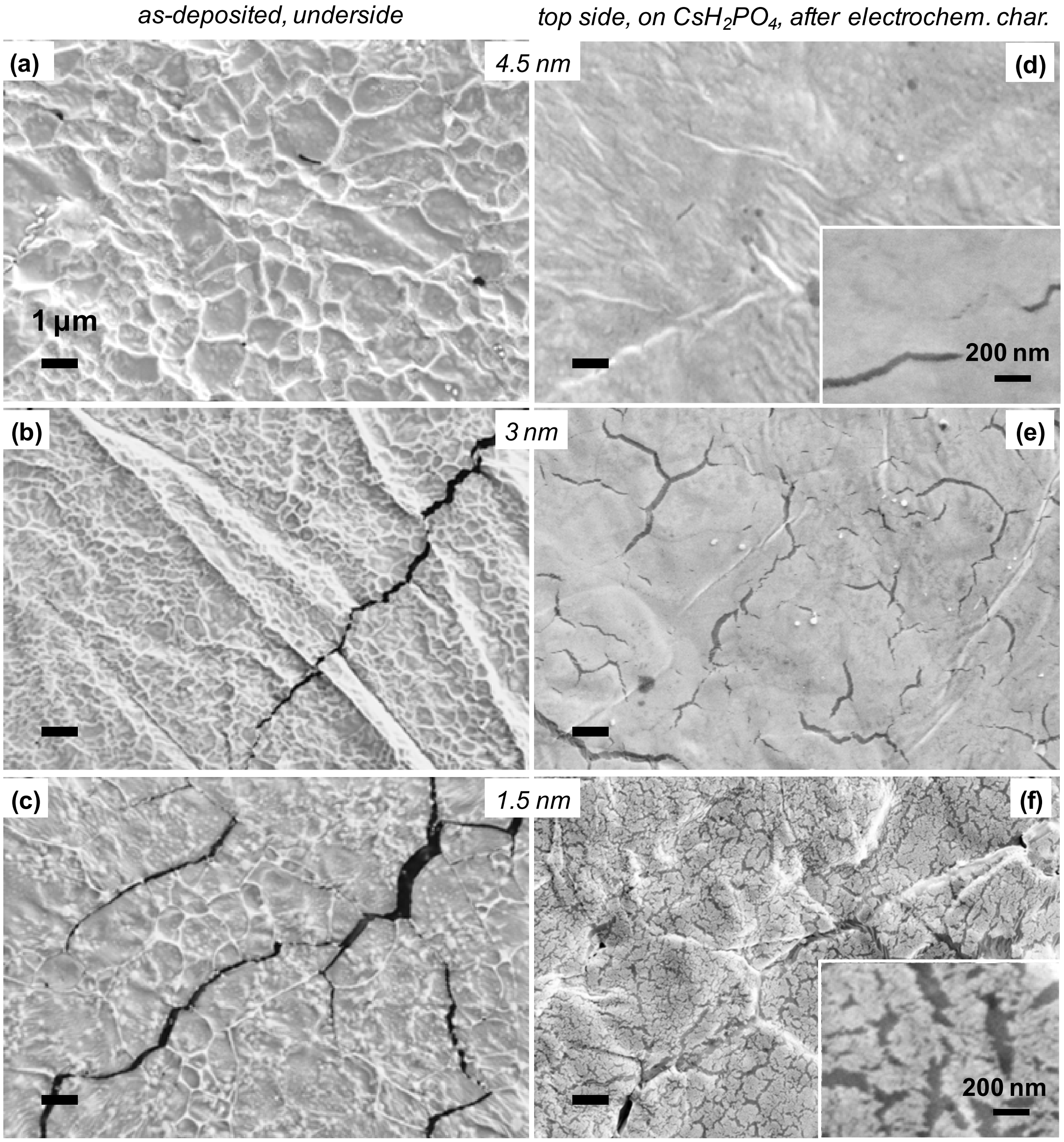

Figure C.6 SEM micrographs of sub-5 nm thin Pt films: (a–c) Undersides of Pt films, isolated from their CsH_2PO_4 substrates, before electrochemical characterization, showing that the films conformed to the features of the CsH_2PO_4 substrate. Large cracks in the films are a consequence of the removal process. (d–f) Pt on CsH_2PO_4, after testing. Light gray = Pt, dark gray = exposed CsH_2PO_4 substrate

Pt films below 5 nm in thickness yield impedance spectra similar in shape to that for 7.5 nm films, that is, an arc is that more symmetric (Figure C.7a). However, the electrode resistance increases with decreasing film thickness, from ~ 4 Ω cm^2 for a Pt film thickness of 4.5 nm to almost 10 Ω cm^2 for a thickness of 1.5 nm. This is counter to the expectation that as the Pt film thickness is decreased, the diffusion step becomes negligible compared to interfacial processes, and the total electrode resistance should approach an interfacial resistance value of 2.2 Ω cm^2 (Figure 3.12). As shown in Figure C.7b, the resistances of 1.5, 3, and 4.5 nm Pt films are larger than predicted (solid curve). For 1.5 and 3 nm thick films, this observation is consistent with SEM observations of the degrading film quality (Figure C.6) and suggests that degradation of the film into small islands reduces the utilization of Pt. The degradation in activity for the 4.5 nm film electrode was surprising given its apparent structural stability (Figure C.6d).

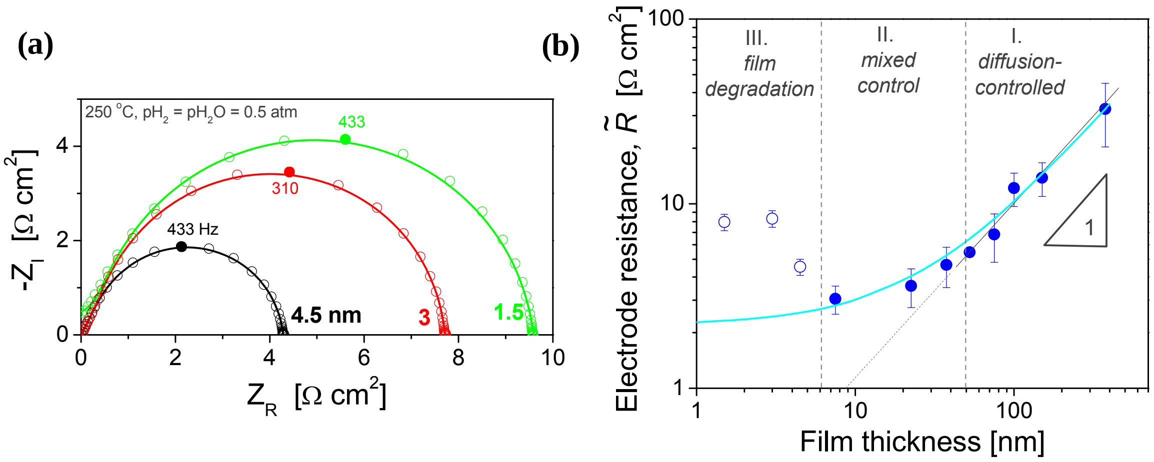

Figure C.7 (a) Nyquist spectra for 1.5, 3, and 4.5 nm thick Pt film electrodes in Pt | CsH_2PO_4 | Pt symmetric cells, showing semi-circular arcs which increased in width with decreasing film thickness. Lines show fits parallel RQ sub-circuits. Non-electrode responses have been subtracted. (b) Double-logarithmic plot of area-normalized electrode resistance as a function of Pt film thickness. Filled data markers are for films which remained intact during electrochemical testing. Open data markers are for 1.5, 3, and 4.5 nm Pt films.

Despite the differences in the resistance values for 1.5–4.5 nm films, the characteristic frequencies displayed no observable trend with thickness and, across six samples (two for each thickness), the average characteristic frequency was found to be $\omega_0 = 2.6 \pm 0.7$ kHz. The temperature and $p\mathrm{H}_2$ dependences also displayed no trend with thickness; the $p\mathrm{H}_2$ reaction order ranged between 0.68 and 0.79 and activation energies were ~ 33 kJ mol^{-1}, values which are comparable to those observed for 7.5 nm films (~ 0.75 and 28 kJ mol^{-1} from Figure 3.8). That the characteristic frequency, $p\mathrm{H}_2$ reaction order and activation energy are virtually unchanged between films with thicknesses of 1.5–7.5 nm suggests that, despite larger electrode resistances and notably different microstructures for sub-5 nm films, the rate-limiting step is the same as that for the 7.5 nm film. In other words, the larger electrode resistance is purely a consequence of the decrease in interfacial Pt | CsH_2PO_4 area due to film degradation; the small islands (under 500 nm in size) are too small to be accessible by the 100-µm scale features of carbon current collector, resulting in poor utilization of the deposited Pt.

It is interesting to note that the stabilization time for 1.5–4 nm thick Pt films at superprotonic conditions were notably longer than that for thicker films, taking over two days instead of approximately one day to reach a steady-state conditions satisfying the criterion of $\leq 2\%\ \mathrm{h}^{-1}$ change in the electrode resistance. The longer stabilization times indicate that Pt in the thinnest films was able to migrate freely whereas thick films appeared not to be affected by the substrate and were significantly more stable.

C.2.3 Mechanical Integrity: 375 nm vs. Sub-8 nm Films

Additional images of the undersides of 4.5 and 7.5 nm films (Figure C.8) appear to confirm the accommodating nature of the Pt; thin Pt films conformed to the underlying carbon tape substrate which was attached to the top side of the film before dissolution of CsH_2PO_4. The underlying features of the carbon tape are visible as mounds (10–50 µm) in the image, and furthermore, the film exhibited wrinkles as it conformed the features of the carbon tape. Films that were very thin, such as those 1.5 and 3 nm thick (Figure C.9), were more fragile and display many more tears from handling, when compared to 4.5 and 7.5 nm films. This fragility may be correlated with their tendency to aggregate into islands after testing (Figure C.6), that is, the poor interconnectivity of the Pt grains and minimal pinning of grains to neighbors allow its free migration over the CsH_2PO_4 surface at superprotonic conditions.

On the other hand, thicker films tended to be stronger, as indicated by Figure C.10, but sometimes buckled when the underlying CsH_2PO_4 moved. Buckling was observed for 375 nm films (Figure C.11), and the spatial distribution of buckling is consistent with cracking of the CsH_2PO_4 substrate, that is, when there is a crack in CsH_2PO_4, the two sides of CsH_2PO_4 can move in such a way as to cause the films to delaminate and compress. The film typically broke at weaker points of the film, primarily along polishing lines. Because buckling occured on the 100-μm scale and with relative low density, they did not affect the shape of the impedance arc, i.e., the half-teardrop shape characteristic of diffusion (Figure 3.6a). That the Warburg behavior remained suggests that the rate-limiting step was still hydrogen diffusion though the Pt film, although the total resistance of the process likely increased a small amount due to the lower Pt | CsH_2PO_4 interfacial area. Furthermore, buckling effects may also explain the frequency dispersion observed in the Warburg impedance response, that is, a deviation of n from 0.5 in the distributed finite-length Warburg expression (Equation 3.1).

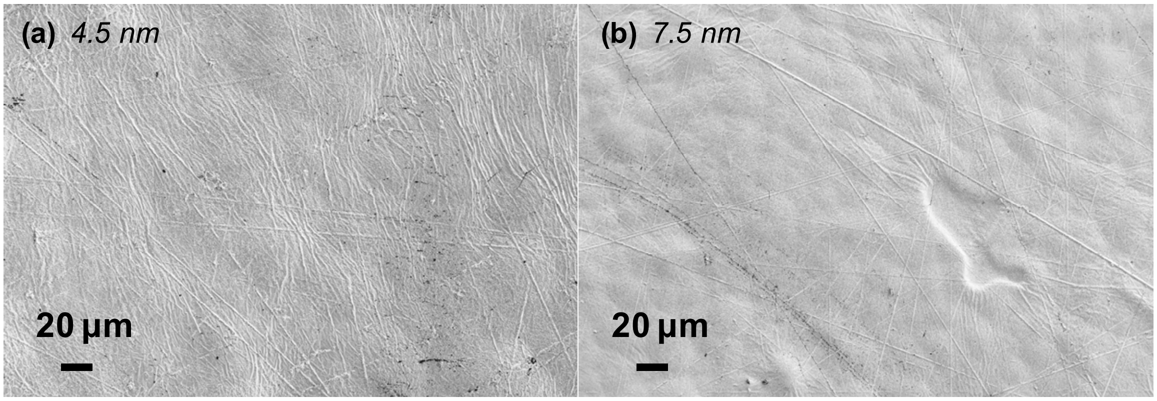

Figure C.8 SEM micrographs of the undersides of (a) 4.5 and (b) 7.5 nm films, as deposited, isolated from the CsH_2PO_4 substrate. Films conformed to the underlying carbon tape.

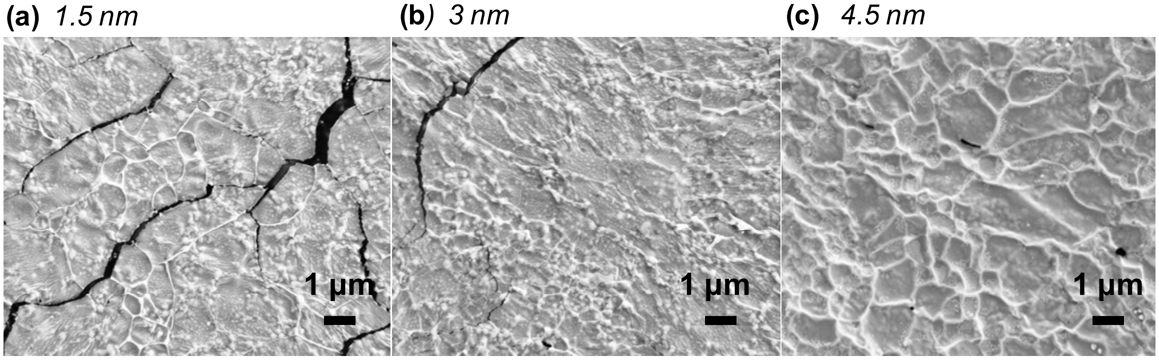

Figure C.9 Representative SEM micrographs of the undersides of 1.5, 3, and 4.5 nm films, as-deposited and isolated from their CsH_2PO_4 substrates. Cracks in the films resulted from handling. Small sub-micron light-gray features are imprints from the underlying carbon tape substrate, visible through the very thin films. For the 4.5 nm film (c), sub-100 nm precipitates of CsH_2PO_4 were also visible.

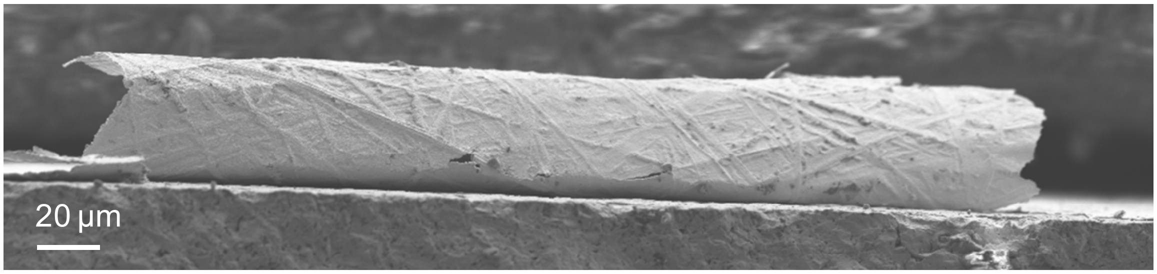

Figure C.10 A cross-section image of the Pt | CsH_2PO_4 interface where a portion of a 375 nm Pt film had delaminated.

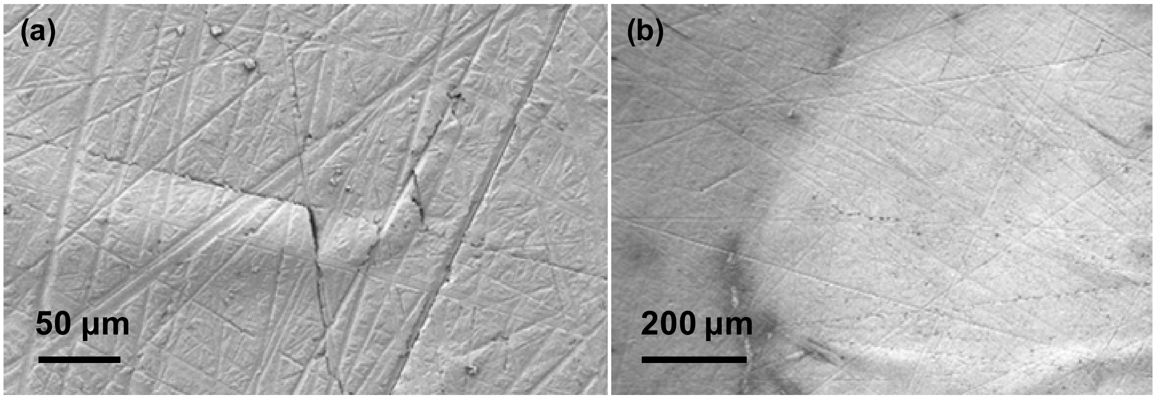

Figure C.11 SEM micrographs of a 375 nm Pt film deposited onto CsH_2PO_4, after electrochemical testing. Buckling occurred on the 100-µm scale, ending at polishing lines (left). The distribution of features suggests they are correlated to cracks in the CsH_2PO_4 substrate (right).

C.2.4 Effect of Mechanical Pressure from Current Collector

It should be noted that the quality of the films, on the micron-scale, depended on the mechanical pressure applied to the symmetric cells using the sample holder shown in Figure C.1. A pressure that is too low caused a metal-metal contact that fluctuated with external vibrations (e.g., that form the mechanical convection oven used to heat the reactor). For films which had sufficient sheet conductivity (i.e., films 7.5 nm and thicker), this only caused the ohmic offset in the impedance spectra to jump intermittently and did not affect the electrode response. However, applying too much pressure caused damage to the cell since superprotonic CsH_2PO_4 deforms under pressure. From Figure C.12, comparing (a) and (c) for 7.5 nm films, it is apparent that the effect of applied mechanical pressure is significant. The carbon fiber paper current collector left a significant number of fiber imprints in the cell (a), but when the pressure was reduced, the film was much less damaged (b). The extent of damage depended not only on the pressure applied but also on the Pt film thickness. Comparison of (a) and (b) for 7.5 nm films to (c) and (d) for

75 and 150 nm films, respectively, in Figure C.12 reveals that a greater amount of damage was incurred for thinner films than thicker films. There was not a significant impact of the applied pressure on the electrode response of the cell, but the damage, in any case, should be kept to a minimum. (A systematic way to do this is to measure the resistance across the electrical leads when the cell is loaded and apply the minimum amount of pressure needed to register a finite resistance value the cell. This method works for diameters 10 mm and greater, otherwise the resistance is too high to be measured by a hand-held multimeter, regardless of the pressure.)

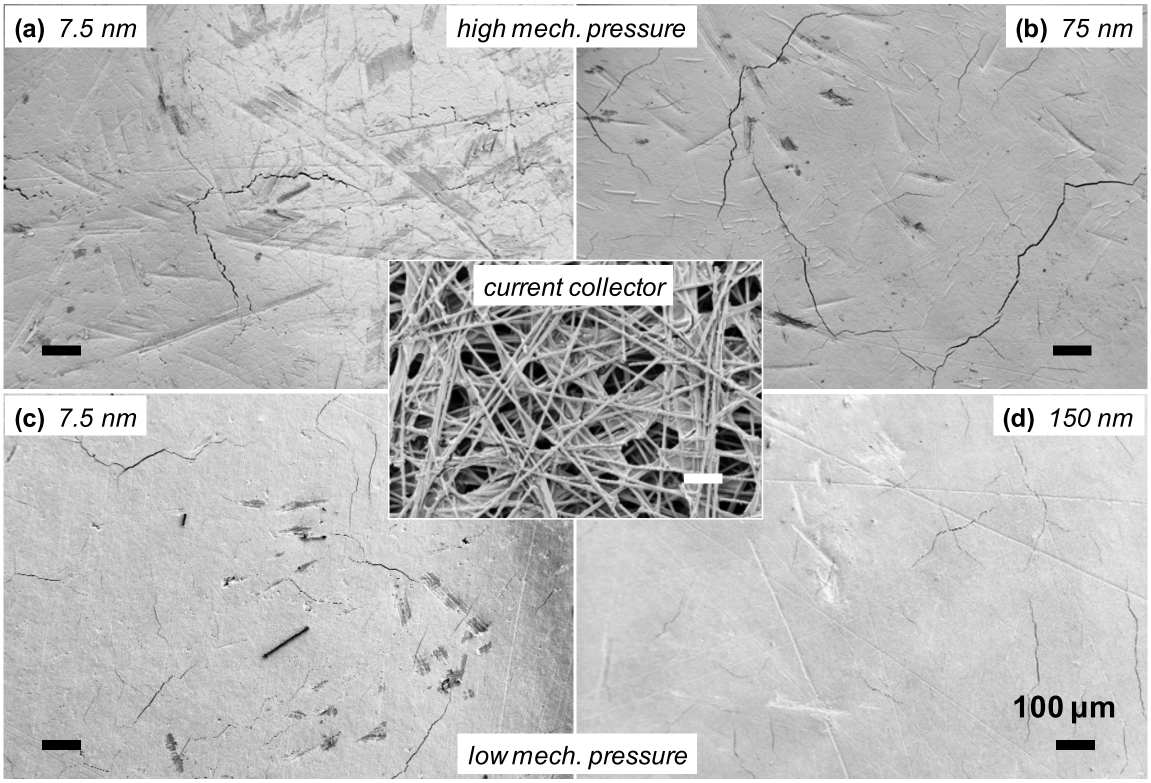

Figure C.12 Pt film quality, after electrochemical characterization, as a function of film thickness and mechanical pressure applied to the cell. (a) and (b) show 7.5 and 75 nm films, respectively, with a relatively high pressure applied. (c) and (d) show 7.5 and 150 nm films, respectively, with a relatively low pressure applied. The center image, shown for the same magnification as (a–d), displays the structure of the carbon fiber paper that was in contact with the cell as a current collector during electrochemical characterization.

C.3 Non-electrode Impedance Responses

C.3.1 Origin of Spurious Electrical Effects

When studying electrode reactions in electrochemical cells, it is necessary to consider spurious contributions to the electrical response. For Pt | CsH_2PO_4 | Pt symmetric cell measurements, inductance contributions from electrical lead wires as well as from instrumentation (e.g., FRA, multiplexer, etc.) are present. The presence of inductance effects can be confirmed by first running a short correction (i.e., with no sample and the electrical leads shorted together). Correction of the raw data can be carried out in one of two ways. If the short correction is adequately represented by the inductor element, then raw experimental data can be corrected by subtract the term $Z_L = i\omega L$ (where L is the inductance value obtained by fitting the short correction data) from the imaginary portion of the data. This was the procedure employed, in this case. If the short correction has other unknown contributions, a point-wise correction would be preferred.

While the contribution of inductance is rather common in electrical measurements, the presence of constriction effects is less frequently addressed. Figure C.13 shows a schematic of the Pt | CsH_2PO_4 | Pt cell and the source of constriction. At extremely high frequencies of voltage perturbation, protons migrate through CsH_2PO_4 with a cross-sectional area that corresponds to the diameter of the CsH_2PO_4 disc. As the frequency is decreased, protons begin to interact with the Pt | CsH_2PO_4 and C | CsH_2PO_4 interfaces, where C denotes the carbon current collector. Because the electrochemical activity of Pt is higher than that of carbon, protons will preferential pass through the Pt | CsH_2PO_4 interface. The resistance associated with the high-frequency constriction arc is attributed to the additional distance that protons must travel to reach the Pt film edge, while the capacitance is due to that at C | CsH_2PO_4. Symmetric cell measurements of C | CsH_2PO_4 | C gives an interfacial capacitance for the C | CsH_2PO_4 interface of ~ 3 μF cm^{-2} compared to 1.1 ± 1.9 μF cm^{-2} for the constriction arcs observed in the impedance spectra for Pt | CsH_2PO_4 | Pt cells with 5–13 mm dia. Pt films.

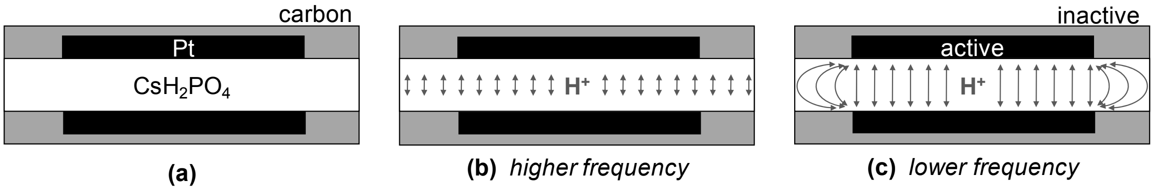

Figure C.13 The constriction effect: (a) no voltage perturbation, (b) high perturbation frequencies at which proton conduction occurs throughout the entire cross-section of CsH_2PO_4, and (c) intermediate frequencies at which protons must pass through a cross-sectional area corresponding to the Pt film area.

C.3.2 Appearance of Constriction Effect

Whether or not the high-frequency constriction arc is visible during an impedance measurement appears to be a function of several parameters. Figure C.14 shows a 19 mm diameter cell with a 10 mm diameter Pt film (75 nm thick) measured using two different frequency response analyzer units, a Solartron Analytical 1250 frequency response analyzer (FRA) coupled to a Princeton Applied Research 273A potentiostat and a Solartron Analytical 1260 FRA. Because the electrical leads in the experimental setup run through a multiplexing unit, the Solartron 1250 (which has a three-probe configuration) gave higher ohmic offsets and higher inductance. The Solartron 1260 has a four-probe configuration and thus minimizes wire inductance and resistance contributions.

The size of the high-frequency arc increased with decreasing film diameters, as shown in the second column of Figure C.17. The resistance of the high-frequency arc (extracted from raw, un-normalized data) was 1.5, 2.6, and 14 Ω for film diameters of 12.6, 10, and 5 mm, respectively. This observation is consistent with constriction; as the film diameter is decreased, the constriction arc increases as the protons in CsH_2PO_4 must travel a greater distance to reach the edge of the Pt film.

When sufficient mechanical pressure was applied such that intimate contact was made between the carbon paper and the CsH_2PO_4 disc, a semi-circular arc appeared at high frequencies. It was observed that when a lower pressure was applied to the cell, the arc decreased in size or disappeared altogether. One explanation for this is that the nature of the $C | CsH_2PO_4$ interface was changed, that is, the capacitance of this interface contained additional contributions from the gas environment due to the increased spacing between the carbon paper and CsH_2PO_4. In any case, the combined effect of mechanical pressure, film diameter and choice of instrumentation can make the appearance of the constriction arc seem rather sporadic and irreproducible, and thus some care must be taken when trying to determine whether a constriction effect exists.

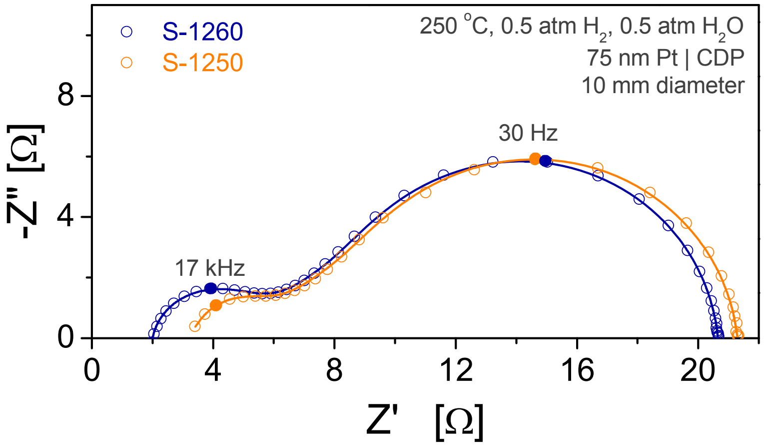

Figure C.14 Impedance response of a Pt | CsH_2PO_4 | Pt symmetric cell measured using two different frequency response analyzers (FRAs). Measurement with the Solartron 1250 FRA (coupled to a potentiostat) results in a higher inductance effect than that with the Solartron 1260 FRA.

C.3.3 Evidence of Constriction Effect

Several observations support the identification of the high-frequency arc in Figure C.14 as that resulting from the constriction phenomenon. As shown in the second column of Figure C.17(b–d) for the Au-Pt layered electrode system, the addition of Au in any configuration did not impact the high-frequency arc, as indicated by the almost perfect overlap of the spectra at high frequencies. This is to be expected, since the configuration of the electrode should not influence constriction.

Since the origin of the constriction arc is due to confinement of proton transport to the Pt | CsH_2PO_4 interface, it is to be expected that the conductivity of CsH_2PO_4 can be extracted using the appropriate impedance characteristics and cell geometry. That is, from Figure C.13b, the ohmic offset at high frequencies corresponds to proton conduction through the entire area of the CsH_2PO_4 disc, whereas the total resistance (offset resistance together with the resistance of the high-frequency arc) corresponds to proton transport through a reduced cross-sectional area, roughly approximated by the Pt film area (Figure C.13c), that is,

$$\sigma_{offset} = \frac{L_{CDP}}{R_{offset} A_{CDP}} \tag{C.1}$$

$$\sigma_{constrict} = \frac{L_{CDP}}{\left(R_{offset} + R_{HF}\right) A_{Pt}} \tag{C.2}$$

Where σ_{offset} is the conductivity calculated (in the cases where a high-frequency arc surfaces) from the ohmic offset of the impedance, R_{offset}, and the area of the 19 mm CsH_2PO_4 disc, while $\sigma_{constrict}$ is the conductivity calculated from the ohmic offset and the resistance of the high-frequency arc, R_{HF}. From averaging over all the cells that displayed a reliable constriction arc (specifically, those with of 5–12.6 mm diameter Pt films and measured using the Solartron 1260 FRA with sufficiently high mechanical pressure applied to the cells), 15 cells in total, the value calculated for σ_{offset} was $1.8 \pm 0.6 \times 10^{-2}$ S cm^{-1} at 250 ºC. From all cells in which sufficient pressure was applied (such that there was no erratic jumps in the ohmic offset, as discussed in C.2.4), $\sigma_{constrict}$ was found to be $2.3 \pm 0.7 \times 10^{-2}$ S cm^{-1} at 250 ºC. These values are consistent with that reported for proton transport in CsH_2PO_4, 2.2×10^{-2} S cm^{-1} at 240 ºC.[10]

The dependence of the high-frequency arc on environmental parameters, such as gas partial pressure and temperature, provides additional support of the constriction phenomenon. As the hydrogen partial pressure is decreased, the low-frequency electrode arc (half-teardrop shape) increases in resistance, as expected (Figure C.15). In contrast, the high-frequency arc and the ohmic offset are unchanged, with the arcs perfectly overlapping with one another as the gas environment is varied. Similar observations are made for when the water partial pressure was varied (not shown). The observation of the pH_2 and pH_2O reaction orders of zero for R_{HF} and R_{offset} is consistent with the behavior of CsH_2PO_4, that is, the migration of protons in CsH_2PO_4 does not depend on the gas composition. Furthermore, the temperature dependence of the high-frequency arc is, to within error, the same as that for the ohmic offset (Figure C.16). Activation energies of 41 and 38 kJ mol^{-1} for R_{HF} and R_{offset}, respectively, agree with values for proton migration in superprotonic CsH_2PO_4, 40 kJ mol^{-1} (0.42 eV).[10]

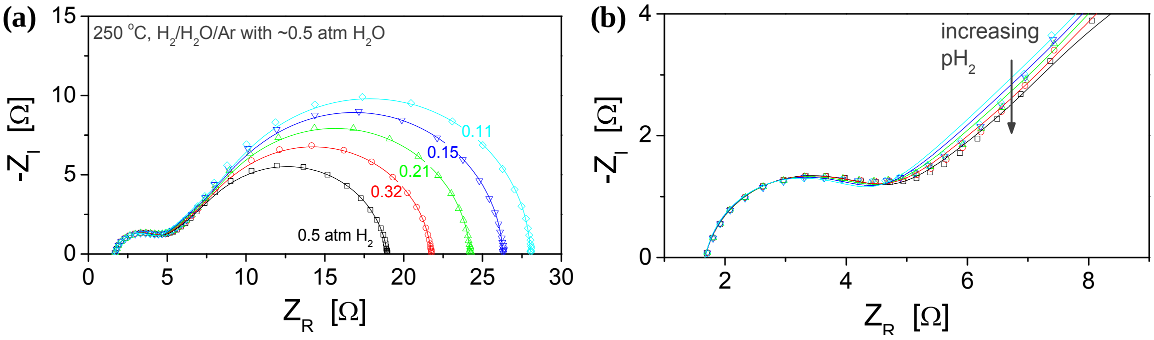

Figure C.15 Representative impedance spectra for a Pt | CsH_2PO_4 | Pt cell that (a) displays both an electrode response (a half-teardrop for a 75 nm thick and 10 mm diameter Pt film) and a high-frequency arc. (b) The hydrogen partial pressure has no effect on the ohmic offset and the high-frequency arc.

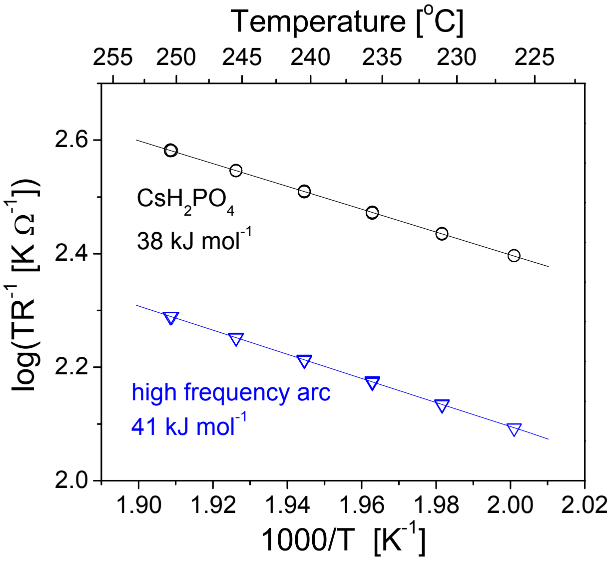

Figure C.16 Temperature dependence of the ohmic offset (CsH_2PO_4) and the width of the high-frequency arc. $pH_2 \approx pH_2O \approx 0.5$ atm

C.4 Layered Pt-Au Film Electrodes

As discussed in Chapter 3, employing films of a catalytically inactive materials such as gold can be used to further probe the hydrogen electro-oxidation mechanism in the metal | CsH_2PO_4 system. In this section, we report additional geometries of Pt-Au films examined under uniform H_2-H_2O environments.

Figure C.17 and Table C.1 summarizes the results of the various Pt-Au geometries examined. Ignoring the high-frequency constriction arc visible in Figure C.17(b–c), it is immediately clear that the electrode configurations shown in Figure C.17(a–c) retained the 45° regime attributed to diffusion, indicating that diffusion through the Pt film is still the preferred pathway for hydrogen oxidation. However, the presence of the large blocking arc at intermediate-to-low frequencies indicates that Au has a significant impact on the total electrode resistance. Configurations (a) and (b) in Figure C.17 and Table C.1 show the effect of the Au film thickness at the metal | gas interface.

When the Au film thickness was increased from (nominally) 10 nm to 50 nm, the blocking arc increased approximately four-fold in width. The characteristic frequency dropped, but the capacitances of the two arcs were comparable, indicating that the change in the characteristic frequency of the process is a consequence of the change in the resistance rather than the capacitance of the process. All other parameters, including gas partial pressure dependences and activation energies were comparable. Although the increase in the resistance of the blocking arc with film thickness indicates diffusion through Au as the corresponding process, it is important to keep in mind that the coverage of the Pt surface using 10 nm Au may be poor and, therefore, the smaller resistance associated with the 10 nm blocking films may be due to partially exposed Pt.

To probe the surface activity of the metal | gas interface, we compared configurations (b) and (c) in Figure C.17 and Table C.1. Adding a 7.5 nm Pt layer on top of a Au | Pt | CsH_2PO_4 cell resulted in a decrease in the resistance, almost by a factor of two. The capacitance increased while the characteristic frequencies were virtually unchanged. The partial pressure dependences and the activation energies were comparable between the two configurations. The observation that the resistance of the process improved only by a factor of two indicates that the Au | gas interface was likely not the rate-limiting step in (b) since we expect the surface activity at Pt | gas to be significantly greater than that at Au | gas. Furthermore, the comparable characteristic frequencies between (b) and (c) also suggest that the rate-limiting step has not changed.

Unlike configurations (a–c), configuration (d), i.e., Pt | Au | CsH_2PO_4, did not display the 45° regime (characteristic of diffusion) at high frequencies. This implies that the arc generated as a result adding Au can be attributed to a process occurring at either the Au | CsH_2PO_4 or Au | Pt interface. Compared to configuration (a) in which 10 nm Au was placed at the metal | gas interface, Au at the metal | CsH_2PO_4 interface, configuration (d), displayed a characteristic frequency that was over one order of magnitude larger. The resistances of their blocking arcs were comparable, indicating that the characteristic frequency difference results from capacitive differences.

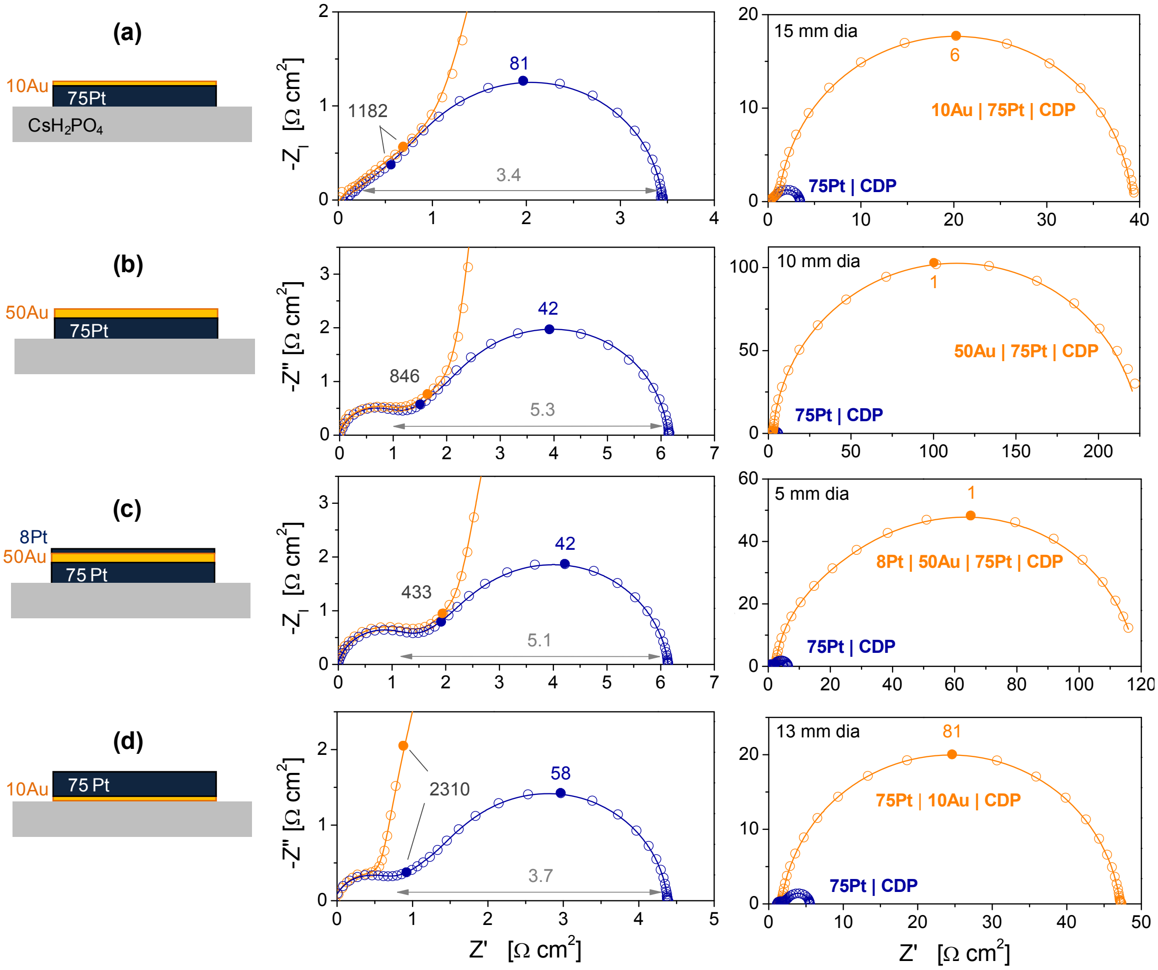

Figure C.17 The Pt-Au layered thin film electrode system at 250 ºC with $pH_2 \approx pH_2O \approx 0.5$ atm: (a) 10Au | 75Pt | CDP, (b) 50Au | 75Pt | CDP, (c) 8Pt | 50Au| 75Pt | CDP, and (d) 75Pt | 10Au | CDP. CDP denotes CsH_2PO_4, and the number preceding the metal denotes the film thickness in nm. The half-cell configuration is shown in the left column. The second and third columns show the corresponding high and low-frequency behavior, respectively. The Warburg resistance, R_0, is indicated by the arc width, and select frequencies *f* are labeled.

Table C.1 Summary of extracted fit parameters for the low-frequency arc generated by the addition of Au to the Pt | CsH_2PO_4 cell. Values in bold correspond to the spectra plotted in Figure C.17. For comparison, values for the 7.5 nm Pt film electrode are also shown. CDP = CsH_2PO_4, HF = high frequency, $\tilde{R}$ = area-normalized resistance, C_{equiv} = equivalent capacitance, ω_0 = characteristic frequency, E_A = activation energy.

	Cell Geometry	$\tilde{R}$ [Ω cm^2]	C_{equiv} [μF cm^{-2}]	ω_0 [Hz]	**45° @ HF?**	$p\mathrm{H_2}$	$p\mathrm{H_2O}$	E_A [kJ mol^{-1}]
	7.5Pt | CDP	3	132	2740	Y	0.74	0.30	31
(a)	**10Au | 75Pt | CDP**	**38**–70	**749**–832	**17**–35	Y	.51–.71	–0.03	48
(b)	**50Au | 75Pt | CDP**	193–**227**	763–**783**	**5.6**–6.8	Y	.61–.78	–0.01	48
(c)	**7.5Pt | 50Au | 75Pt | CDP**	115–**119**	1135–**1155**	**7.3**–7.6	Y	.77–.80	0.02	50
(d)	**75Pt | 10Au | CDP**	**46**–53	**43**–46	413–**515**	N	.55–.64	0.06	54
(e)	**(HF arc) 50Au | CDP**	476–833	41–47	73–36	—	—	—	—
(f)	**(LF arc) 50Au | CDP**	82–170	37100–39200	0.46–0.21	—	—	—	—

We also electrochemically characterized 10 and 50 nm Au films deposited directly onto CsH_2PO_4 in order to understand hydrogen electro-oxidation at Au | CsH_2PO_4 and further clarify the processes occurring in the Pt-Au bilayer systems. In the case of 10 nm Au films, the electronic connectivity of the films degraded after electrochemical testing. The sheet resistances measured for the Au films were reasonable initially, comparable to values for as-deposited 7.5 nm Pt films, but after electrochemical testing, the sheet resistances were too high to be measured using a hand-held multimeter. The impedance response was consistent with this behavior; the currents were too small to be measured using a Solartron 1260 unit, implying an electrode resistance of at least several MΩ. On the other hand, 50 nm films remained intact and retained its sheet connectivity and low sheet resistance after electrochemical characterization. The total electrode resistances for 50 nm Au films were 390–710 Ω cm^2. The impedance response was comprised primarily of two arcs (Figure C.18a), a large arc at high frequencies with a resistance of 476–833 Ω cm^2 and a smaller arc at low frequencies with a resistance of 82–170 Ω cm^2. These resistance values are listed in Table C.1 for comparison to the Pt-Au layered electrode systems. At very high frequencies, an additional process is visible (Figure C.18b); at present, it is unclear whether this arc is due to diffusion (suggested by the shape) or constriction (as indicated by the high characteristic frequency).

The observation of such a large resistance, relative to the values of the blocking arcs exhibited by the Pt-Au systems, is somewhat surprising and suggests that the Pt-Au systems are more active. Since 50 nm Au in configuration (b), Au | Pt | CsH_2PO_4, displayed lower electrode resistance than 50 nm Au in Au | CsH_2PO_4, the source of the high resistance in the Au | CsH_2PO_4 cell is likely a process that is not located at the Au | gas interface. To confirm if the source of the high resistance is, indeed, a process at the Au | CsH_2PO_4 interface, it would be necessary construct a similar to configuration (d), i.e., Pt | Au | CsH_2PO_4 | Au | Pt cell, but with a 50 nm layer of Au rather than a thin 10 nm layer. The observation that 10 nm Au alone degrades significantly may mean that 10 nm Au films may not remain interconnected when deposited under (or on top of) Pt. Thus, the observation of a lower resistance in configuration (d) compared to that for 50 nm Au alone presently does not provide enough information for drawing any meaningful conclusions. Note that although interdiffusion of bulk metals at temperatures near 250 ºC is expected to be negligible, it cannot be ruled out in nanograined thin film systems. Thus, it remains a possibility that increased activity of Pt-Au bilayer electrodes compared to Au alone is due to alloy formation.

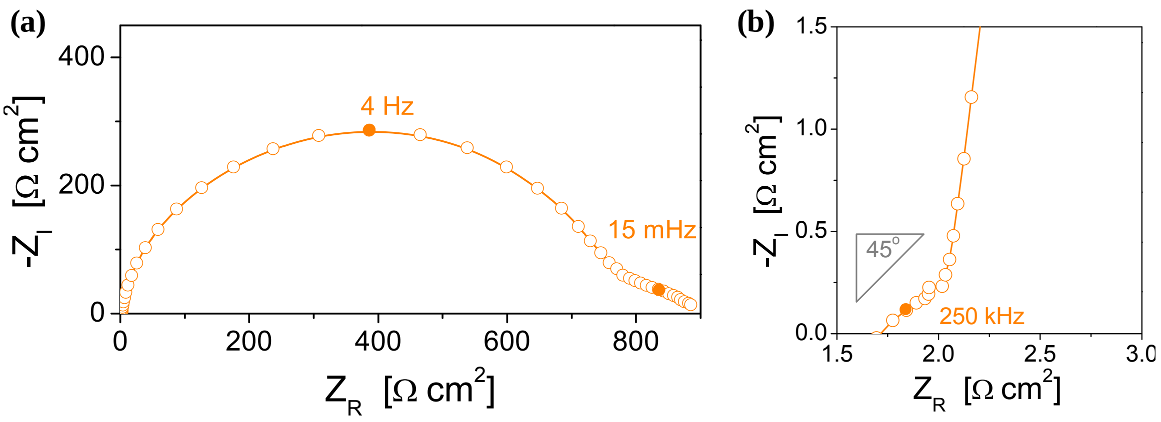

Figure C.18 Impedance spectra of a Au | CsH_2PO_4 | Au symmetric cell, collected at 250 ºC with $pH_2 \approx pH_2O \approx 0.5$ atm, (a) comprised primarily of two arcs, with (b) an additional low-resistance process visible high frequencies.

C.5 Electrolyte Effects: $Cs_{0.25}Rb_{0.75}H_2PO_4$ vs. CsH_2PO_4

To clarify the role of charge transfer at the Pt | solid acid electrolyte interface in the reaction mechanism, we perform impedance studies of the Pt | $Cs_{0.25}Rb_{0.75}H_2PO_4$ | Pt system. The CsH_2PO_4-RbH_2PO_4 system has been shown to form solid solutions up to a Rb content of $x \approx 0.8$.[113] The proton conductivity of $Cs_{1-x}Rb_xH_2PO_4$ ($x < 0.8$) is approximately 2–3 times lower than that of the end-member, CsH_2PO_4, and the lattice parameters and hydrogen bond lengths vary monotonically with Rb content.[113, 124] We suspect that the change in the properties of $Cs_{1-x}Rb_xH_2PO_4$ with Rb content makes this solid solution system valuable for exploring the effect of the Pt | electrolyte interface on the rate-limiting step of hydrogen electro-oxidation. In this section, we compare the impedance response of Pt | $Cs_{0.25}Rb_{0.75}H_2PO_4$ to Pt | CsH_2PO_4.

C.5.1 150 nm Platinum Films

The Nyquist spectra for 150 nm Pt film electrodes (Figure C.19) deposited on CsH_2PO_4 and $Cs_{0.25}Rb_{0.75}H_2PO_4$, show notable differences in arc shape and width. At high frequencies, the spectra behavior similarly, displaying a slope of 45º. However, at intermediate frequencies, the spectrum for Pt | $Cs_{0.25}Rb_{0.75}H_2PO_4$ | Pt deviates from that for Pt | $Cs_{0.25}Rb_{0.75}H_2PO_4$ | Pt, extending to an additional arc at low frequencies. The impedance spectrum for Pt | CsH_2PO_4, as shown in Chapter 3, can be fitted to the distributed finite-length Warburg (dFLW) model. For the impedance response of Pt | $Cs_{0.25}Rb_{0.75}H_2PO_4$ | Pt, an additional (empirical) RQ element was added in series to the dFLW element to account for the low-frequency arc. Extracted values are shown in Table C.2. The extracted fit parameters for Pt | CsH_2PO_4 | Pt and the dFLW portion of Pt | $Cs_{0.25}Rb_{0.75}H_2PO_4$ | Pt spectra are comparable, with Warburg resistances of 17 and 14 Ω cm^2, respectively. The characteristic frequencies (26–36 Hz) and pH_2 reaction orders (0.32–0.34) are also comparable, with differences in the characteristic frequencies being attributed to errors from the fitting of convoluted processes in the Pt | $Cs_{1-x}Rb_xH_2PO_4$ | Pt system. The additional low-frequency arc present in the Pt | $Cs_{0.25}Rb_{0.75}H_2PO_4$ | Pt spectrum had a resistance of 13 Ω cm^2, with a notably different pH_2 dependence of 0.65. The ohmic offset (not shown) yielded a proton conductivity of 8×10^{-3} S cm^{-1} for $Cs_{0.25}Rb_{0.75}H_2PO_4$ at 255 ºC, almost one-third of that for CsH_2PO_4 at the same temperature, 2.5×10^{-2} S cm^{-1}.

The presence of an additional feature at low frequencies suggests that the use of $Cs_{0.25}Rb_{0.75}H_2PO_4$ as the electrolyte influences the rate-limiting step(s) for hydrogen electro-oxidation. Based on Pt | CsH_2PO_4 | Pt data for thick Pt films for which diffusion of hydrogen was found to be the rate-limiting step, small perturbations at the Pt | electrolyte interface, is not expected to influence the rate-limiting step of hydrogen diffusion through the Pt film. Our observation here implies that a step occurring at or affected by the Pt | $Cs_{0.25}Rb_{0.75}H_2PO_4$ interface is significantly slower than in the Pt | CsH_2PO_4 system. That is, the additional low-frequency arc in Pt | $Cs_{0.25}Rb_{0.75}H_2PO_4$ spectrum, with a resistance of 13 Ω cm^2, corresponds to a process that occurs at or near the Pt | $Cs_{0.25}Rb_{0.75}H_2PO_4$ interface. This interfacial resistance value is approximately six times greater than the resistance, 2.2 Ω cm^2, of the interfacial steps occurring in Pt | CsH_2PO_4 | Pt (Figure 3.12). Although the pH_2 reaction order of 0.65 for the Pt | $Cs_{0.25}Rb_{0.75}H_2PO_4$ interfacial step is comparable to that observed for 7.5 nm Pt films on CsH_2PO_4, it is not yet clear whether these two interfacial processes, with resistances of 13 and 2.2 Ω cm^2, are the same. In the next section, experiments with 7.5 nm films are examined, in an attempt to further clarify this observed phenomenon.

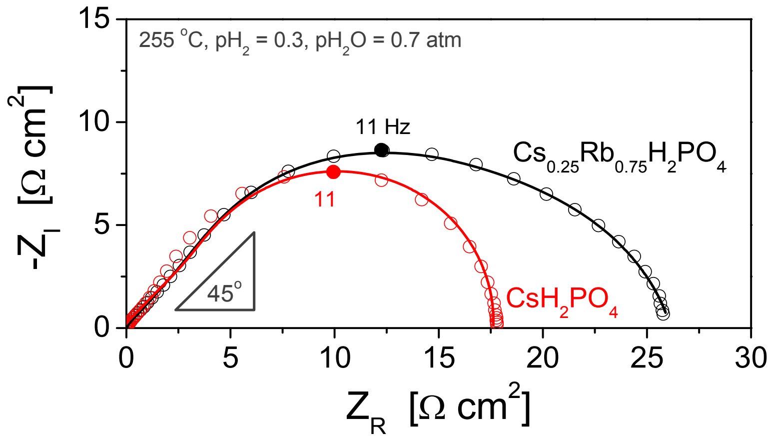

Figure C.19 Nyquist plot for 150 nm Pt film electrode on CsH_2PO_4 and on $Cs_{0.25}Rb_{0.75}H_2PO_4$ polycrystalline electrolytes. Arc shape and widths were reproducible across three different samples for each substrate. Lines are fits to dLFW (for CsH_2PO_4) and to dFLW in series with RQ (for $Cs_{0.25}Rb_{0.75}H_2PO_4$).

Table C.2 Comparison of fitted parameters for 150 nm Pt film electrodes on CsH_2PO_4 (CDP) and $Cs_{0.25}Rb_{0.75}H_2PO_4$ (CRDP75) at 255 °C in 0.3 atm H_2, 0.7 atm H_2O. $\tilde{R}$ = area-normalized resistance, ω_0 = characteristic frequency

	Warburg diffusion (dFLW)			*Low-frequency process*		
Cell	**$\tilde{R}$ [Ω cm^2]**	**ω_0 [Hz]**	**pH_2 rxn order**	**$\tilde{R}$ [Ω cm^2]**	**ω_0 [Hz]**	**pH_2 rxn order**
Pt | CDP	17	26	0.34	N/A	N/A	N/A
Pt | CRDP75	14	36	0.32	13	20	0.65

C.5.2 7.5 nm Platinum Films

Pt | $Cs_{0.25}Rb_{0.75}H_2PO_4$ | Pt cells with 7.5 nm Pt films yielded impedance spectra that were symmetric in shape, as shown for both 19 and 9.3 mm Pt films in Figure C.20a and Figure C.20b, respectively. The symmetric nature of the arcs is consistent with an electrode reaction mechanism dominated by an interfacial processes (as demonstrated for 7.5 nm films on CsH_2PO_4 in Chapter 3). Unlike 150 nm Pt film electrodes which displayed reproducible behavior, 7.5 nm electrodes were inconsistent in their electrode arc widths. The electrode resistance for Pt | CsH_2PO_4 (Table C.3) varied from 3.4 to 7.7 Ω cm^2, while that for Pt | $Cs_{0.25}Rb_{0.75}H_2PO_4$ varied from 0.7 to 20 Ω cm^2 for 9.3 and 19 mm films, respectively. From a comparison of these values, it is clear that the effect of changing the electrolyte substrate, although irreproducible, is non-negligible. The characteristic frequencies vary notably between arcs, however, the capacitances of the processes for all cells tested are similar, implying that the observed change in the characteristic frequency of the rate-limiting step is a consequence of a change in the resistance rather than the capacitance of the process.

While the scatter in the electrode resistance values for Pt | CsH_2PO_4 may be acceptable (a factor of ~ 2), that for Pt | $Cs_{0.25}Rb_{0.75}H_2PO_4$ is quite significant (a factor of

~ 30). This is not surprising since Rb incorporation leads to an increasingly plastic superprotonic phase. In the laboratory, application of mechanical pressure to make electrical connection for conductivity measurements led us to observe that under comparable pressures, a greater extent of deformation (i.e., flattening) of dense $Cs_{1-x}Rb_xH_2PO_4$ discs occurs for compounds with larger x. Thus, for a given mechanical pressure applied to the symmetric cells (for current collection), those based on $Cs_{0.25}Rb_{0.75}H_2PO_4$ substrates deformed more than those based on CsH_2PO_4 substrates. Physical observations of the symmetric cells before and after testing suggest that the carbon paper current collector damaged $Cs_{0.25}Rb_{0.75}H_2PO_4$ cells to a greater extent. Furthermore, based on SEM image analysis of films on CsH_2PO_4 (Figure C.12), we can conclude that thicker films generally remained more intact under mechanical pressure, consistent with the reproducibility of the data for 150 nm films. On the other hand, 7.5 nm films on $Cs_{0.25}Rb_{0.75}H_2PO_4$ are more easily damaged by the pressure of the carbon paper (Figure C.12) given the lack of stability for 1.5–4.5 nm films (Figure C.6) and the expectation that higher plasticity (of $Cs_{0.25}Rb_{0.75}H_2PO_4$) implies a more mobile/ductile substrate. Thus, in order to accurately determine the effect of $Cs_{0.25}Rb_{0.75}H_2PO_4$ on the rate-limiting step, determination of an optimal mechanical pressure for current collection is required.

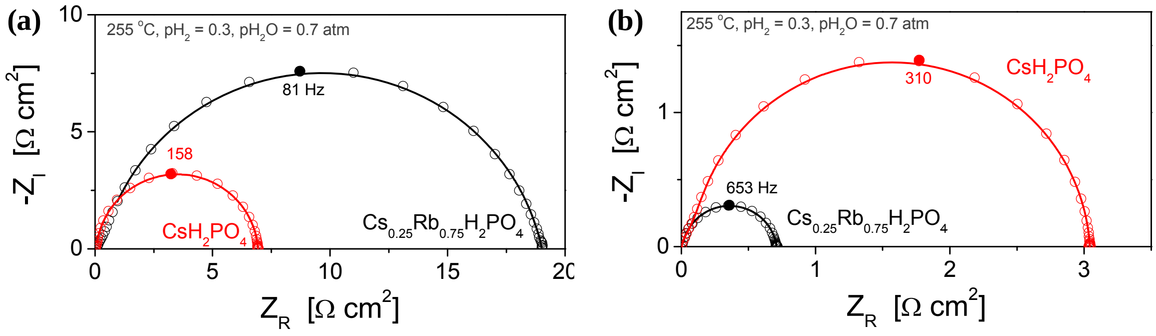

Figure C.20 Nyquist plots for 7.5 nm Pt films deposited on CsH_2PO_4 and on $Cs_{0.25}Rb_{0.75}H_2PO_4$ polycrystalline electrolytes. Both the cell and Pt film diameters are (a) 19 mm and (b) 9.3 mm. The arc shapes are similar, but the widths of the arcs vary significantly

Table C.3 Comparison of extracted fit parameters for 7.5 nm Pt film electrodes on CsH_2PO_4 (CDP) and $Cs_{0.25}Rb_{0.75}H_2PO_4$ (CRDP75) at 255 ºC in 0.3 atm H_2 and 0.7 atm H_2O. $\tilde{R}$ = area-normalized resistance, C_{equiv} = equivalent capacitance, ω_0 = characteristic frequency

Cell	**Dia.** [mm]	$\tilde{R}$ [Ω cm^2]	C_{equiv} [µF cm^{-2}]	ω_0 [Hz]	**pH$_2$ rxn order**
Pt | CDP	19.1	7.7	157	880	0.86
Pt | CDP	9.3	3.4	144	2325	--
Pt | CRDP75	19.1	20	121	411	0.89
Pt | CRDP75	9.3	0.7	135	10415	--

C.6 Effect of Environmental Parameters

In this section, we show several representative plots to illustrate how activation energy and the pH$_2$ reaction order values, reported in Chapter 3, are extracted. The reaction order for pH$_2$O is also reported. As is the case for chemical reactions, the reaction rate of electrochemical reactions depends on the amount of reactant/product available (Appendix A.3). In the case of hydrogen electro-oxidation, hydrogen partial pressure, pH$_2$, is expected to affect the reaction rate, and, furthermore, because of the high water partial pressure of the gas environment, we also consider the effect of water partial pressure, pH_2O. Thus, the reaction rate can be expressed as:

$$\textit{reaction rate} \propto R_E^{-1} \propto pH_2{}^n pH_2O^m \qquad \text{(C.3)}$$

where R_E is the resistance of an electrode process, and n and m are the reaction orders of pH_2 and pH_2O, respectively. The reaction orders, n and m, are determined independently, specifically, by holding pH_2O constant while varying pH_2 (to extract n) and holding pH_2 constant while varying pH_2O (to extract m). Figure C.21 and Figure C.22 are plots showing the effect of pH_2 and pH_2O on the (inverse) resistances of the electrode, CsH_2PO_4 and constriction processes in Pt | CsH_2PO_4 | Pt, for 7.5 and 75 nm films, respectively. (Processes associated with the bulk of the electrolyte are not expected to depend on gas partial pressure but are plotted here for reference.) For both cells, processes related to proton conduction in CsH_2PO_4, i.e., the ohmic offset and the high-frequency constriction arc, vary negligibly with gas partial pressure. These results were observed for virtually all the cells tested. The average values, extracted from plots for 20–30 samples are shown in Table C.4. In some cases (Figure C.21a being an example), the dependence of the constriction arc is larger than expected, particularly when the constriction effect is small, because of a larger fitting error of the constriction arc as the low-frequency electrode arc increases in size. This is consistent with the partial pressure dependence for the two processes being equal be opposite in sign.

Table C.4 Hydrogen and water partial pressure dependences of electrolyte-related processes.

	ohmic offset	**high-frequency constriction**
$\boldsymbol{pH_2}$	–0.02 ± 0.05	–0.12 ± 0.09
$\boldsymbol{pH_2O}$	0.0 ± 0.1	0.02 ± 0.08

In the case of 75 nm Pt (Figure C.21), the electrode process exhibited a dependence on pH_2, with a slope of ~ 0.54 (average ≈ 0.45 for 75 nm films, Figure 3.8) while the pH_2O reaction order was much lower, 0.16 (average = 0.30 ± 0.09). In the case of 7.5 nm Pt (Figure C.22), the electrode exhibited a pH_2 reaction order that is notably higher, 0.80, (average ≈ 0.75, Figure 3.8) than that for thicker films and the pH_2O dependence is 0.22 (with an average value of 0.30 ± 0.06) comparable to that for 75 nm Pt.

Given a known rate-limiting step of hydrogen diffusion (in the case of 75 nm Pt films), a pH_2 reaction close to 0.5 is expected (Appendix A.3). That the pH_2 reaction order is significantly larger for 7.5 nm films is consistent with the observed change in the rate-limiting step (Figure 3.8). Presently, identification of this rate-limiting process is not possible, although it is noteworthy that dissociative adsorption of hydrogen can, to first order approximation, yield a slope close to unity. (Appendix A.3)

The observation of a pH_2O dependence is somewhat surprising because it is not immediate clear the role of water in the reaction mechanism, particularly in the hydrogen diffusion pathway. The observed pH_2O dependence was confirmed to be a small positive value consistently observed across ~ 30 samples, with an average reaction order of ~ 0.30 across all film thicknesses. Without the capability to explore a wider pH_2O range, it is not possible to confirm the role of water in the reaction mechanism. In Appendix A.3, we assume that water influences the reaction rate by occupying surface sites on the metal; however, this results in a negative reaction order for pH_2O, opposite of experimental observations.

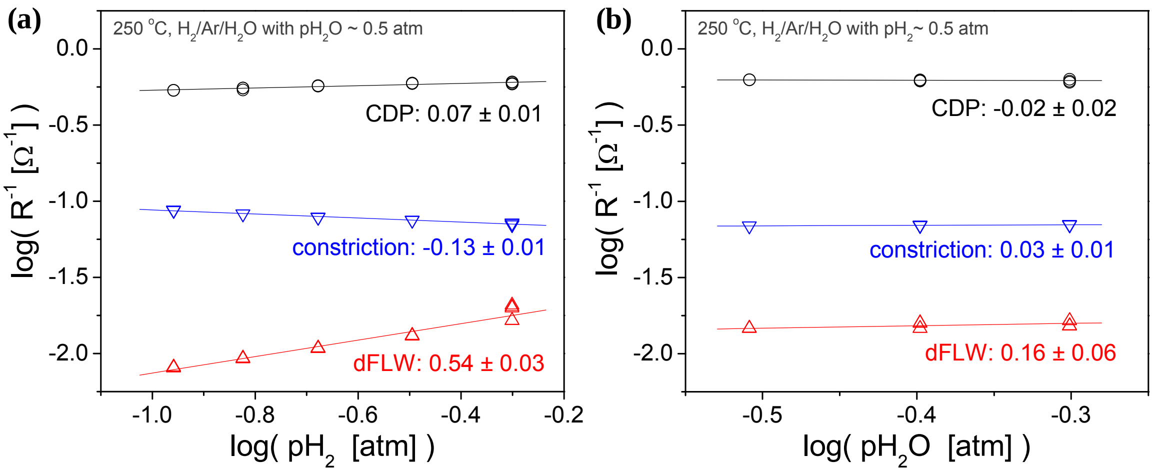

Figure C.21 Partial pressure dependence for Pt | CsH_2PO_4 | Pt (75 nm, 5 mm Pt film) at 250 ºC. Plots of inverse resistance as a function of (a) pH_2 at constant pH_2O and (b) pH_2O at constant pH_2.

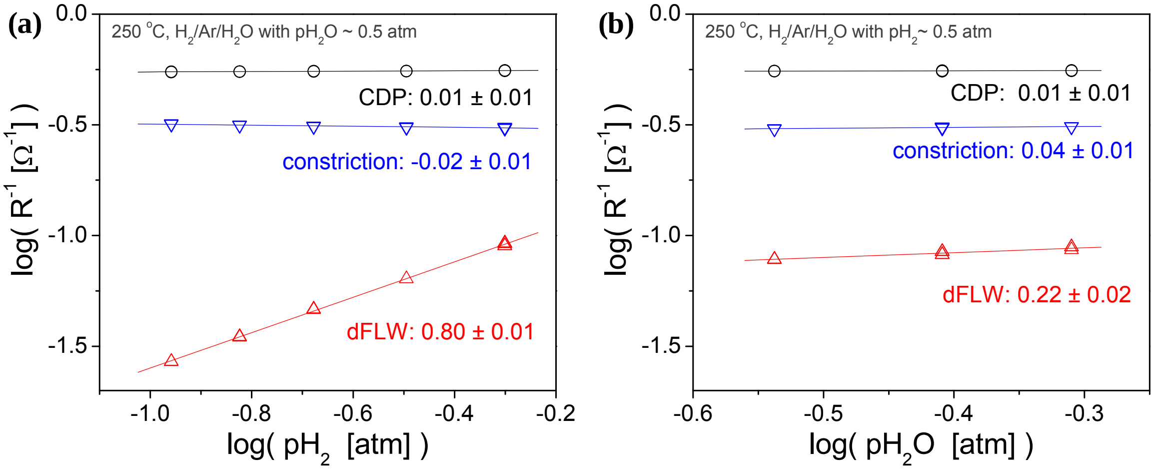

Figure C.22 Partial pressure dependence for Pt | CsH_2PO_4 | Pt (7.5 nm, 10 mm Pt film) at 250 ºC. Plots of inverse resistance as a function of (a) pH_2 at constant pH_2O and (b) pH_2O at constant pH_2.

Figure C.23 and Figure C.24 show the Arrhenius plots for 75 and 7.5 nm Pt films, respectively, in the Pt | CsH_2PO_4 | Pt system. In the case of the 75 nm films (Figure C.23a), we plot $R_E^{-1} \times T$ rather than R_E^{-1} because both proton conduction through CsH_2PO_4 and hydrogen diffusion through Pt depend on temperature,

$$\frac{1}{R_E} \propto \frac{1}{T}\exp\left(\frac{-E_A}{RT}\right) \tag{C.4}$$

where R_E is the resistance of the electrode process, E_A is the activation energy and R and T have their usual meanings. In this case, only from a plot of $R_E^{-1} \times T$ can you extract the correct value of the activation energy. The activation energies for proton conduction through CsH_2PO_4, extracted from the ohmic offset and the high-frequency constriction arc, are 40 and 42 kJ mol^{-1}, respectively, both in good agreement with that reported in literature, 0.42 eV or 41 kJ mol^{-1}.[10] To extract the activation energy for hydrogen diffusivity, the inverse of the characteristic timescale, τ, (or characteristic frequency) is plotted because

$$D_{\mathrm{H}} = \frac{{L_F}^2}{\tau} = D_{\mathrm{H}}^0 \exp\left(\frac{-Q}{RT}\right) \tag{C.5}$$

where D_{H} is the diffusion coefficient for hydrogen in Pt, L_F is the thickness of the Pt film, D_{H}^0 is the pre-exponential constant, and Q is the activation energy. From Figure C.23b, the activation energy for diffusion was found to be ~ 48 kJ mol^{-1}.

In the case of cells with 7.5 nm films, the rate-limiting step hydrogen electro-oxidation has not been identified, and thus, the more general approach of plotting R_E^{-1} rather than $R_E^{-1} \times T$ was used. (Figure C.24) The temperature dependence for the CsH_2PO_4-related processes are also plotted this way to enable comparison to the electrode process. However, the true activation energies are extracted by plotting $R_E^{-1} \times T$; these values are indicated in parentheses in the figure.

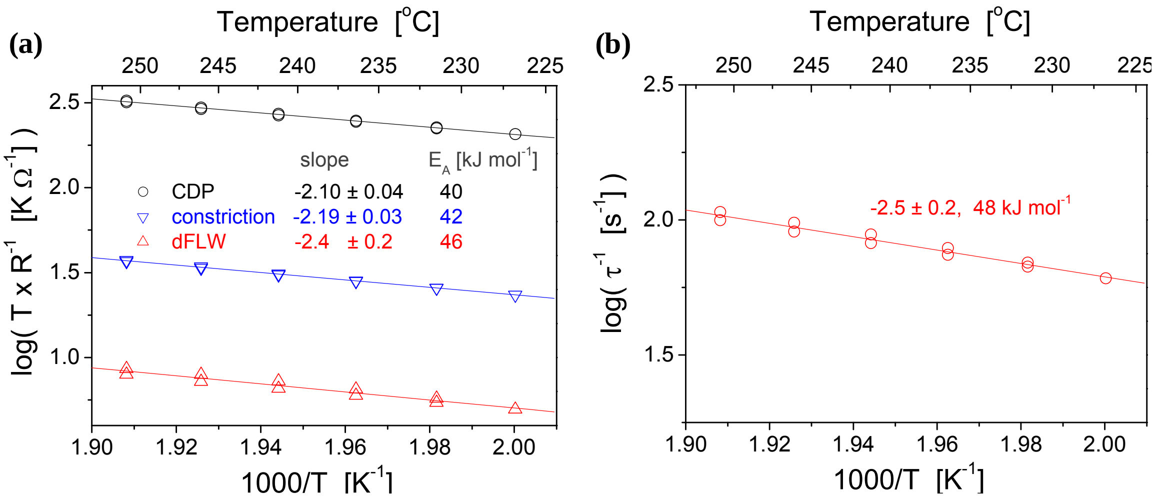

Figure C.23 Arrhenius behavior of Pt | CsH_2PO_4 | Pt (75 nm, 5 mm Pt film) for $pH_2 \approx pH_2O \approx 0.5$ atm: (a) $R_E^{-1} \times T$ as a function of inverse temperature for proton conduction in CsH_2PO_4 and H diffusion in Pt, and (b) inverse characteristic timescale for hydrogen diffusion, for extraction of the activation energy for hydrogen diffusivity, $D_H \propto \tau^{-1}$.

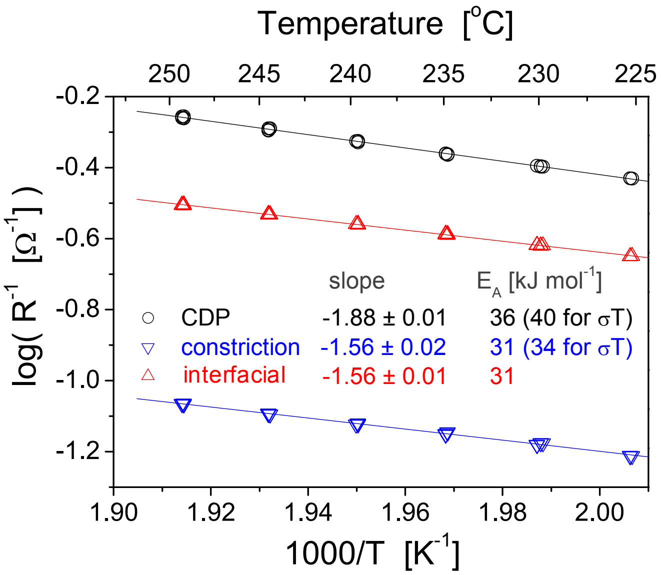

Figure C.24 Arrhenius behavior of Pt | CsH_2PO_4 | Pt (7.5 nm, 10 mm Pt film) for $pH_2 \approx pH_2O \approx 0.5$ atm. Because the electrode rate-limiting step has not been identified, R_E^{-1} is plotted as a function of inverse temperature. The activation energies correspond to $R_E^{-1} \times T$ for the CsH_2PO_4 and constriction processes are indicated in parentheses.

C.7 Role of the Superprotonic Phase Transition in Electrode Kinetics

We can utilize phase transformation characteristics of CsH_2PO_4 to provide additional insight into electrochemical reactions. Specifically, because the proton conductivity (or conduction mechanism) changes drastically across the phase transition, such a change is expected to have a significant impact on the electrochemistry that occurs at the metal | CsH_2PO_4 interface.

C.7.1 Temperature Dependence

Figure C.25 shows the Pt | CsH_2PO_4 | Pt cell response for the temperature profile shown. At temperatures above and below the phase transition temperature, the temperature was increased at 5 ºC intervals, and the resistances of the CsH_2PO_4 and the electrodes change with temperature in a step-wise fashion. At the phase transition temperature, estimated to be ~ 221 ºC on cooling, the equilibration of the electrode and electrolyte resistances take significantly longer times. With the temperature held at 221 ºC, between hour 8 and hour 22 (Figure C.25a), CsH_2PO_4 transforms slowly, with a majority transformed by hour 12. The electrode resistance tracks that for CsH_2PO_4, particularly noticeable at hour 8 at which both the CsH_2PO_4 and the electrode resistances exhibit jumps in their values due to a slight decrease in temperature from 222 to 221 ºC. The steady-state values for resistance are used to generate an Arrhenius plot of inverse resistance (Figure C.25b). In qualitative agreement with Figure C.25a, the Arrhenius plot shows a sudden jump in all steady-state resistance values across the phase transition. At superprotonic temperatures, the activation energies were ~ 40 and ~ 38 kJ mol^{-1} for the ohmic offset and high-frequency constriction processes, respectively, (i.e., CsH_2PO_4) and ~ 30 kJ mol^{-1} for the electrode process. At temperatures below the phase transition temperature, two arcs appeared in the impedance response (not shown), corresponding to the electrolyte and electrode processes. (At temperatures below the phase transition, proton conduction through CsH_2PO_4 is slow and appears as an arc in the Nyquist spectrum.[10]) The electrolyte and the electrode processes exhibit comparably high activation energies of 90 and 105 kJ mol^{-1}.

The two plots in Figure C.25, from two different cells, are representative of the temperature behavior of all Pt cells characterized in this study. The change in the rate-limiting step across the phase transition and apparent correlation between the electrode and electrolyte behavior below the phase transition suggest that the rate-limiting step for H_2 oxidation over Pt is related to proton transport. This hypothesis is not unreasonable; as proton conduction in CsH_2PO_4 becomes slower, the rate-limiting process at high temperatures (i.e., hydrogen diffusion through Pt) is overtaken by slow charge transfer at Pt | CsH_2PO_4.

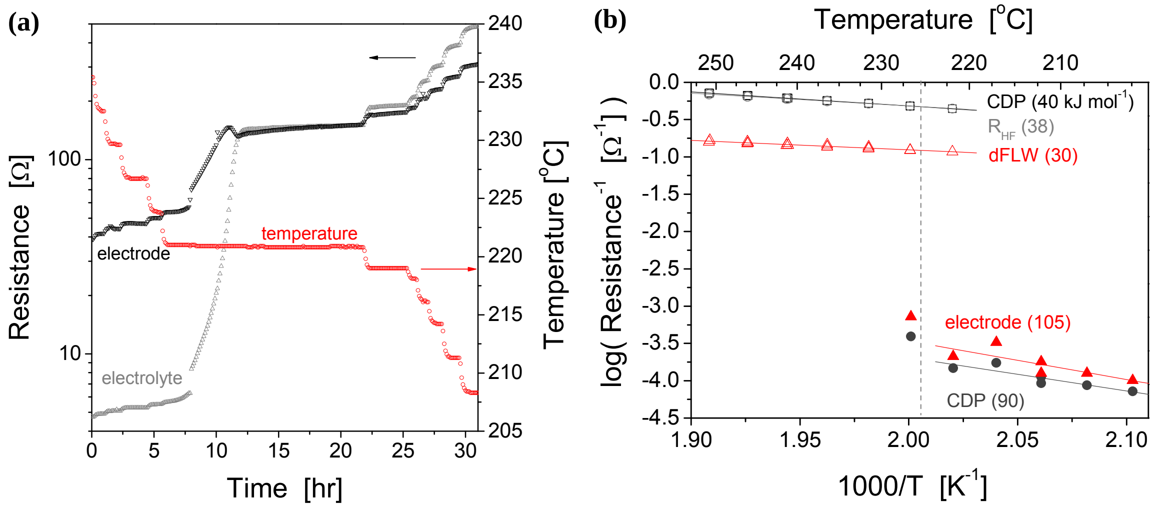

Figure C.25 Plots showing the typical behavior of Pt | CsH_2PO_4 | Pt across the phase transition: (a) the cell temperature and the resistances of the electrolyte and electrodes (100 nm thick, 12.6 mm dia. Pt), plotted as a function of time and (b) an Arrhenius plot of the steady-state values (75 nm thick, 12.6 mm dia. Pt). Inverse resistance, R_E^{-1}, is plotted here, but activation energies shown are computed from a plotting $R_E^{-1} \times T$.

C.7.2 Platinum Film Geometry Dependence

Figure C.26 shows how the electrolyte and electrode resistances vary with Pt film geometry at temperatures below the phase transition temperature. As expected, proton conduction through CsH_2PO_4 exhibits no dependence on the Pt film diameter (Figure C.26a). On the other hand, the electrode process varies notably with film diameter, displaying a slope close to –3 on the double-logarithmic plot. Note that the data for all cells, with Pt film thicknesses of 7.5–375 nm, collapse into one line, indicating that the electrode process exhibits no thickness dependence. This is more explicitly shown in Figure C.26b; in this plot, the electrode resistance is area-normalized for clarity of presentation. The film geometry dependence of the electrode resistance at temperatures below the phase transition temperature of CsH_2PO_4 is consistent with an interfacial rate-limiting step, proposed to occur at $Pt\,|\,CsH_2PO_4$. Based on the extrapolation of the hydrogen diffusion resistance from superprotonic temperatures to a temperature of 200 ºC (Figure C.25b), we expect hydrogen diffusion to be fast, enabling access to the two-phase interface. It is interesting to note that, at $T < T_{SPT,}$ Au-Pt electrodes (shown in Figure C.17) also fall within the range resistance values shown in Figure C.26, suggesting that the presence of Au (in any given configuration) no longer influences the kinetics.

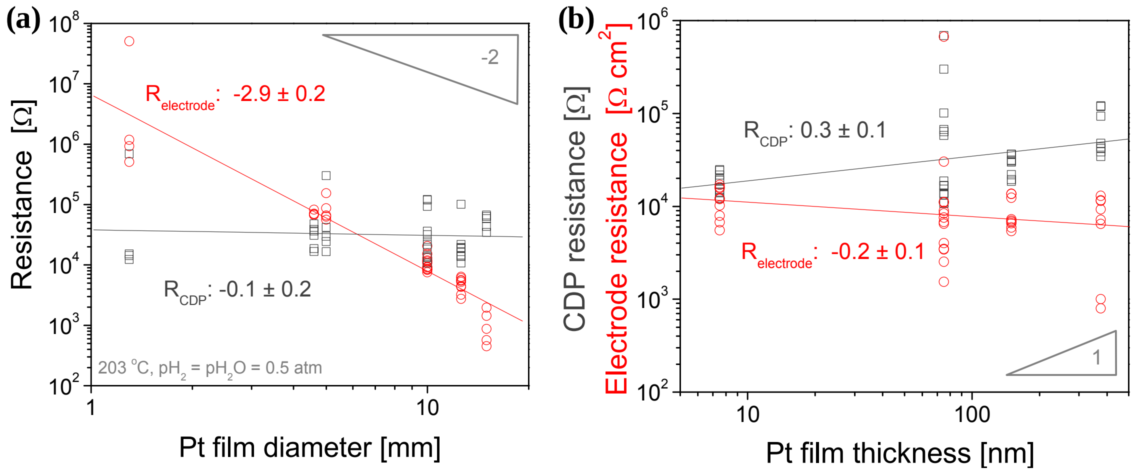

Figure C.26 Geometry dependence of electrode and electrolyte resistances below the phase transition temperature, on a double-logarithmic plot. $T \approx 200$ °C, $pH_2 \approx pH_2O \approx 0.5$ atm. The resistance of CsH_2PO_4 is not dimension-normalized because its dimensions do not vary significantly across samples. The geometry dependence reveals that the electrode resistance decreases with area (a) but is not thickness-dependent (b).

C.7.3 Temperature Cycling and Crack Formation

As reported in Chapter 5, the incompatibility of the monoclinic and cubic phases of CsH_2PO_4 results in the formation of microcracks during phase transformation. In this section, we examine the effect of repeated cycling on the formation and distribution of microcracks in polycrystalline CsH_2PO_4. Figure C.27 shows a series of images of a polycrystalline CsH_2PO_4 surface taken after each of three heat-cool cycles during which mechanical pressure was applied to the cell (in a similar manner as with the Pt | CsH_2PO_4 | Pt cells), while Figure C.28 shows images after each of two heat-cool cycles for a sample to which no external pressure was applied. The CsH_2PO_4 surfaces were scratched so that images could be taken at a fixed location after each thermal cycle. In both cases, the distribution of cracks appeared to change with each cycle; new microcracks formed in the substrate while a few existing cracks healed slightly, with the generation of cracks outnumbering the disappearance. From these images, it appears that cracking healing (as highlighted in the images) occurred more readily when pressure was applied to the sample. In addition, when no pressure is applied to the cell (Figure C.28), the greater number of fine cracks is visible, possibly because of the lack of external force that can aid in healing the cracks. To confirm these speculations, a statistical analysis would be required.

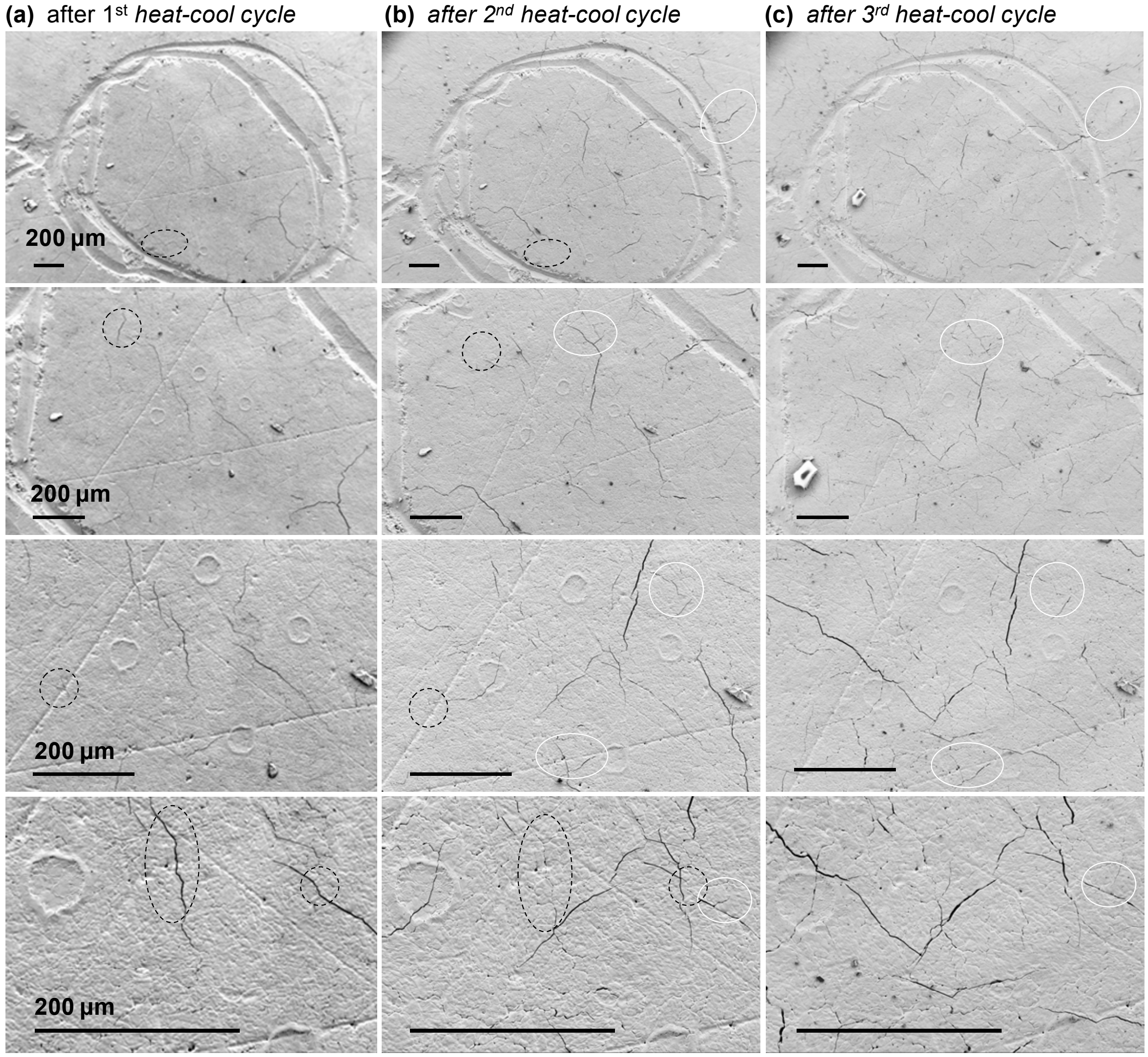

Figure C.27 The effect of the superprotonic phase transition on cracking in densified polycrystalline CsH_2PO_4 disc, with mechanical pressure applied to the disc. SEM micrographs of a CsH_2PO_4 surface, taken at the same location on the surface, after (a) one, (b) two and (c) three heat-cool cycles. Dotted black lines indicate several locations at which cracks had healed between (a) and (b), while solid white lines indicate the healing of cracks between (b) and (c).

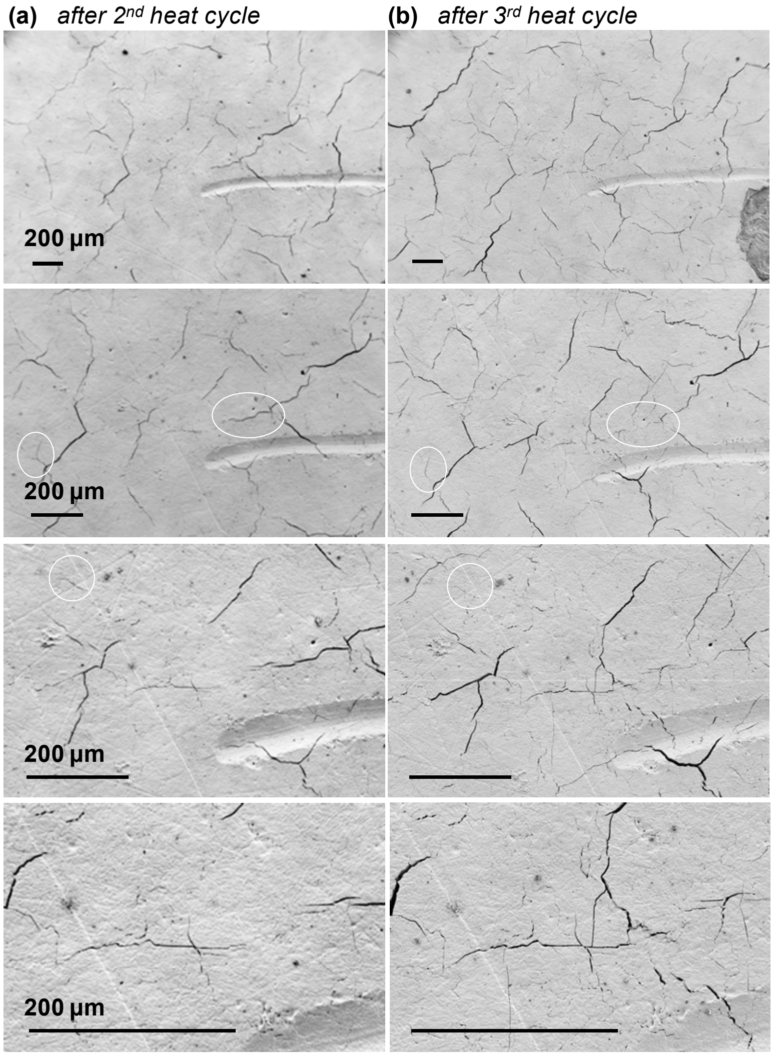

Figure C.28 The effect of the superprotonic phase transition on cracking in polycrystalline CsH_2PO_4 *without* mechanical pressure applied to the substrate. SEM micrographs of a CsH_2PO_4 surface after (a) two heat-cool cycles and (b) three heat-cool cycles taken at the same location on the surface. Solid white lines highlight locations where cracks had healed.

That the density of microcracks increases when CsH_2PO_4 is taken through the transition may have implications for electrode studies. In the case of metal films, new cracks generated after each cycle are propagated to the films while healed cracks do not affect the film structure (since Pt itself cannot heal). Therefore, if the rate-limiting step occurred at triple-phase boundary sites (e.g., at these cracks, Figures 3.3 and 3.9), then cycling would cause a drop in the measured electrode resistance. On the other hand, for an electrode process rate-limited by a two-phase process, the addition of triple-phase sites would have no impact on the shape or size of the impedance arc (provided that the increase in the number of triple-phase sites is not large enough to overtake the two-phase pathway). Based on these expectations, it is not surprising that in the case of the Pt | CsH_2PO_4 | Pt system, the impedance response varies little with cycling through the phase transition (Figure C.29). The impedance spectra collected before and after temperature cycling, shown here for cells with 7.5 and 150 nm thick Pt films, overlap almost perfectly, indicating that neither the interfacial nor diffusion step (which dominate 7.5 and 150 nm films, respectively) is affected when additional cracks in the Pt film are generated. In some cases, there appeared to be a small decrease in the total combined width of the spectra with cycling, as shown in the case of 52.5 nm Pt films (Figure C.30a). Extracted fit values for the resistances for the ohmic, high-frequency and electrode (dFLW) processes reveal that most of this change comes from processes associated with the electrolyte (ohmic + constriction) rather than the electrode (Figure C.30b). That the constriction arc itself seems to be shrinking suggests that the change in the spectra is related to the contact of the carbon paper to the cell; this is not unreasonable because the volume difference between the two phases of CsH_2PO_4 is ~ 2%.

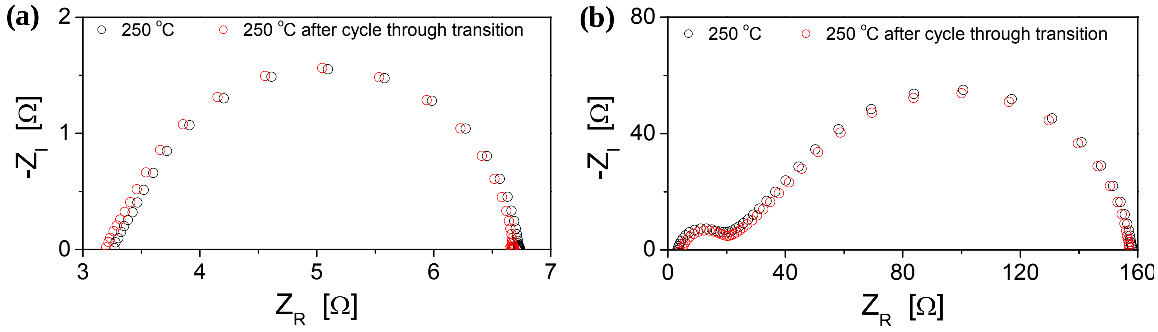

Figure C.29 Impedance spectra for Pt | CsH_2PO_4 | Pt symmetric cells before and after a cool-heat cycle through the phase transition. The two spectra overlap almost perfectly for both (a) 7.5 nm thick, 15 mm dia. and (b) 150 nm thick, 5 mm dia. Pt films.

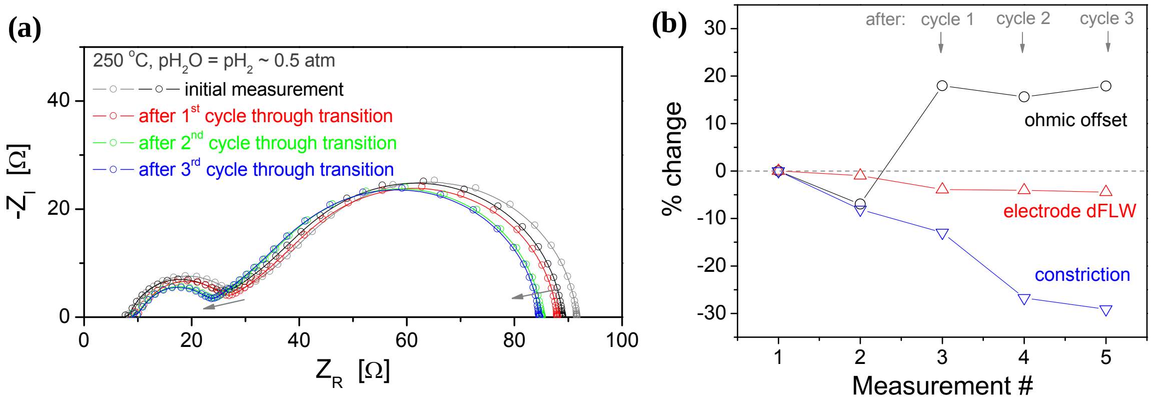

Figure C.30 Effect of thermal cycling on the impedance response of Pt | CsH_2PO_4 | Pt symmetric cells (52.5 nm thick, 5 mm diameter): (a) raw impedance spectra showing how the impedance response behaves after a few cool-heat cycles through the phase transition, (b) a plot of the % change from measurement 1. (Measurement #1 and #2 were both taken before temperature cycling, specifically before and after collecting Arrhenius data at superprotonic temperatures.)

Appendix D Hydrogen Electro-oxidation over Palladium Thin Films

Palladium is known to have high hydrogen solubility and is therefore widely studied as a hydrogen permeation membrane.[31] Thus, Pd is expected to facilitate hydrogen oxidation (and oxygen reduction) via the two-phase boundary pathway. Not only this, Pd belongs to the same group as Pt on the periodic table and therefore has great potential as a high-activity fuel cell electrocatalyst with lower cost.[125] In this section, we present our investigation of hydrogen oxidation over Pd thin films deposited atop CsH_2PO_4. Using thin film techniques, we can make a more meaningful comparison between the Pd and Pt as hydrogen oxidation electrocatalysts for solid acid fuel cells.

D.1 Experimental

The preparation of Pd | CsH_2PO_4 | Pd symmetric cells was identical to that for Pt based cells presented in Chapter 3. Pd films 10–300 nm in thickness were fabricated.

The general crystallinity of the Pd films, adhered to the substrates, was evaluated using a Phillips X'Pert Pro powder X-ray diffractometer using Cu Kα radiation (45 kV, 40 mA) with a 2θ range of 15–90º. The morphology of the metal films both before and after electrochemical characterization was examined by scanning electron microscopy, SEM, (LEO 1550VP, Carl Ziess SMT) using a 3 kV accelerating voltage. Chemical analysis for a subset of the films was carried out using an Oxford INCA 300 X-ray energy dispersive spectrometer (EDS) (in conjunction with the above SEM) at an accelerating voltage of 10 kV. The film thickness was measured by cross-sectional SEM imaging of fractured cells, and the deposition rate of Pt was determined to be 15 nm min^{-1}. The film connectivity was assessed by measuring the sheet resistance of the films, using a hand-held multimeter, both before and after electrochemical characterization.

Impedance spectra were collected, in the majority of cases, using a Solartron Analytical 1260 frequency response analyzer with a 10 mV perturbation voltage about zero bias over frequencies of 10 or 1 MHz to 100 mHz configured with a four-probe measurement geometry. For experimental convenience, some spectra were collected using a Solartron 1250 analyzer equipped with a potentiostat (Princeton Applied Research, EG&G 273A). Electrical connection to the cells was made using an in-house constructed sample holder in which the cells were sandwiched between two pieces of Toray carbon fiber paper (280 µm thick) placed between two stainless steel porous discs. Using the sample holder, adequate pressure was applied to the assembly to mechanically contact silver wire leads to the stainless steel discs. For a subset of the thicker films, electrical connection was made by the direct attachment of silver wires using colloidal silver paint (Ted Pella, #16032); such a method did not yield electrode responses different from that with Toray paper.

Impedance measurements were collected under the same environmental conditions as was used in the case of Pt-based cells. Because PdO has been observed to react with CsH_2PO_4 in oxidizing conditions at ~ 240 ºC (Appendix B), we verified that the formation of PdO, $Pd(OH)_2$ and $Pd(OH)_4$ (for which thermodynamic data was available) is unfavorable for all H_2-H_2O atmospheres and temperatures examined in this study. Based on these calculations, we expect Pd films to be stable throughout the symmetric cell experiments.

Cells were typically heated to ~ 50–100 ºC in ambient air before flowing Ar with ~ 0.03 atm H_2O. After this, the temperature was raised to 150 ºC at ~ 3 ºC min^{-1} and held at this temperature for 0.5–1 h until the water bubbler could be heated to supply adequate water partial pressures in the inlet Ar stream. Once an adequate pH_2O level is attained, the cells were heated to 250 ºC at 2.5 ºC min^{-1} under H_2 flow.

D.2 Results and Discussion

D.2.1 Palladium Film Characteristics

Figure D.1 shows X-ray diffraction patterns of as-deposited 100 nm Pd films before and after electrochemical characterization; these patterns were considered representative of Pd films 100–300 nm thick. The breadth of the Pd peak at $2\theta \approx 40^o$ indicated that the deposited Pd was crystalline with small grains (was was the case for Pt films). In these particularly patterns, the main peak sharpened after electrochemical characterization (though not observed consistently between samples) and a small peak at $2\theta \approx 17.5^o$ appeared after electrochemical characterization. The peak at $2\theta \approx 17.5^o$ was not observed in other samples and does not match any peaks for Toray paper (used as a current collector) or for reaction product formed between PdO and CsH_2PO_4 at 240 ºC in air (via reactivity tests described in Appendix B). Aside from this peak, all other films 100–300 nm thick behaved similarly. As-deposited 10 nm Pd films generate peaks too broad and low in intensity to be useful for comparing the film crystallinity before and after electrochemical characterization.

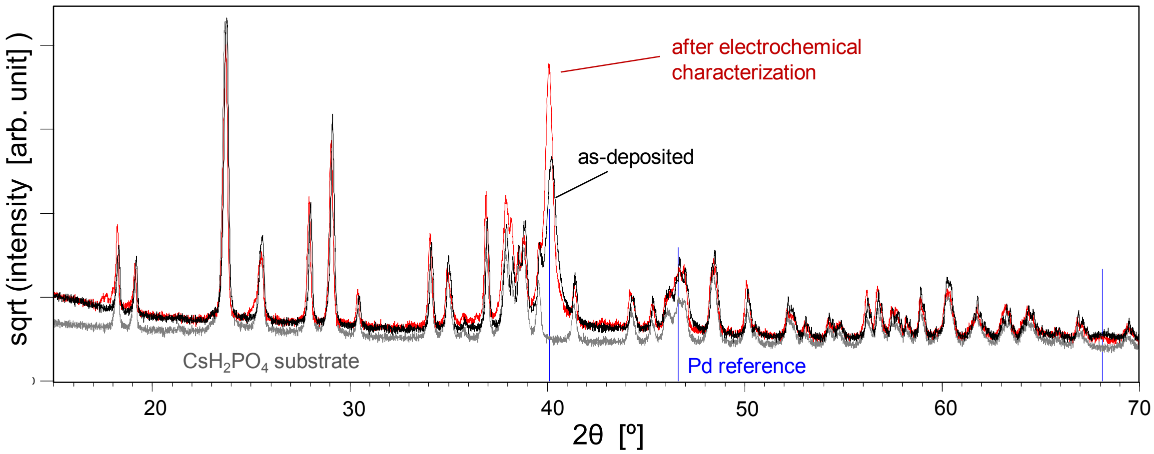

Figure D.1 X-ray diffraction pattern of 100 nm Pd films on top of CsH_2PO_4 before and after electrochemical characterization, shown alongside a CsH_2PO_4 pattern and Pd reference peaks.

Films 100, 200, and 300 nm thick (Figure D.2) appear to be intact and laterally connected. The cross-sections of the film, particularly in Figure D.2c, show film structures similar to those for Pt (Chapter 3). 10 nm Pd films were too thin to be visualized by SEM, so the thickness of 10 nm is estimated from the deposition time.

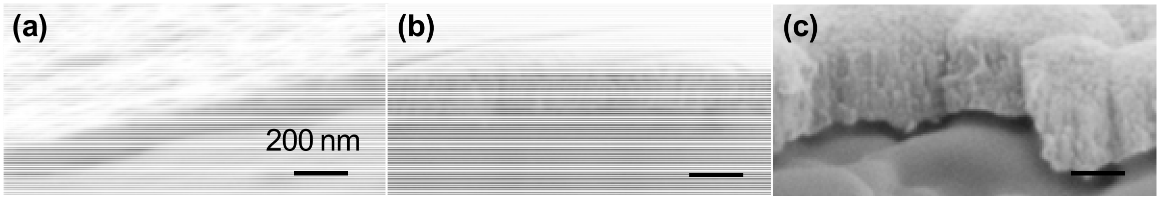

Figure D.2 SEM images of the cross-sections of Pd | CsH_2PO_4 | Pd cells showing as-deposited films Pd films (a) 100 nm, (b) 200 nm, and (c) 300 nm thick.

The characteristics of 10 nm Pd films were different from those of thin Pt films (e.g., 7.5 nm). As-deposited Pd films showed finite values of sheet resistance, comparable to those measured for 7.5 nm Pt films. However, after electrochemical characterization, the sheet resistance was not measurable by a hand-held voltmeter, indicating a virtually non-existent electronic connectivity of the Pd films. This is consistent with SEM observations of the 10 nm Pd films before and after electrochemical characterization (Figure D.3). As-deposited films appeared conformal on the CsH_2PO_4 surface, revealing underlying grains ~ 300 nm to ~ 1 μm in size. After electrochemical tests at superprotonic conditions, however, the films aggregated into small Pd islands 100–200 nm in size.

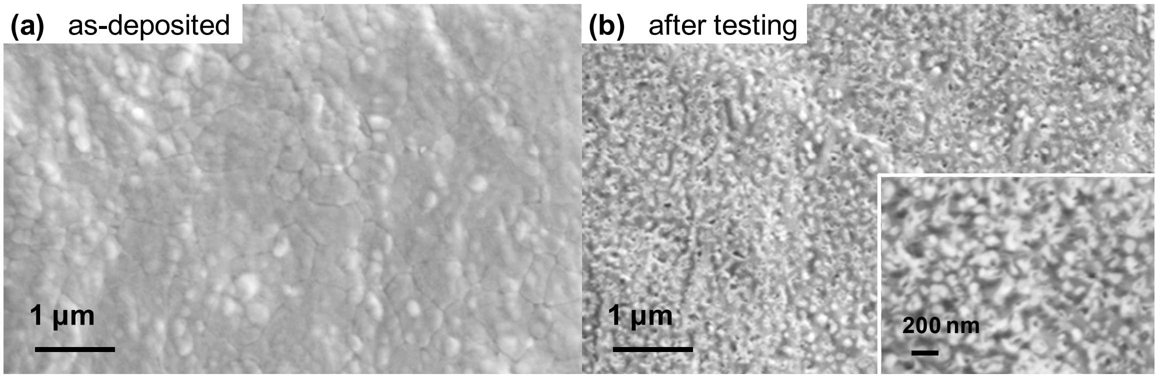

Figure D.3 In-plane SEM micrographs of 10 nm Pd films deposited on top of CsH_2PO_4, comparing films (a) before and (b) after electrochemical characterization at ~ 250 ºC in humidified H_2-Ar atmospheres.

In-plane images of the films (Figure D.4 and Figure D.5, 100 nm films) show somewhat irreproducible results in terms of film stability. For most of the thicker films examined, the films remained intact after electrochemical characterization (Figure D.4). Some buckling of the films after testing was observed; this is in contrast to Pt films, for which only thick 375 nm films showed any noticeable buckling. For a subset of the films, the film quality degraded after electrochemical characterization (Figure D.5). The films were penetrated by what appears to be the underlying CsH_2PO_4. At two different locations across the boundary of the Pd film, Figure D.5b and Figure D.5c, respectively, the films segregated into small islands, with notably different microstructures across the boundary. (A fully masked region of the substrate onto which no Pd was deposited is shown in Figure D.5d for reference). By energy dispersive spectroscopy analysis of regions 1 and 2 (as marked in Figure D.5a), it was determined that region 1 has a lower Pd:Cs atomic ratio but a higher O:Cs ratio; the P:Cs ratios were comparable. That is, region 1 is comprised of a greater amount of oxygen but less of Pd. The P:Cs ratio for both regions were between 1.5 and 2, rather than the expected value of 1 for CsH_2PO_4. Based on the sampling volume of EDS and the XRD results for CsH_2PO_4 (Figure D.1), this observation implies a P-rich region near the surface of the CsH_2PO_4 disc.

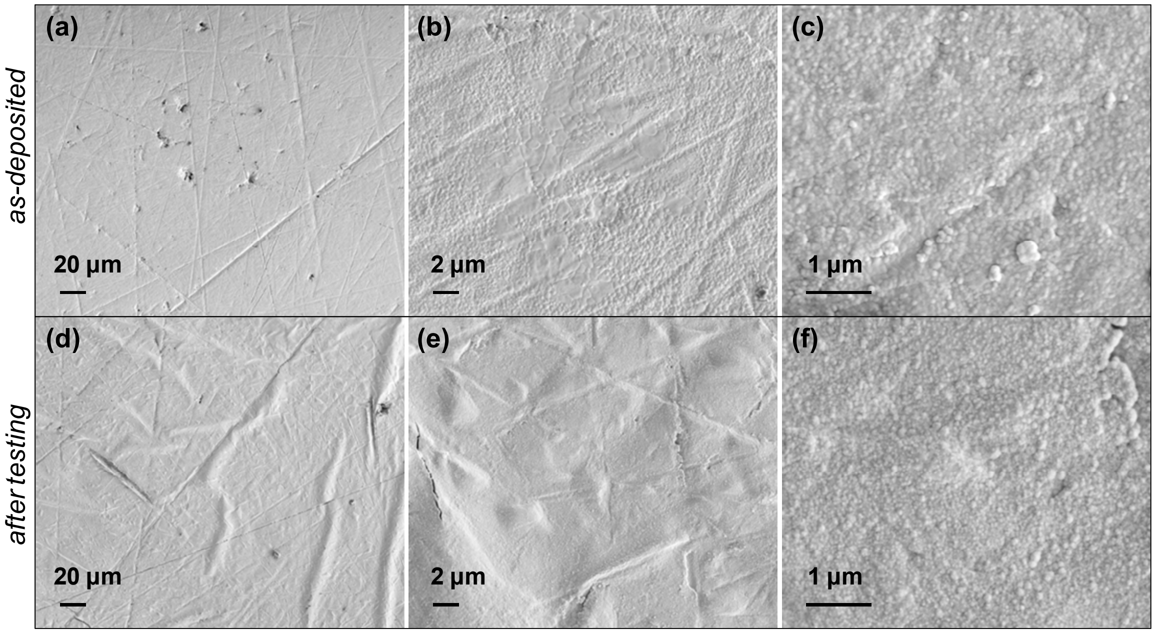

Figure D.4 In-plane SEM micrographs of 100 nm Pd films deposited on top of CsH_2PO_4, comparing the films (a–c) before and (d–f) after electrochemical characterization at ~ 250 ºC in humidified H_2-Ar atmospheres.

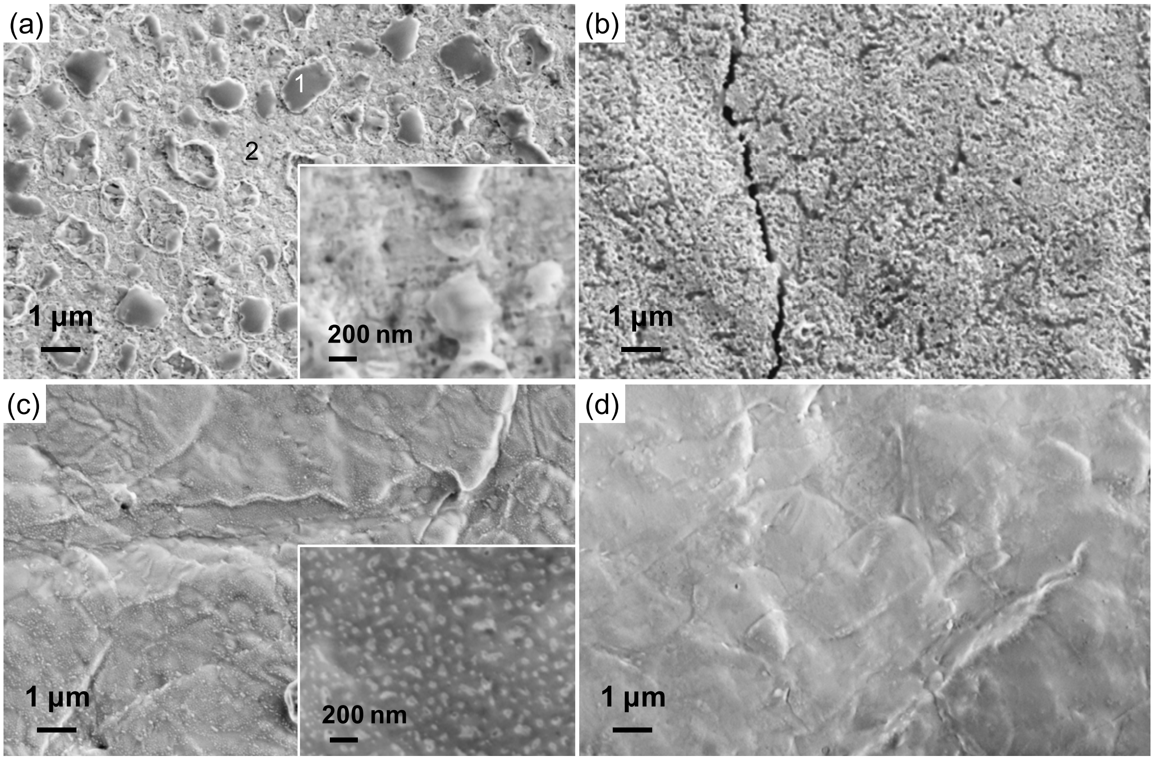

Figure D.5 In-plane SEM micrographs of 100 nm Pd films deposited on top of CsH_2PO_4 (a) near center of film/disc, (b) Pd-rich region and (c) CsH_2PO_4-rich region at the Pd-CsH_2PO_4 boundary, and (d) masked CsH_2PO_4 surface with no Pd present, for reference. Images were taken after electrochemical characterization at ~ 250 ºC in humidified H_2-Ar atmospheres.

The source of the differences between the two sets of films shown in Figure D.4 and Figure D.5 requires further exploration. One possible explanation is that variations in the length of time as-fabricated symmetric cells reside at ambient conditions before characterization or in the procedure for ramping the cell temperature to superprotonic conditions can lead to the (temporary) formation of Pd oxide. Such variations in the temperature and gas environment history may affect reproducibility in the Pd | CsH_2PO_4 | Pd system.

D.2.2 Characteristics of Impedance Spectra

Figure D.6 shows an impedance spectrum for a Pd | CsH_2PO_4 | Pd symmetric cell with 100 nm Pd, 10 mm in diameter. The spectrum was shifted by its ohmic offset for ease of analysis and corrected for inductance effects. Four features are visible in the spectrum. An arc at frequencies above 133 kHz (originally masked by system inductance, as indicated in the figure) is attributed to constriction (Appendix C.3). As the frequency is decreased, three additional arcs follow, denoted as “HF”, “MF”, and “LF”, with the intermediate MF arc at ~ 620 Hz being convoluted with the HF and LF arcs. The raw data (including ohmic offset) were fitted to an empirical equivalent circuit (Figure D.7) and used to extract the resistance (width) of each arc. Each parallel RQ sub-circuit corresponds to each of the four arcs; an inductor was included to account for system inductance and a resistor for proton transport through CsH_2PO_4. (In Figure D.6, the extracted values for the ohmic offset and inductance were used in order to perform the offset and inductance corrections.)

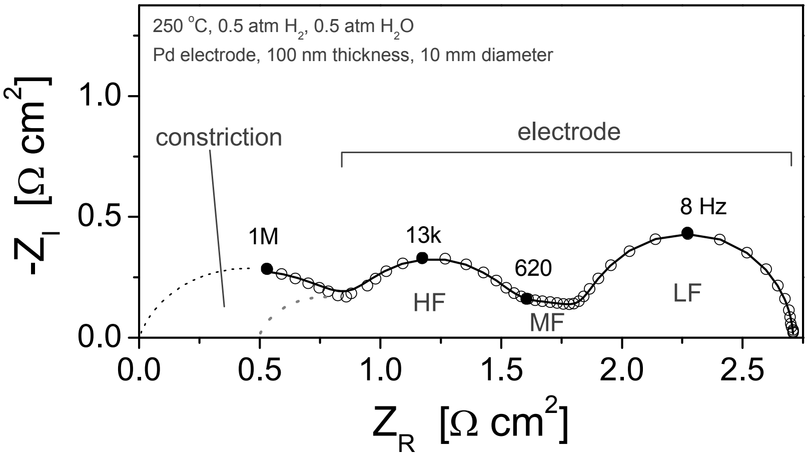

Figure D.6 Impedance spectrum for a Pd | CsH_2PO_4 | Pd symmetric cell with 100 nm Pd films 10 mm in diameter, collected at ~ 250 ºC in H_2-H_2O with ~ 0.5 atm H_2O. The solid line is a fit to the equivalent circuit shown in Figure D.7. The thick dotted line at high frequency denotes raw data (before inductance correction) and thin dotted line serves as a guide to the eyes.

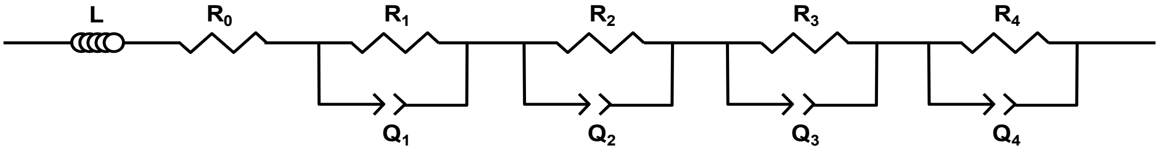

Figure D.7 Equivalent circuit model for the Pd | CsH_2PO_4 | Pd symmetric cell. L = inductance, R_0 = electrolyte resistance, R_i = resistance of process *i*, and C_i = capacitance of process *i*.

Although the impedance spectrum in Figure D.6 shows three electrode arcs, data acquired from over 30 cells with film thicknesses of 100–300 nm and diameters of 1–15 mm revealed variations in the shape of the spectra. The appearance of the MF arc was irreproducible, neither dependent on film thickness nor diameter. Figure D.8 shows three impedance spectra for Pd films of three different thicknesses. Based on their characteristic frequencies, it is evident that the HF and LF arcs are present, but the MF arc is masked, surfacing as a small separation between the HF and LF arcs (Figure D.8b). This separation is most noticeable for the 100 nm film and occurred to varying degrees depending on the sample. Although the shape of the spectra varies across samples, the total electrode resistance is fairly reproducible and exhibits no dependence on film thickness (Figure D.6 and Figure D.8a).

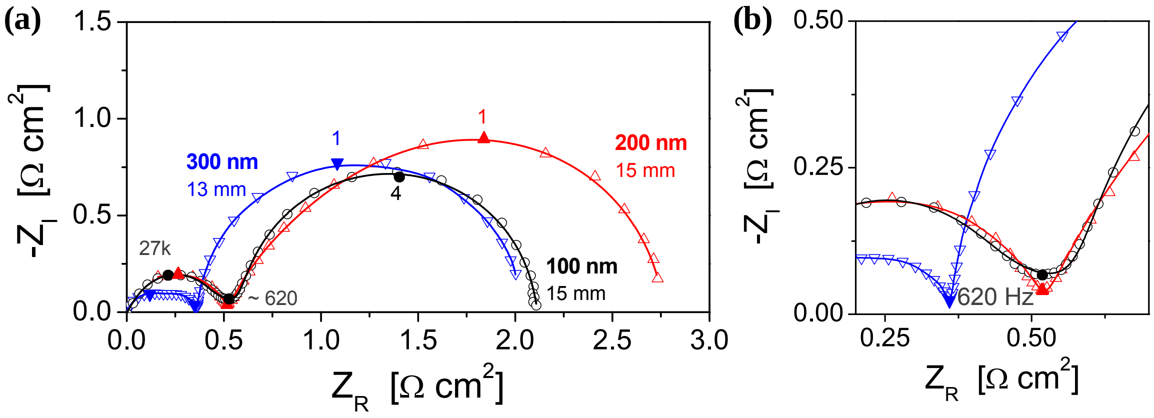

Figure D.8 Select impedance spectra collected at ~ 250 ºC in H_2-H_2O with ~ 0.5 atm H_2O for 100, 200, and 300 nm thick Pd films showing (a) the HF and LF arcs and (b) a partially hidden MF arc.

D.2.3 Effect of Palladium Film Geometry

Despite the apparent variability of the impedance response, we fit the spectra to an equivalent circuit similar to that shown Figure D.7 but with one less parallel RQ sub-circuit depending on whether or not the MF arc is visible. Based on the fit results, we assigned the constriction, HF, MF and LF arcs based on their characteristic frequencies and plotted their corresponding resistances as functions of film diameter (Figure D.9) and thickness (Figure D.10). From Figure D.9, it is immediately clear that the resistance of each electrode process scales with the film area. Based on this result, we plot the area-normalized resistance as a function of thickness (Figure D.10) and show that the electrode processes do not depend on thickness, consistent with the impedance spectra shown in Figure D.8a.

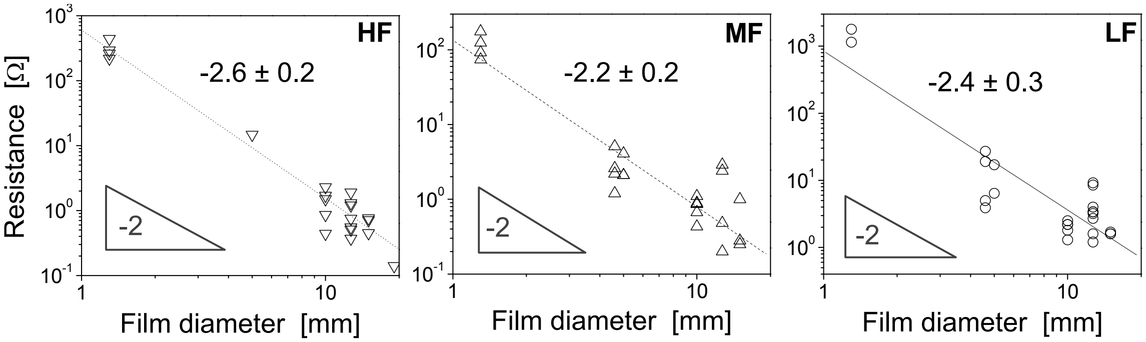

Figure D.9 Plots of electrode resistance (~ 250 ºC in H_2-H_2O with ~ 0.5 atm H_2O) as a function of film diameter. HF, MF and LF denote high-, mid-, and low-frequency arcs, respectively.

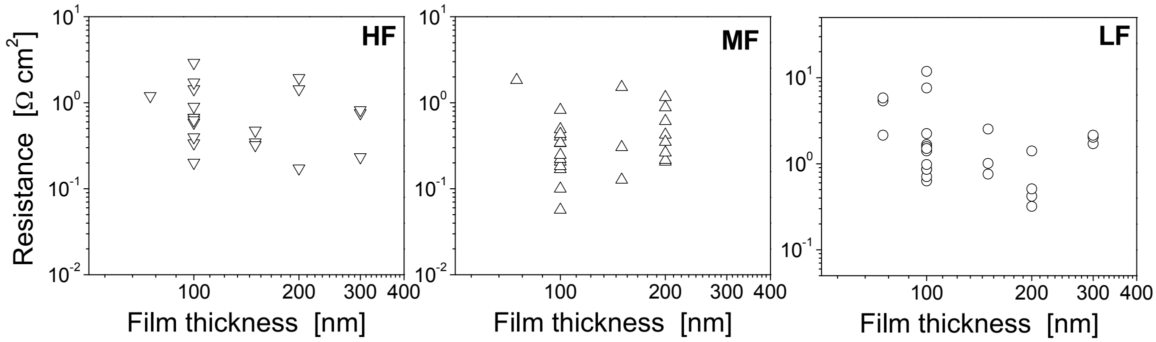

Figure D.10 Plots of area-normalized electrode resistance (~ 250 ºC in H_2-H_2O with ~ 0.5 atm H_2O) as a function of film thickness. HF, MF and LF denote high-, mid-, and low-frequency arcs, respectively. Slopes range between –0.6 to 0.3 with large errors.

D.2.4 Effect of Environmental Parameters

The effect of temperature, hydrogen partial pressure (pH_2) and water partial pressure (pH_2O) on the electrode processes were examined. Plots of the electrode resistance as a function of pH_2 and temperature for the cell presented in Figure D.6 are presented in Figure D.11a and Figure D.11b, respectively. The pH_2 reaction order and activation energy for each process is noted in the plot. Using similar plots for over 30 symmetric cells, the average reaction orders for pH_2 and pH_2O (plot not shown) and the activation energies were extracted and are tabulated in Table D.1, along with the corresponding values of the area-normalized electrode resistance (in units of Ω cm^2).

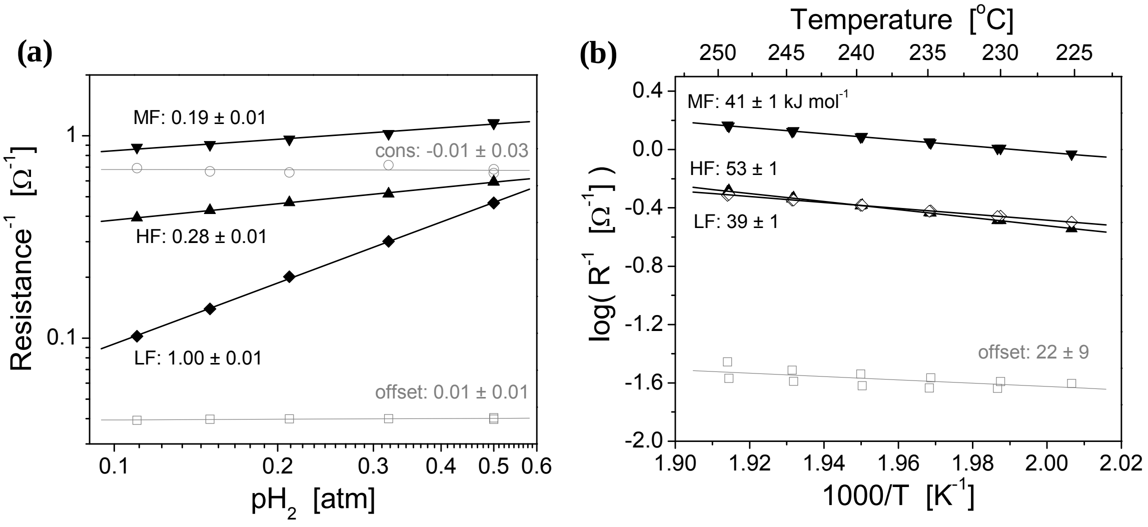

Figure D.11 Representative plots used for extracting (a) pH_2 reaction order and (b) activation energy. Shown are data for a Pd | CsH_2PO_4 | Pd cell with 100 nm Pd, 10 mm dia.

Table D.1 Pd | CsH_2PO_4 | Pd symmetric cell: average values of the area-normalized resistance, pH_2 and pH_2O reaction orders and the temperature dependence (of $R_E^{-1} \times T$ for the offset and constriction arcs and R^{-1} for HF, MF and LF arcs). $\tilde{R}$ = area-normalized resistance

arc	$\tilde{R}$ **[Ω cm^2]**	**pH_2 rxn order** (250 ºC)	**pH_2O rxn order** (250 ºC)	**T [kJ mol^{-1}]** ($pH_2 \approx pH_2O \approx 0.5$ atm)
offset	—	0.02 ± 0.04	–0.02 ± 0.02	37 ± 9
constriction	—	0.01 ± 0.07	0.01 ± 0.05	38 ± 3
HF	0.6 ± 0.3	0.2 ± 0.2	0.05 ± 0.05	38 ± 21
MF	0.4 ± 0.3	0.4 ± 0.2	–0.03 ± 0.05	36 ± 9
LF	1.4 ± 0.6	1.0 ± 0.2	–0.12 ± 0.07	31 ± 6

The electrode resistances of all three processes displayed negligible dependence on pH_2O. This is in contrast to the Pt thin film electrode response which exhibited a reaction order of ~ 0.3 for all film thicknesses. The pH_2 dependence varies significantly between the arcs, with the HF arc displaying almost zero dependence while the MF and

LF arcs have stronger dependences of 0.4 ± 0.2 and 1.0 ± 0.2, respectively. The high errors associated with the HF and MF arcs are a consequence of their smaller resistances such that convolution with one another and with the constriction arc induced larger errors during equivalent circuit fitting. The LF arc is notably more resistive than the remaining arcs and, thus, fitting errors associated with this process were smaller. The reaction order of 1 for the low-frequency arc is highly suggestive of a surface exchange step at the Pd | H_2 interface, similar to that observed for the 7.5 nm Pt film electrode. (The $p\mathrm{H}_2$ reaction order for the 7.5 nm Pt film was found to be 0.74 ± 0.08 and includes residual contribution from hydrogen diffusion.) The activation energy of the LF process, 31 ± 6 kJ mol^{-1} process is also comparable to that for the 7.5 nm Pt film, 28 ± 3 kJ mol^{-1}.

Based on the $p\mathrm{H}_2$ reaction order of 0.4 (close to ½) and the activation energy of 36 ± 9 kJ mol^{-1}, it would be reasonable to hypothesize that the MF arc corresponds to hydrogen diffusion through Pd, with the lower activation energy relative to that for diffusion in Pt being attributed to a smaller influence from hydrogen trapping. However, a quick calculation of the expected resistance, based on known values of hydrogen diffusivity and solubility in Pd, yields a value that is three orders of magnitude smaller than the values obtained here. Specifically, for a temperature of 250 ºC and hydrogen partial pressure of 0.5 atm, the solubility of hydrogen in Pd is ~ 0.01 H/Pd[31] and the hydrogen diffusivity is ~ 3×10^{-9} $\mathrm{m}^2\,\mathrm{s}^{-1}$.[126] Using Equation (A.42), the area-normalized resistance is computed to be 4×10^{-4} $\Omega\,\mathrm{cm}^2$ for 300 nm Pd film (thickest film used in this study). The average experimentally determined value for the MF arc, 0.4 $\Omega\,\mathrm{cm}^2$, is significantly larger than the computed value; any deviations in the computed value due to trapping effects would be unlikely to account for this difference.

D.2.5 Impedance Response of Layered Pt-Au Film Electrodes

Preliminary measurements of Pd-Au bilayers deposited on top of CsH_2PO_4 are presented in Figure D.12. (Note that the films in this figure are 5 mm in diameter, so the HF arc is convoluted with the constriction arc.) Surprisingly, the effect having Au either on top of Pd (Au | Pd | CsH_2PO_4) or between Pd and CsH_2PO_4 (Pd | Au | CsH_2PO_4) is minimal. In the case of Pd | Au | CsH_2PO_4, the high-frequency process appears to be less convoluted with the constriction arc, indicating that the HF arc corresponds to a process the metal | CsH_2PO_4 interface. However, the LF arc increases relative to the control (Pd | CsH_2PO_4), an unexpected result. In the case of Au | Pd | CsH_2PO_4, the impedance response displays no significant changes from the control. Overall, based on Figure D.12, we can conclude that the effect of Au on the impedance response of the Pd system is within the margin of scatter.

It should be noted that the Pd | CsH_2PO_4 spectrum plotted in Figure D.12 is consistent in shape and total width to those shown in Figure D.6 and Figure D.8. However, the film quality for these cells after electrochemical characterization (Figure D.5), is significantly degraded in comparison. That the impedance spectra are not dramatically different despite their varied film characteristics (Figure D.4 vs. Figure D.5) implies that the electrode response is not especially sensitive to film morphology.

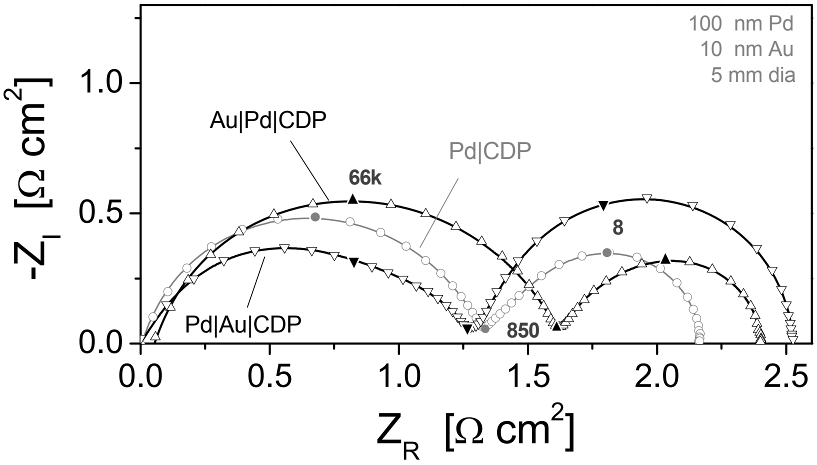

Figure D.12 Impedance spectra, collected at 250 ºC in H_2-H_2O with ~ 0.5 atm H_2O, for Pd | CsH_2PO_4, Au | Pd | CsH_2PO_4 and Pd | Au | CsH_2PO_4 for which Pd and Au films were 100 nm and 10 nm, respectively.

D.2.6 10 nm Palladium Films

As shown in Figure D.3, 10 nm Pd films degraded significantly after testing. This is consistent with their impedance spectra (Figure D.13) The large values for the area-normalized resistance, > 15 kΩ cm^2, reflect the lack of electronic connectivity in the films. Two arcs are visible, although the total resistance is dominated by the low-frequency arc. The observation that the two arcs are dramatically different in size, compared to the arcs in the impedance spectra of thicker intact films, is interesting since a lack of connectivity if the Pd film should result in the two arcs increasing by the same factor. This implies a difference in the reaction mechanism between thick, intact films and thin degraded films.

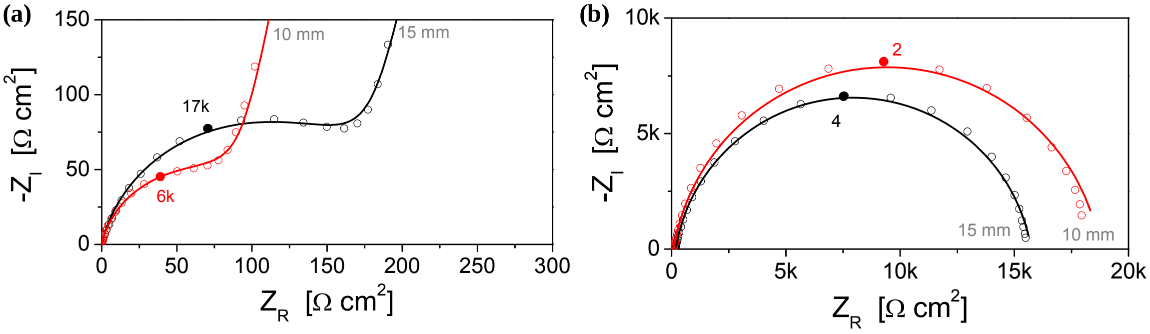

Figure D.13 Impedance spectra for Pd | CsH_2PO_4 | Pd cell (10 nm Pd films) collected at 250 °C in H_2-H_2O with ~ 0.5 atm H_2O: (a) high-frequency arc and (b) low-frequency arc.

D.2.7 Comparison to Platinum

The total Pd electrode resistance, averaged across ~ 30 symmetric cells, was found to be $2.2 \pm 0.8\ \Omega\ cm^2$. Because the rate-limiting steps for hydrogen electro-oxidation over Pd do not depend on thickness and therefore are dominated by interfacial processes, it is expected that a direct comparison of the Pd film results to those for ultra-thin Pt films (for which interfacial effects dominate) would provide an adequate comparison of their relative interfacial activities. From Chapter 3, we found that for a 7.5 nm Pt film, the resistance was ~ $3.1 \pm 0.5\ \Omega\ cm^2$, whereas the estimated interfacial resistance was (coincidentally) $2.2\ \Omega\ cm^2$, both of which are, to within experimental scatter, comparable to the Pd electrode resistance. This implies that the *interfacial* activity of Pd is comparable to, if not better than, that for Pt.

Although the activity of the Pd film electrode indicates that Pd may surpass Pt in the anode of solid acid fuel cells, the degradation of thin Pd films precludes fabrication of comparably thin films for application purposes. One solution to this problem is to fabricate layered Pt-Pd electrodes. The electrode resistance of each of the three Pd arcs

(Table D.1) has, on average, a value that is smaller than the total electrode resistance of 7.5 nm Pt. Therefore, determining the identity of these rate-limiting processes (and that for thin Pt films) can be extremely valuable for designing an optimal Pd-Pt bilayer catalyst. For example, *if* the interfacial process in Pt and the LF arc in Pd both correspond to surface exchange at the metal | gas interface, and the HF arc in Pd corresponds to charge transfer, then the Pd | Pt | CsH_2PO_4 configuration may minimize the total electrode resistance. This is because Pt | CsH_2PO_4 exhibits no charge transfer resistance in its impedance response and gas | Pd | CsH_2PO_4 exhibits a lower surface exchange resistance than gas | Pt | CsH_2PO_4. One can entertain additional film configurations, depending on the identity of the Pd arcs.

D.3 Summary

1) Pd films 100–300 nm thick were found to have a total electrode resistance of $2.2 \pm 0.8\ \Omega\ \mathrm{cm}^2$. Three electrode processes were observed, all of which scaled with film area but not film thickness.
2) 10 nm Pd films degraded significantly after electrochemical testing.
3) Preliminary measurements of Pt-Au bilayer films revealed a negligible effect of Au on the rate-limiting steps.
4) Reproducibility appeared to be problematic for Pd films (compared to Pt films). It is possible that as-deposited films have a surface oxide, or a surface oxide may form during initial heating of the sample. Reaction between the resulting Pd oxide layer and CsH_2PO_4 may be the source of variability in the impedance response.

5) Despite possible oxide formation, the electrode activity of Pd is still comparable to that for Pt. Therefore, Pd remains a promising anode for solid acid fuel cells.

D.4 Recommendations for Future Studies

1) It is likely that more reproducible results could be attained by proper handling of the films. After loading the symmetric cell, the reactor should be flushed with Ar at room temperature before heating up the sample in H_2. It is possible that as-deposited Pd is already partially oxidized, but based on the fact that no reaction was observed between nanoparticle Pd and CsH_2PO_4 at 150 ºC in air after 48 h, it should be possible to attain stable films for characterization despite some exposure to air. Thus, oxidation of Pd (if any) is more likely due to the temperatures and gas environments experienced by the samples during ramp-up.
2) The electrochemical response of the Pd-Au bilayer systems was surprising and should be reproduced. The results would be useful for identifying the rate-limiting steps associated with the Pd electrode arcs.
3) Pt-Pd bilayer films would be valuable for investigating not only the rate-limiting steps for the Pd film electrode but also for designing a high-activity electrode.

Appendix E Nickel Thin Films

In this section, we discuss attempts to study hydrogen electro-oxidation over sputtered Ni films, fabricated using deposition conditions similar to those used for Pt and Pd. However, films appeared to be unstable after electrochemical characterization. As-deposited Ni films appeared intact, but after electrochemical characterization at 250 ºC, 150 and 400 nm thick Ni films aggregated into islands (Figure E.1). In the case of 400 nm films (Figure E.1b), the morphology of what appears to the substrate surface also changed, appearing smoother with poorly defined grain boundaries. Using energy dispersive spectroscopy, we found no significant composition difference between the islands and the smooth matrix, that is, Ni, P, and O were present in both regions, implying that Ni, though not clearly visible, is also present in regions which have morphologies similar to CsH_2PO_4.

Interestingly, films which were not electrochemically characterized but heat-treated at similar conditions remained intact (Figure E.2). 100 nm films heat-treated at superprotonic conditions, with and without electrochemical testing, yielded completely different results. Films which were only heat-treated, Figure E.2(a,d), displayed characteristics similar to those observed for Pt films after testing. However, films which were electrochemically characterized with a 10 mV perturbation (about 0 V) showed severe degradation. It was not possible to distinguish between film and substrate (Figure E.2b); the surface was comprised of uniformly round grains, significantly larger than those in the starting material (Figure E.2c). This is consistent with the observation that the films disappeared completely (Figure E.2d) leaving behind a yellowish tint on the CsH_2PO_4 substrate. The substrate itself also appeared to have degraded and was embedded with fibers from carbon paper.

The physical characteristics of the substrate after electrochemical characterization are consistent with dehydration of CsH_2PO_4, but several repeated and well-controlled experiments (with adequate humidity levels) confirm that Ni | CsH_2PO_4 | Ni cells indeed degrade, usually with the film disappearing and the substrate deforming slightly. These observations are highly suggestive of a reaction between CsH_2PO_4 and Ni. It is worthwhile to note that reaction between NiO and CsH_2PO_4 was not observed in even after 48 h in air at superprotonic conditions (Appendix B).

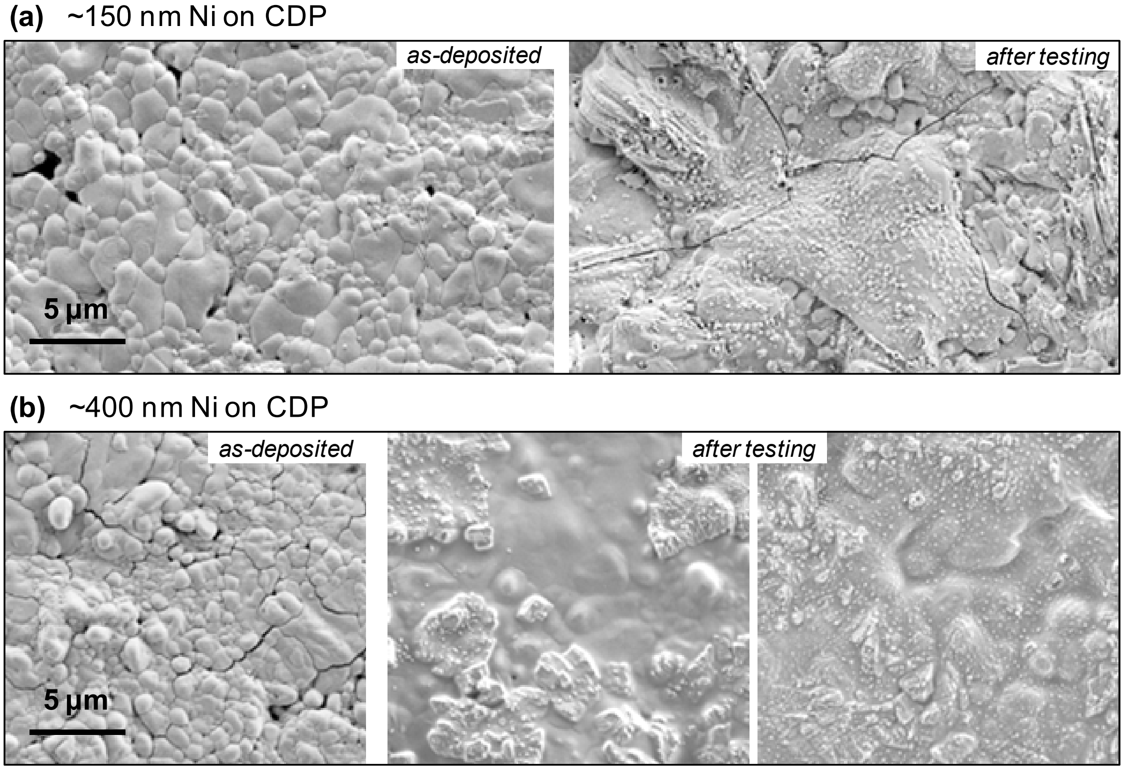

Figure E.1 SEM micrographs of Ni films deposited on top of CsH_2PO_4, as-deposited and after electrochemical characterization at 235 ºC in humidified H_2 gas with ~ 0.4 atm H_2O: (a) 150 nm Ni films (b) 400 nm Ni films.

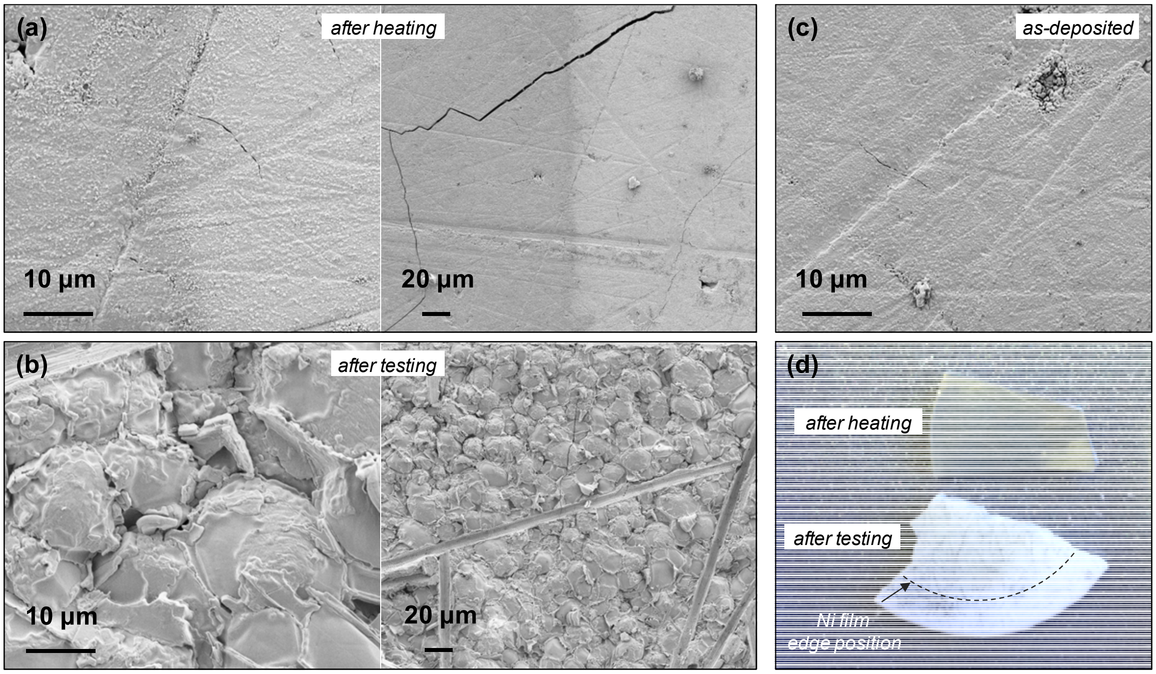

Figure E.2 100 nm Ni films after (a) heat treatment and (b) electrochemical characterization at 250 ºC in humidified H_2 gas with ~ 0.5 atm H_2O compared to (c) as-deposited films. Shown in (d) are photographs of the two samples; the dotted line marks the original Ni-CsH_2PO_4 boundary.

X-ray diffraction patterns corresponding to the samples in Figure E.2(b–c) are shown in Figure E.3. Patterns collected for as-deposited Ni films and after electrochemical characterization contain peaks for CsH_2PO_4. However, the Ni peak, initially small for as-deposited films, disappears completely after electrochemical characterization, implying that either Ni is no longer crystalline or it has reacted with or dissolved into CsH_2PO_4. No peaks for NiO were observed before or after electrochemical characterization.

It is worthy to note that as-deposited Ni films obtained by thermal evaporation yielded Ni diffraction peaks with higher relative intensity compared to films obtained by sputter deposition, as shown in Figure E.4 for 400 nm Ni films obtained by both deposition methods. Thermally evaporated films were stable after heat treatment (not shown), but electrochemical characterization has not yet been carried out.

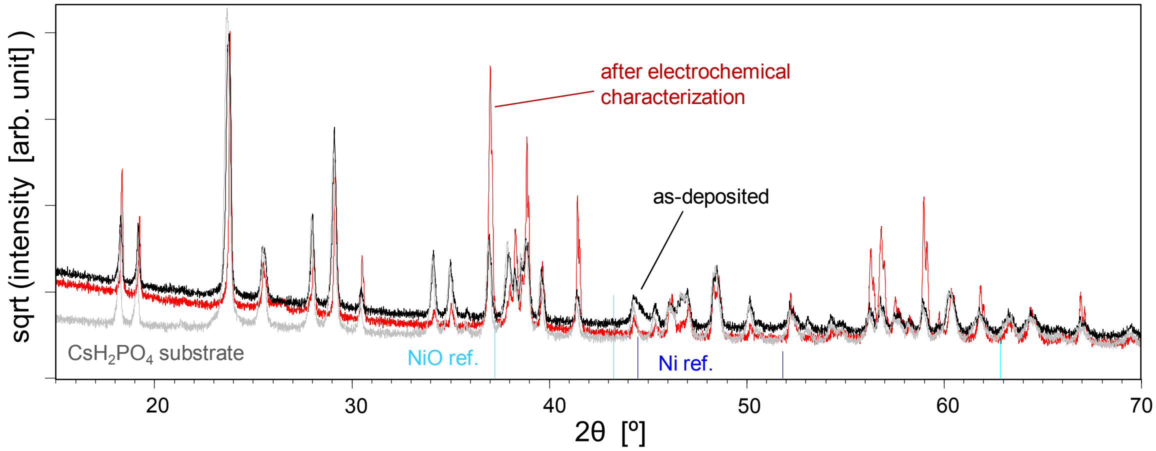

Figure E.3 X-ray diffraction patterns of 100 nm Ni films on top CsH_2PO_4 before and after testing, shown alongside a pattern for CsH_2PO_4 and reference peaks for Ni and NiO. These Ni patterns correspond to the cell shown in Figure E.29(b–c).

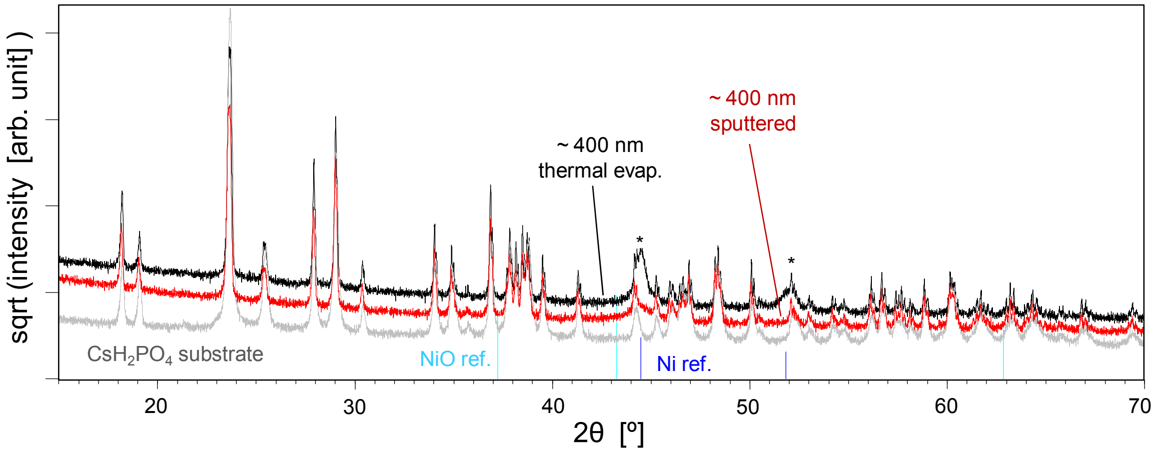

Figure E.4 X-ray diffraction patterns of as-deposited 400 nm Ni films on top CsH_2PO_4 fabricated by thermal evaporation and sputter deposition, alongside pattern for CsH_2PO_4 and reference peaks for Ni and NiO.

Appendix F Pt | $CsHSO_4$ by Atomic Force Microscopy

F.1 Experimental Details

F.1.1 Instrumentation and Setup

Figure F.1 shows photographs of the main components of the electrochemical AFM setup. The copper hotplate, by design, is electrically insulated from the rest of the sample stage (Figure F.1a), and the temperature is controlled using a external temperature controller (Lakeshore Cryotronics, Inc.). The sample (a $CsHSO_4$ half-cell, in this photograph) was placed on top a silver mesh in contact with the copper plate. The silver mesh provided a way to make electrical connection to the counter electrode on the underside of the sample while allowing for gas transport to the counter electrode. Half-cells were clipped onto the stage, as shown, and thermocouples were attached using Kapton tape. In this particular photograph, two thermocouples were present, one attached to the cell surface (T_{surf}) and the other to the hotplate surface (T_{plate}), although the latter was not always used in typical measurements. The sample stage attaches to the microscope under the piezoelectric scanner head (Figure F.1b) and inside the environmental chamber. Gases were fed via flexible plastic tubing and vented into open air at the outlet. The entire assembly was placed into a home-made copper Faraday cage which sat in a vibration isolation chamber (Figure F.1c). Cables exiting this chamber in the photograph were those for electrical measurement (left three cables) and hot stage temperature control (right cable).

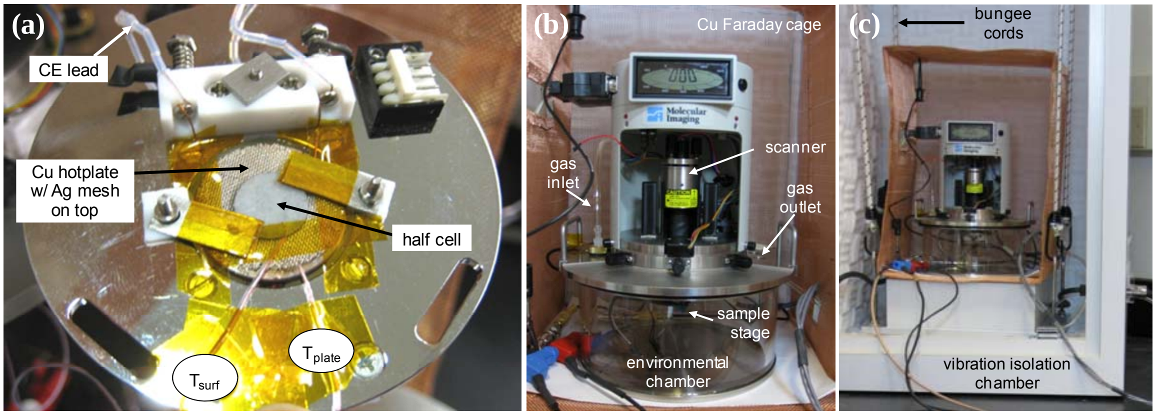

Figure F.1 Photographs of experimental setup for electrochemical AFM: (a) heated sample stage, (b) microscope with environmental chamber, and (c) Faraday cage and vibration isolation unit for noise reduction.

F.1.2 Sample Heating

For imaging at elevated temperatures, heat conductive pastes (often also electrically conducting) pastes are typically used to ensure good thermal contact between the sample and hotplate. In the case of electrochemical AFM measurements, this is not ideal and therefore, we relied on physical contact of the sample and hotplate for heat transfer. To examine how the resulting temperature gradient can influence electrochemical AFM measurements on $CsHSO_4$, we constructed a cell similar to the desired AFM configuration except that the top surface was painted with conductive silver paste (Figure F.2); this enabled measurement of the proton conductivity of $CsHSO_4$ to determine how it varies with the surface and hotplate, both of which are monitored simultaneously (Figure F.1a). As shown in Figure F.3, a relatively large temperature gradient was found to exist across the half-cell, and, moreover, the gradient increases with the set point temperature. For example, to reach the superprotonic transition temperature of ~ 141ºC, a setpoint temperature of ~ 168 ºC, or a hotplate temperature of ~ 158 ºC, is required, implying a temperature gradient of ~ 17 ºC across the $CsHSO_4$ disc. However, simultaneous conductivity measurements of the $CsHSO_4$ sample showed that by a surface temperature of ~ 135 ºC, the sample had already reached its superprotonic phase. This implies that either the method for measuring the surface temperature is not accurate or, more likely, that the $CsHSO_4$ surface need not be above the superprotonic temperature as long as the rest of the sample is sufficiently heated (possibly inducing phase transformation across the entire sample).

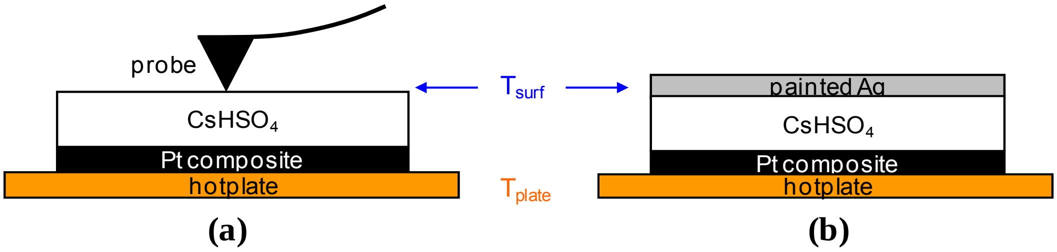

Figure F.2 Schematic of the $CsHSO_4$ cell configuration: (a) typical half-cell configuration for electrochemical AFM and (b) configuration for $CsHSO_4$ conductivity measurements and temperature calibration.

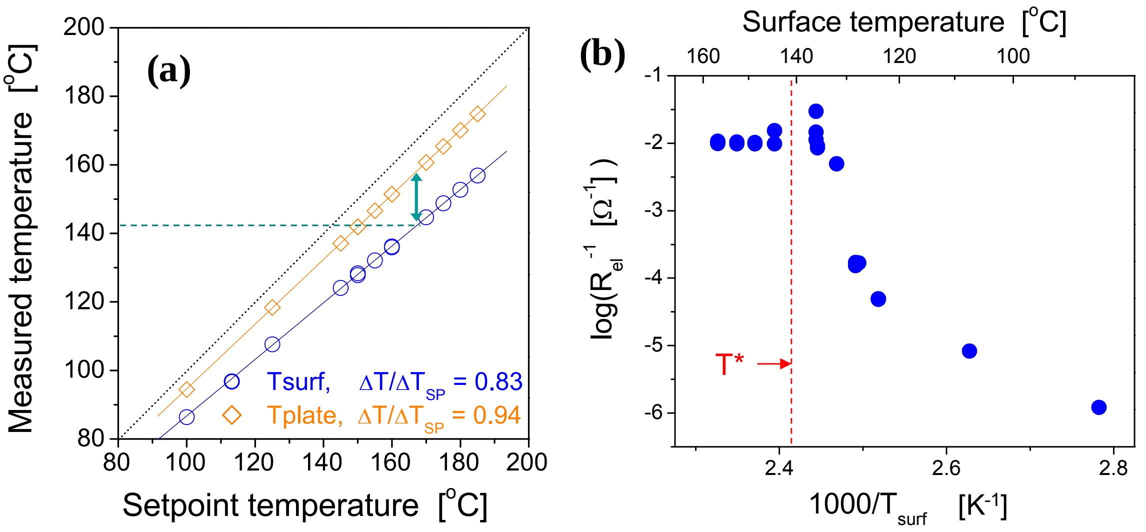

Figure F.3 Analysis of the temperature gradient across CsHSO$_4$: (a) a plot of the measured temperatures, T_{surf} and T_{plate} against the setpoint temperature. Dotted black line denotes slope of 1, and (b) the inverse resistance for proton conduction in CsHSO$_4$ as a function of the surface temperature. Dotted line is the reported phase transition temperature of 141 ºC.

F.2 Data Analysis

F.2.1 Open- and Short-Circuit Corrections

Unlike conventional electrical measurements, electrochemistry by AFM requires extra consideration because of the extremely low currents that are measured. The most important is the open-circuit correction which is an indication of extraneous, high impedance contributions which are in parallel with the sample of interest during electrochemical measurement. A primary component of the open correction is the stray capacitance, resulting from a dielectric residing between the two electrical cables/leads attached to the sample of interest. Figure F.4 is an illustration of how stray capacitance can influence experimental measurements. Given two parallel RC sub-circuits in series (Figure F.4a), we can visualize how a capacitor, C_S, in parallel with the circuit (Figure F.4b) can affect the resulting impedance response. For arbitrarily selected circuit element values ($R_1 = R_2 = 100$ GΩ, $C_1 = 1$ pF, $C_2 = 10$ pF), we generated spectra using various values of stray capacitance (Figure F.4c). From Figure F.4c, it is clear that a stray capacitance comparable to the cell capacitance will result in a masking of the processes. If unaware of the presence of stray capacitance, one would fit the data with two parallel RC sub-circuits (Figure F.4c) thereby obtain errors for the extracted resistor and capacitor values (results not shown). These errors increase with the value of C_S; in the limit of very high values of C_S, only one arc with a resistance of $2R_1$ would be visible; the capacitance of this arc will correspond to the stray value, masking the true capacitance of the electrical process of interest. On the other hand, for stray capacitance values which are small compared to those for the sample of interest, stray capacitance will not play a significant role in the total impedance response and can therefore be neglected; this is usually the case for conventional measurements.

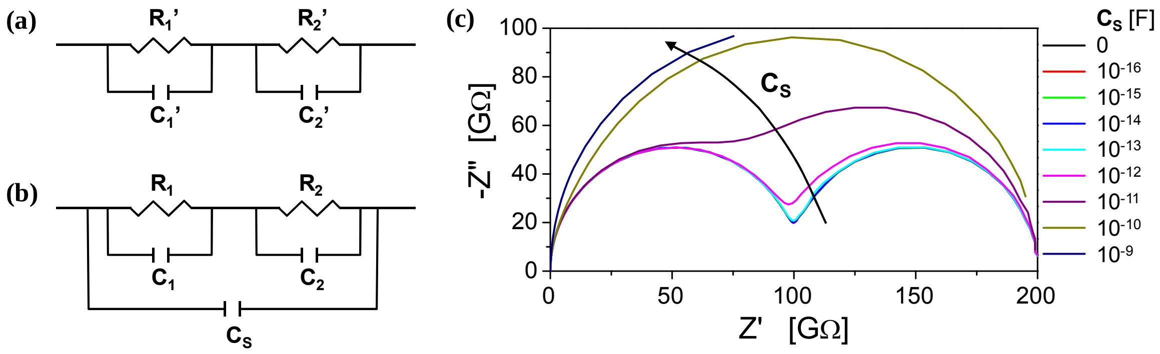

Figure F.4 Illustration of how stray capacitance affects two arbitrary processes: (a) two parallel RC sub-circuits representing the processes of interest, (b) stray capacitance, C_S, in parallel with processes of interest (c) simulation results of the circuit shown in (b) for $R_1 = R_2 = 100$ GΩ, $C_1 = 1$ and $C_2 = 10$ pF and $C_S = 0$–1 nF.

To measure the open correction in the electrochemical AFM system, the probe was withdrawn from the sample surface and the impedance spectrum measured. Although not presented here, the separation distance between the AFM probe and the sample surface did not impact the results of the open-circuit measurement, indicating that the capacitance of air between the probe and sample is negligible compared to contributions from cables and instrumentation. In the electrochemical AFM experimental setup, the stray capacitance was not found to be fixed value. Instead, the open correction measured for the system was found to depend strongly on the internal circuitry of the potentiostat/frequency response analyzer (Figure F.5a); as the current range is varied from 3 pA to 300 mA (where the current range is indicated by its upper current limit), the impedance modulus, $|Z_{stray}|$, decreases. Thus, given that this stray impedance, Z_{stray}, is in parallel with cell impedance, Z_{cell}, (Figure F.5b) measurements performed using a higher current range (of the instrument) will have a greater contribution from spurious effects.

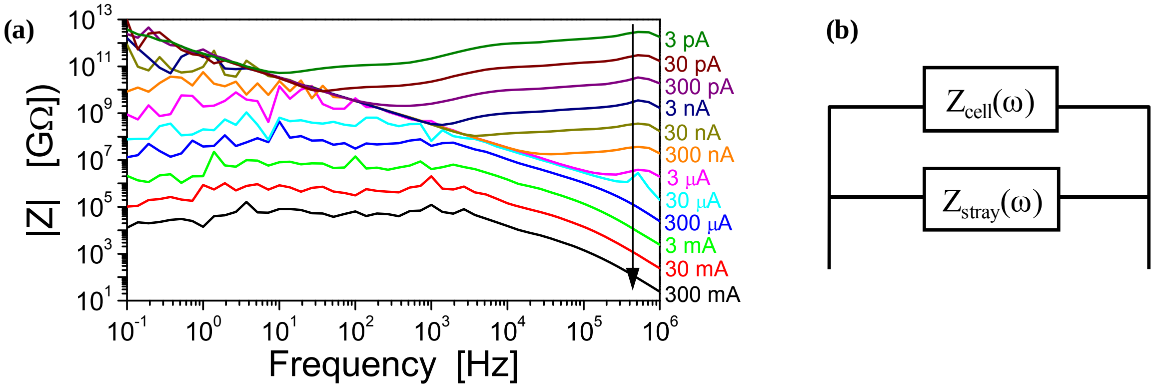

Figure F.5 (a) Bode magnitude plot for open circuit as a function of the current range selected in instrumentation, and (b) a circuit showing how open-circuit resistance (or stray capacitance) affects the cell impedance

To correct for the data collected by AFM, a point-wise open-circuit correction must be applied to the raw data, since a given measurement spans two or three current ranges. To determine the formula for applying the correction, one only needs the expression

$$\frac{1}{Z_{cell}(\omega)} = \frac{1}{Z_{meas}(\omega)} - \frac{1}{Z_{stray}(\omega)} \tag{F.1}$$

where Z_{cell} is the desired, corrected cell impedance, Z_{meas} is the as-measured impedance, and Z_{stray} is the open correction. Only algebraic manipulation of the real and imaginary components is required to compute the stray-corrected cell impedance. This expression is computed at each frequency point; the value of Z_{stray} used at each frequency depends on the specific current range selected by the instrument. Such a point-wise correction was applied to all experimental data collected using the AFM system. An example of an open-circuit correction is shown in Figure F.6 for the Pt | $CsHSO_4$ system.

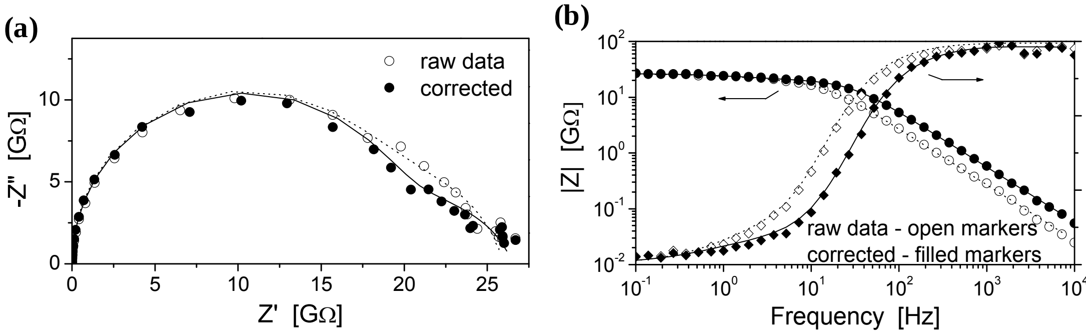

Figure F.6 Representative (a) Nyquist and (b) Bode-Bode plots collected at –1.1 V before and after applying a point-wise open-circuit correction. Data presented are from the Pt | $CsHSO_4$ system at ~ 150 ºC in air, obtained using Probe 6 listed in Table 4.1.

Short corrections are not expected to be as critical for a system which has extremely large impedances. This is confirmed by a measurement of the contact resistance between a Pt-coated AFM probe and Au foil (Figure F.7). The impedance modulus of 5 kΩ and phase angle of zero across all frequencies indicate a purely resistive response, as expected for a metal-to-metal contact.

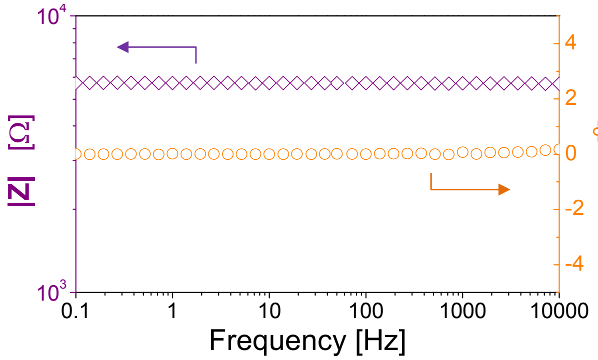

Figure F.7 Representative short-circuit measurement for a Pt-coated AFM probe in contact with a piece of Au foil with a contact force of ~ 0.06 μN. The contact resistance is 5 kΩ and the phase angle, θ, is zero at all frequencies, consistent with a purely resistive response.

F.2.2 Measurement Stability

Thermal drift is an important consideration when performing AFM measurements, as fluctuations in temperature can affect the piezoelectric response of the AFM scanner which controls the *x*-*y*-*z* position of the probe. Thermal drift at elevated temperatures is more severe than at room or low temperature measurements typical of conventional AFM measurements. Figure F.8 shows an AFM image taken at ~ 150 ºC before and after collecting series of cyclic voltammograms and impedance spectra, over the course of ~ 5 h. By tracking the features of the image, the drift was determined to be 0.1 nm s^{-1}. This drift implies that an electrochemical measurement must be performed quickly enough to avoid traversing a long distance which can result in a large variation in electrochemical response. For this reason, cyclic voltammetry is preferred for gathering data for quantitative analysis. That is, the portion of data in cyclic voltammograms used for spatial variation analysis, i.e., the return scan of the cathodic branch, takes only ~ 30 s to complete; this corresponds to a drift of ~ 3 nm, sufficiently small given the AFM tip radius of ~ 40 nm.

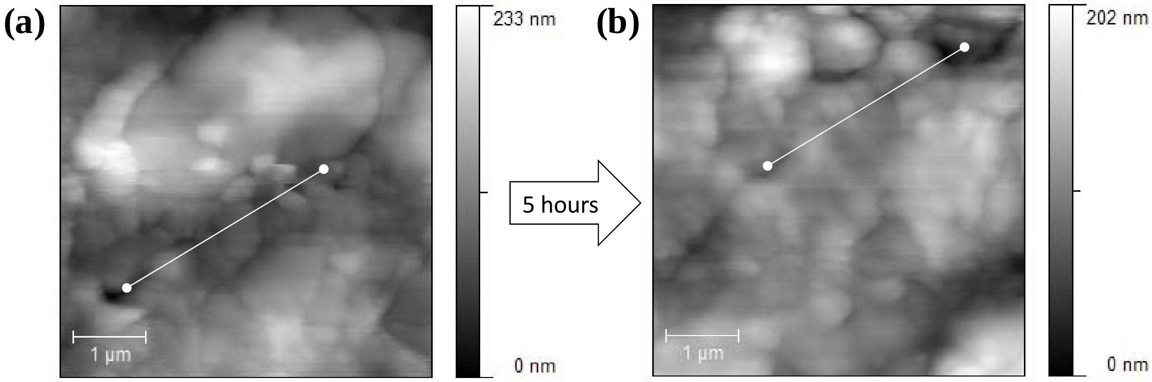

Figure F.8 Topographical AFM image of a $CsHSO_4$ surface (a) before and (b) after acquisition of spatial variation data. Based on this image, a drift rate of 0.1 nm s^{-1} was estimated.

Because of thermal drift issues, it is important to determine that any features in the impedance spectra are not artifacts of drift. We verified that the appearance of two arcs in the impedance spectra was not due to transient effects; Figure F.9 shows that two spectra collected consecutively, with frequencies swept in opposite directions, yield identical impedance responses.

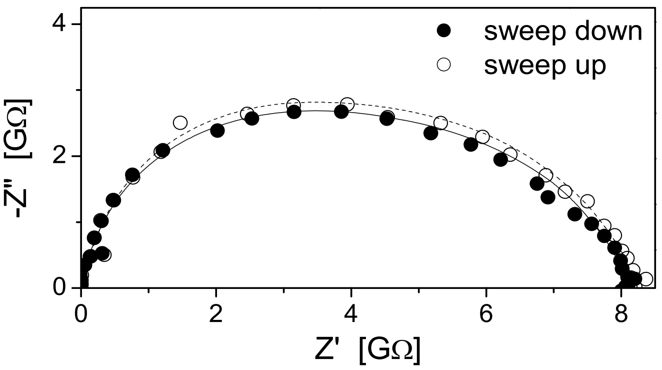

Figure F.9 Two impedance spectra collected consecutively at an applied bias of –1.0 V (using Probe 3 listed in Table 4.1), with the second measured by sweeping the frequency in the opposite direction of the first. The agreement between the two spectra confirms that that the shape of the spectra is not a transient artifact. Spectra were acquired at ~ 150 °C in air (~ 0.03 atm H_2O).

F.2.3 Analysis of Cyclic Voltammograms

Raw cyclic voltammetry data were corrected for a non-zero offset current by fitting to a Butler-Volmer expression (Equation 4.5) with an added constant which typically amounted to 10^{-13} A. A consequence of such a correction is the increased scatter that appears at low overpotentials in the Tafel plots (Figure 4.6). For quantitative analysis of oxygen reduction kinetics, capacitive (transient) effects must be minimized, and thus, voltammograms collected at low scan rates are ideal. We verified that a scan rate of 25 mV s^{-1} employed for acquiring cyclic voltammograms for spatial variation studies does not significantly affect the extracted value of α, implying a negligible impact on the conclusions drawn from data presented here. Figure F.10a shows cyclic voltammograms collected at various scan rates, while Figure F.10b shows α values extracted from fitting of the data to Equation 4.6 (specifically, the linear regime of the Tafel plots, between –0.95 and –0.6 V). Extracted α values range from 0.35 at 400 mV s^{-1} to 0.40 at 5 mV s^{-1}; the deviation in α for the data collected at 25 mV s^{-1} from that at 5 mV s^{-1}, ± 0.01, is well within the variation observed spatially (± 0.1 across six different Pt | $CsHSO_4$ systems. Figure 4.8b).

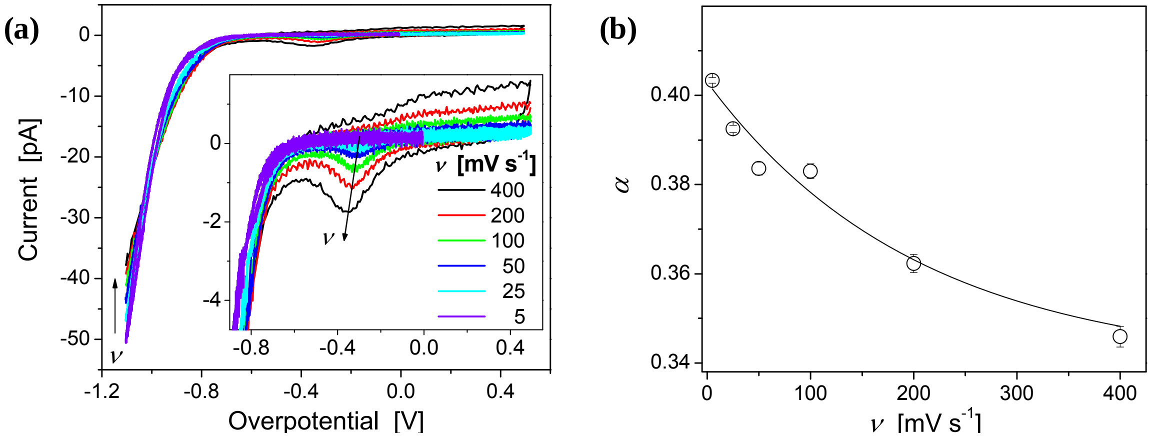

Figure F.10 (a) Cyclic voltammograms for Pt | $CsHSO_4$ collected at scan rates ranging from 400 to 5 mV s^{-1} (using Probe 3 listed in Table 4.1), and (b) corresponding exchange coefficients, α, extracted from fitting the return sweep of the cathodic branch (plotted in Tafel form) to Equation 4.6, showing the dependence of α on scan rate.

F.2.4 Effect of Force on Electrochemical Measurements

We confirmed that any variations in the force applied between the Pt probe and the $CsHSO_4$ surface, determined periodically using force curves, have little effect on the features of the cyclic voltammograms. Figure F.11a is a series of voltammograms collected at a range of forces that is well beyond any force fluctuations observed during electrochemical measurements. Variations in both the oxygen reduction and Pt oxide reduction currents are negligible when the force is doubled, indicating a minimal effect of force on the data presented, and in particular, on the observed spatial variation of electrode kinetics. The agreement between the voltammograms, furthermore, implies that the high-frequency process, which is dominant at high bias, is not a result of contact resistance at the Pt | $CsHSO_4$ interface. We also verified that the process of lifting the probe from and re-approaching the $CsHSO_4$ surface (a procedure required for acquiring electrochemical data at various spatial positions) has a negligible impact on the features of the cyclic voltammogram (Figure F.11b).

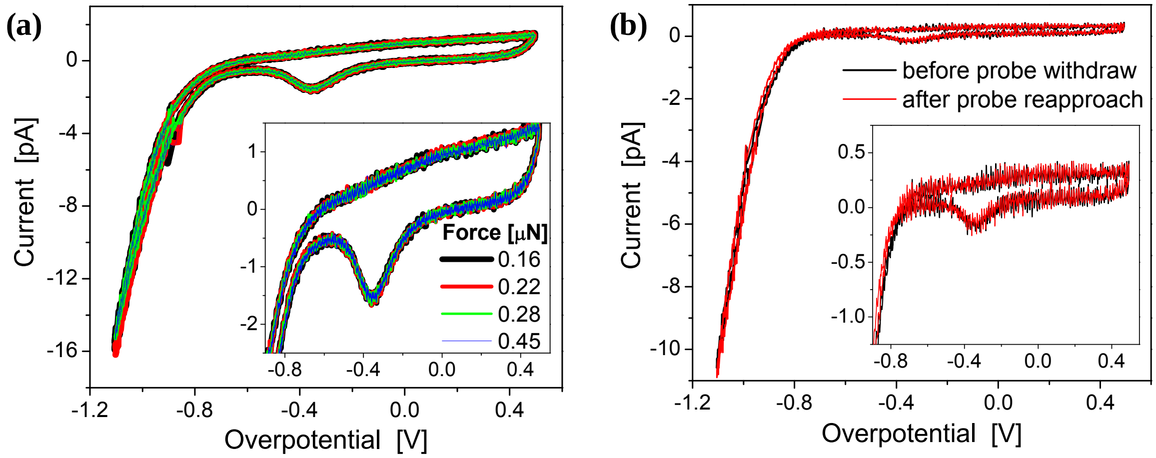

Figure F.11 Cyclic voltammograms for Pt | $CsHSO_4$ collected at ~ 150 °C in humidified air with ~ 0.01–0.03 atm H_2O (a) at forces, ranging from 0.16 to 0.45 μN, applied between the probe and the $CsHSO_4$ surface (Probe 6, Table 4.1) and (b) at the same location on the surface, before withdrawing the probe and after reapproaching (Probe 3, Table 4.1).

F.3 Nano-Pt | $CsHSO_4$ vs. Wire-Pt | CsH_2PO_4

Although it remains inconclusive the source of the correlation between the Butler-Volmer parameters, i_0 and α, there exists some evidence that the activity of the Pt | solid acid interface depends on the morphology of that interface. We compare electrochemical AFM results for the nano-Pt | $CsHSO_4$ interface with those acquired by Sasaki[127] for the Pt wire | CsH_2PO_4 system. For the former, the six data sets from Figure 4.9 are collapsed into one line for ease of presentations (Figure F.12a). Data plotted alongside the AFM results were collected at 235 ºC in oxygen with 0.38 atm H_2O for an asymmetric electrode geometry where the working electrode was a 250 µm Pt wire embedded in a CsH_2PO_4 electrolyte, on the opposing side of which is a composite counter electrode (setup described in detail elsewhere[36]); the results plotted in Figure F.12a were acquired by extracting exchange currents and coefficients for current-voltage curves collected for a single Pt wire | CsH_2PO_4 cell as a function of time (Figure F.12b). The values for both parameters vary with time in such a way so as to yield a correlation between i_0 and α, with a slope comparable to that observed in the nano-Pt | $CsHSO_4$ system. (The higher currents are due to the larger contact area between the Pt wire and CsH_2PO_4.) The electrochemical response of the Pt | CsH_2PO_4 system appears to be related to changes in the nature of the interface with time (Figure F.12b). However, the source of the agreement between i_0-α correlations in nanoscale and microscale systems is not immediately obvious and warrants further exploration. Although the proton transport mechanism in $CsHSO_4$ is similar to that in CsH_2PO_4, microscale measurements of the Pt wire | $CsHSO_4$ system would enable a direct comparison. It would also be valuable to determine if the i_0-α correlation can be observed across multiple Pt wire | solid acid systems.

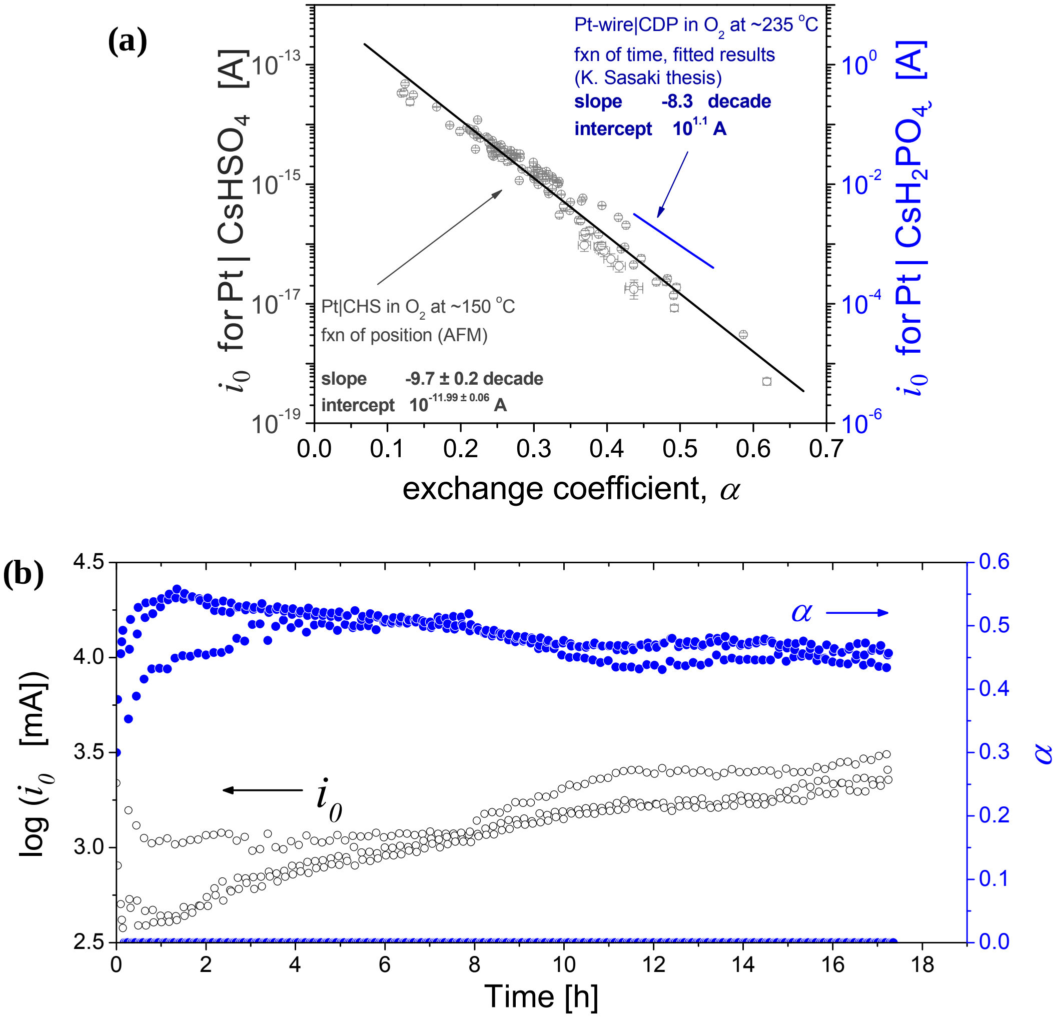

Figure F.12 (a) Plots of exchange current, on a logarithmic scale, as a function of exchange coefficient, comparing the correlation for the Pt | CsHSO$_4$ interface with that for the Pt | CsH$_2$PO$_4$ interface.[127] (b) For Pt | CsH$_2$PO$_4$, values of i_0 and α were extracted from current-voltage data collected as a function of time.

F.4 Platinum Oxide Reduction at Pt | CsHSO$_4$

In this section, we report some preliminary measurements of the Pt oxide reduction kinetics using the nano Pt | CsHSO$_4$ system.

F.4.1 Experimental

Pt oxidation measurements were performed under identical conditions to those reported for oxygen electro-reduction studies in Chapter 4. To study Pt oxidation kinetics, the voltage profile was varied as follows. To examine Pt chemical oxidation behavior, the system was held in air (~ 0.03 atm H_2O) with no voltage applied for times between 0 and 30. After this chemical oxidation step, the voltage was swept from 0 to –1 V at 100 mV s^{-1} in order to measure the Pt oxide reduction peak that was formed. Similarly, to examine Pt electrochemical oxidation behavior, the voltage was swept to 0.5 V at 100 mV s^{-1} at which it was held for times between 0 and 30 min. After each oxidative dwell step, the oxide reduction behavior was examined by sweeping the voltage to from 0.5 to –1 V at 100 mV s^{-1}. Before every chemical or electrochemical oxidation step, the voltage was held at –1 V for 1 min to ensure that the majority of oxides present were removed. It is important to note that, during electrochemical oxidation of Pt at 0.5 V, it is not possible to eliminate contributions from chemical oxidation which may be occurring concurrently.

F.4.2 Results and Discussion

The reduction characteristics of Pt oxides formed by chemical oxidation (Figure F.13a) via,

$$\mathrm{Pt}_{(s)} + \frac{x}{2}\mathrm{O}_{2(g)} \rightarrow \mathrm{PtO}_{\mathrm{x}(s)} \tag{F.2}$$

and electrochemical oxidation (Figure F.13b), via,

$$\mathrm{Pt}_{(s)} + x\mathrm{H}_2\mathrm{O}_{(g)} \rightarrow \mathrm{PtO}_{\mathrm{x}(s)} + 2x\mathrm{H}^+ + 2x\mathrm{e}^- \tag{F.3}$$

are shown in Figure F.13. In the case of chemical oxidation (Figure F.13a), as the oxidation time was increased, the first reduction peak, located at ~ –0.45 V, increased in size between oxidation times of 0 and 5 min, after which the peak size began to decrease. Corresponding to this decrease was the appearance of a second reduction peak at

~ –0.65 V, which increased in size with oxidation time. The onset voltage of the first reduction peak remained relatively constant at ~ –0.2 V despite changes in its size, while the peak voltage shifted to higher overpotentials with oxidation time, particularly at 10 and 30 min. For electrochemical oxidation of Pt (Figure F.13b), a similar behavior was observed, that is, an increase in peak size for oxidation times of 0–5 min, after which the peak decreased in size, concurrent with the appearance of a second reduction peak at larger overpotentials. However, in the case of electrochemical oxidation, the onset voltage occurs at lower overpotentials (below –0.1 V), and the peak position was observed to vary with dwell time more significantly. This may be an indication that electrochemical oxidation of Pt results in the formation of a different form of oxide than that formed by chemical oxidation; this would not be surprising since, based solely on their reactions, one would expect different oxidation pathways. In both cases, the observation of a second reduction peak appearing after long oxidation times suggests that the first reduction peak corresponds to an oxide that is kinetically favored to form, whereas the second reduction peak corresponds to an oxide that is thermodynamically favored. This is consistent with the second reduction peak occurring at larger negative overpotentials which, by definition, implies that the corresponding oxide is thermodynamically more stable than the oxide corresponding to the first reduction peak.

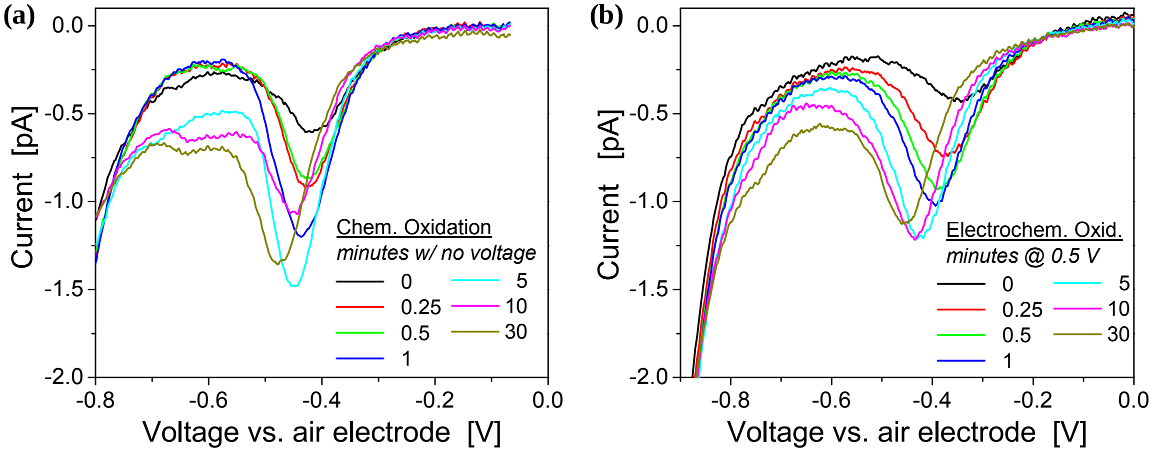

Figure F.13 Pt oxide reduction peaks collected with a 100 mV s^{-1} scan rate at 150 ºC in synthetic air with ~ 0.03 atm H_2O (~ 0.3 μN force) , after dwelling for various times (a) with no voltage applied, for chemical oxidation of Pt and (b) 0.5 V applied, for electrochemical oxidation of Pt.

A more quantitatively analysis of the first reduction peak (at ~ –0.45 V) is presented in Figure F.14. The three parameters, peak voltage, current and area, increase quickly with oxidation time for small oxidation times and appear to reach constant values before decreasing after ~ 5 min, particularly in the case of peak current and area. An increase in peak area means that a larger quantity of material was available for reduction. A plateau of the peak area (amount of oxide formed) with oxidation time is not surprising since as the oxide layer grows thicker, additional oxidation becomes more difficult because of the requirement that oxygen diffuse through the formed oxide layer (or that water, protons and/or electrons be transported through the layer in the case of electrochemical oxidation). A shifting peak voltage while maintaining a relatively constant onset voltage implies that with longer oxidation times, the resulting oxide is kinetically more difficult to reduce.

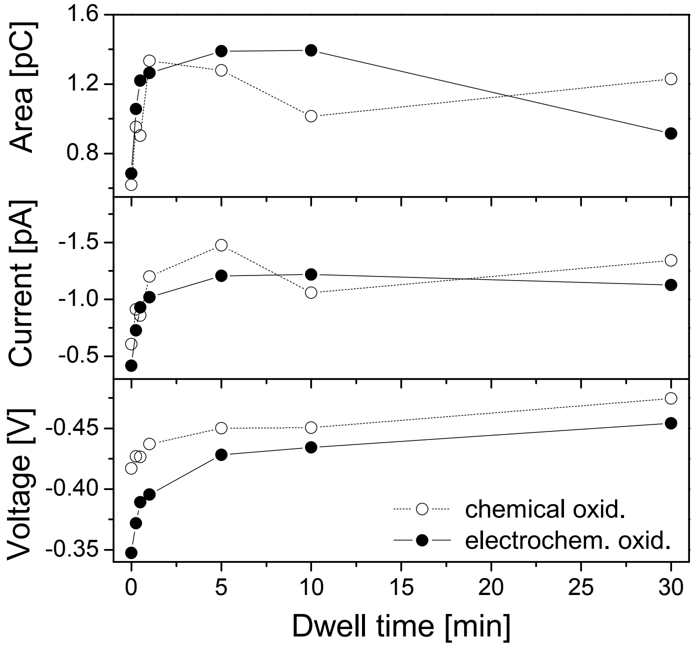

Figure F.14 Peak voltage, current and integrated area for the electrochemical reduction of Pt oxide (Figure F.13) as a function of dwell time at chemically and electrochemically oxidizing conditions.

F.5 Oxygen Electro-Reduction at Pt | Single-crystal $CsHSO_4$

In this section, we examine the spatial variation of electrocatalysis in the Pt | $CsHSO_4$ system, in which $CsHSO_4$ single crystals rather than a polycrystalline discs were employed. Because surface heterogeneities of single crystals are expected to be minimized, we attempt to exploit such a system to confirm the correlation between surface structure and electrochemical activity.

F.5.1 Experimental

Single crystals of $CsHSO_4$ were grown from a saturated aqueous solution made by dissolution of $CsHSO_4$ powder in de-ionized water. The resulting solution was filtered through a syringe filter (0.2 μm filter size) to remove dust particles and left, covered, at ambient conditions to allow water evaporation and crystal precipitation. Crystals were removed from solution and rinsed with water followed immediately by methanol before drying in air.

Select crystals of appropriate dimensions, typically those which were > 5 mm on edge and > 1 mm thick, were sputtered on both faces with 25 nm of platinum (Cressington 208HR, ~ 15 mTorr Ar, 80 mA plasma current). After sputtering and immediately before use in AFM studies, the crystal was fractured laterally, using a razor blade, to generate two $CsHSO_4$ half-cells. Half-cells fabricated from un-fractured single crystals, pulled directly from solution and sputtered on one face with Pt, were also used for electrochemical AFM measurements.

The single-crystal half-cells were placed on top of a metal mesh which, in turn, sat on top of the AFM hotstage. Electrical connection to the counter electrode was made via this metal mesh (see Section F.1.1). Electrochemical characterization of the crystals via AFM was done so using the same procedures as those employed for polycrystalline samples (Chapter 4).

It is important to note that any residual acid on the single crystal can greatly influence the electrochemical response. Figure F.15 shows cyclic voltammograms collected from a Pt probe in contact with the surface of an un-fractured, as-grown single-crystal surface. Unlike the response for polycrystalline $CsHSO_4$ samples (Figure F.10a), these voltammograms displayed additional transient features at ~ –0.6 V on the cathodic sweep and at ~ –0.75 and –0.3 V on the return anodic sweep. Although the source of the features has not been determined, the features agree reasonably well with those reported in literature for aqueous acidic electrolyte systems for which peaks associated with hydrogen adsorption and desorption onto Pt are well-known characteristics of the voltammogram.[92–96] This observation provides some evidence that such adsorption processes occur only in aqueous/liquid acid systems and that the absence of adsorption features in solid acid systems (Chapter 4) is not solely a consequence of the higher temperatures employed.

The presence of even a small amount of acid causes large variations in the electrochemical response (Figure F.16). Furthermore, once a probe is contaminated with acid, the acid remains at the Pt | $CsHSO_4$ interface for any subsequent $CsHSO_4$ samples. To ensure that the electrochemical response examined is that due to the solid acid $CsHSO_4$ electrolyte rather than residual sulfuric acid, samples (both poly- and single-crystalline) must be rinsed adequately with methanol. Fractured single crystals must be examined visually to ensure that self-enclosed pockets of solution did not contaminate the fractured surface.

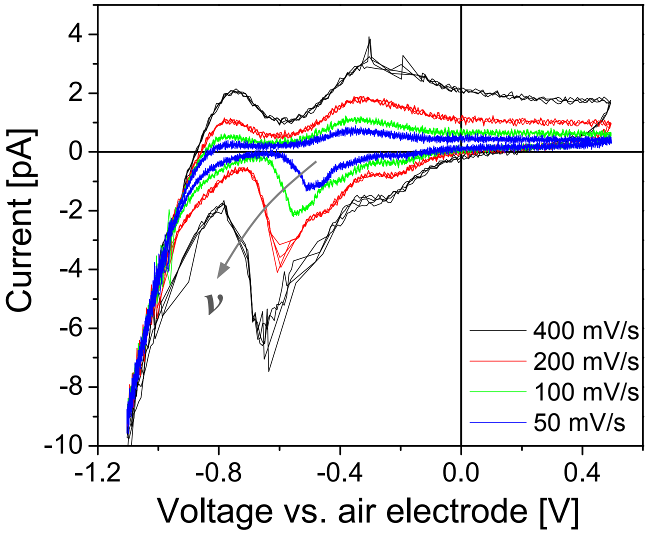

Figure F.15 Cyclic voltammograms for a Pt probe in contact with the surface of an as-grown $CsHSO_4$ single crystal. Data shown were collected at ~ 150 ºC in synthetic air with ~ 0.03 atm H_2O at several different scan rates.

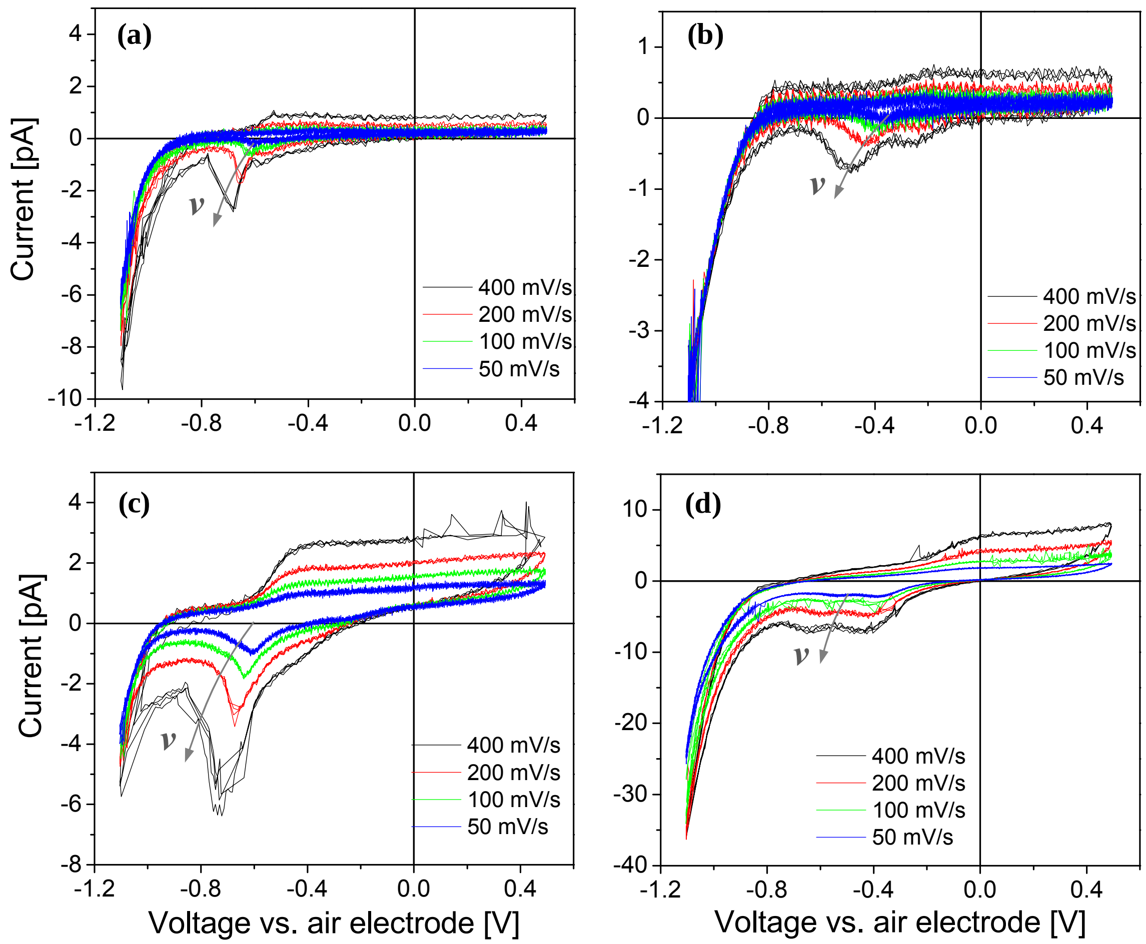

Figure F.16 Cyclic voltammograms for a Pt probe in contact with single-crystal $CsHSO_4$, contaminated with acidic solution, showing the variability in the transient response. (a) and (b) correspond to different probes on the same crystal, and voltammograms shown in (c) and (d) were collected from same Pt | $CsHSO_4$ system but at two different positions on the crystal surface.

F.5.2 Results and Discussion

Figure F.17a shows the cyclic voltammogram for the Pt | $CsHSO_4$ system in which the single-crystal surface under examination was obtained by fracturing. Like the polycrystalline $CsHSO_4$ system, the single-crystal response displayed transient features with broad peaks centered at approximately –0.4 V and 0.1 V for cathodic and anodic sweeps of the voltammograms, respectively. These peaks were overlaid with an oxygen electro-reduction current which reaches ~ 5 pA at –1.1 V. A typical impedance response for this system is shown in Figure F.17b for overpotentials from –1.2 to –0.7 V. For the overpotential range shown, the impedance response was comprised of one arc which varied significantly in size as a function of overpotential. Specifically, the electrode resistance decreased exponentially with overpotential, as indicated by the linear behavior of resistance (on a log scale) when plotted against overpotential (not shown). This behavior is consistent with the DC response, obtained from cyclic voltammetry (25 mV s^{-1} and plotted in Tafel form (Figure F.18a). A plot of the current, on a logarithmic scale, as a function of overpotential yields a straight line.

Qualitatively, the voltammograms collected for Pt in contact with single-crystal and polycrystalline surfaces are similar; both Pt oxidation and oxide reduction peaks were visible, although their kinetics may differ slightly. However, unlike polycrystalline samples, single-crystal samples display only one impedance arc that is overpotential dependent, indicating that the ohmic response at high frequencies is negligible.

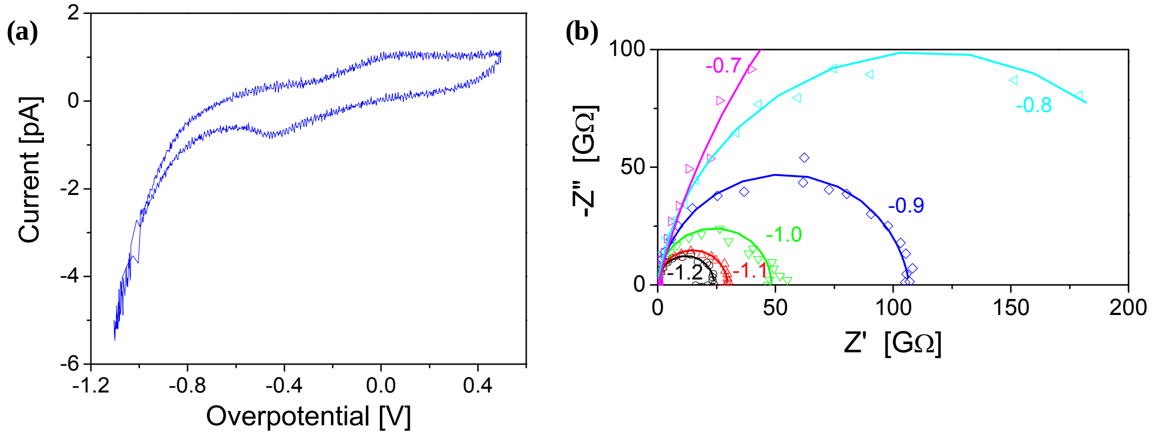

Figure F.17 (a) Cyclic voltammogram for Pt | single-crystal $CsHSO_4$ collected with a scan rate of 100 mV s^{-1}, and (b) Nyquist spectra for Pt | single-crystal $CsHSO_4$ collected as a function of overpotential. Lines are fits to a parallel RQ circuit. Data are collected at ~ 150 ºC in air with ~ 0.3 atm H_2O.

Extracted α and i_0 values, obtained from the Tafel plots in Figure F.18a and from a second fractured single-crystal sample (not shown), are plotted in Figure F.18b, alongside polycrystalline data. A correlation between the two kinetic parameters exists, and, moreover, the behavior is similar to that observed for polycrystalline $CsHSO_4$ samples. Specifically, the slopes of α vs. i_0 are similar between the single-crystal and polycrystalline samples. More interestingly, the variability of α and i_0 for the single-crystal samples ($\Delta\alpha \approx 0.15$ and 0.05 for sets 1 and 2, respectively) is similar to that observed for polycrystalline $CsHSO_4$. This implies that the heterogeneity of electrochemical kinetics across a single-crystal surface (across a comparable sample area of 5 µm × 5 µm) is not significantly different from that across a polycrystalline surface.

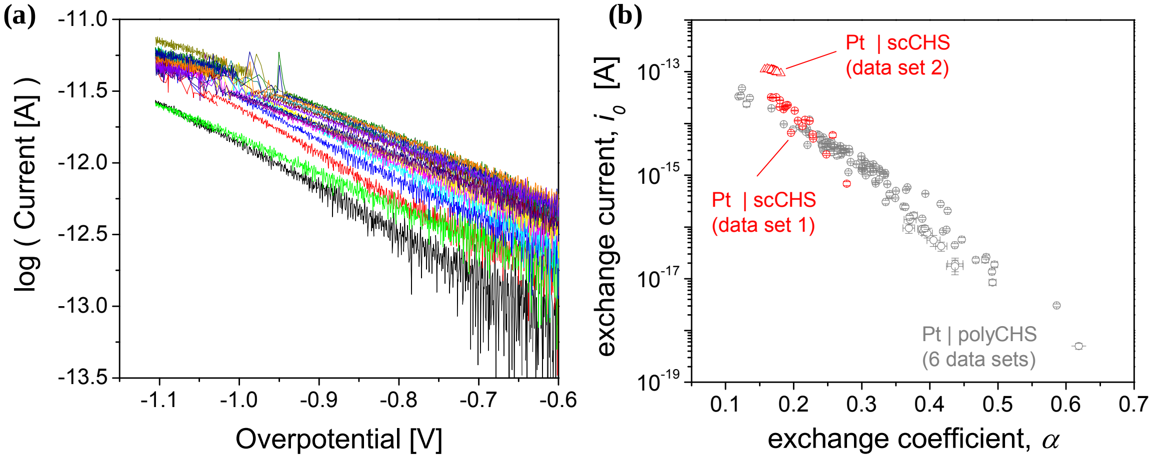

Figure F.18 (a) Tafel plots for the Pt | single-crystal $CsHSO_4$ interface taken from the return scans of cyclic voltammograms collected at 25 mV s^{-1} and (b) extracted values of exchange current (log scale) plotted against exchange coefficient for two sets of single-crystal experiments, overlaid with polycrystalline $CsHSO_4$ data (Figure. 4.9). Data set 1 corresponds to the plots shown in Figure F.17 and Figure F.18a.

A closer examination of the single-crystal surfaces reveal that, although as-fractured surfaces were smooth, they were damaged by the AFM probe during measurement. An AFM topography image of $CsHSO_4$ at superprotonic conditions shows indentations on the surface (Figure F.19). Additional investigation revealed that the damage is a consequence of the force applied to the sample by the probe rather than the overpotentials across the $Pt | CsHSO_4$ interface during electrochemical measurements. Based on this observation and the apparently spatial variation of the electrochemical response (Figure F.18), it is reasonable to conclude that single crystals of $CsHSO_4$, known to be plastic at superprotonic conditions, are not ideal as smooth substrates, that is, they essentially become polycrystalline samples once the AFM probe makes contact. It should be noted that indentation is not frequently observed in polycrystalline samples due to the roughness of the surface, although it is also likely to occur.

Figure F.20 displays additional images of damaged single-crystal surfaces. Even contact mode AFM probes (with nominal spring constants below $0.1\ N\ m^{-1}$) have been observed to indent single crystals of $CsHSO_4$ (Figure F.20). However, since the actual spring constants of most conventional AFM probes can deviate significantly their nominal values, leading to irreproducible indentation behavior, it is not possible, without well-calibrated AFM probes, to identify the value of force at which $CsHSO_4$ deforms.

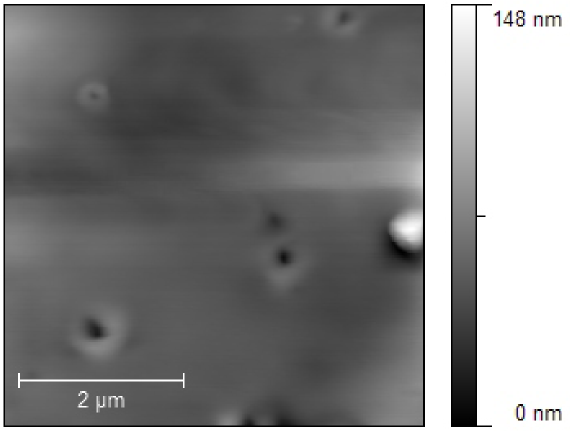

Figure F.19 AFM topography image of a single-crystal $CsHSO_4$ surface, in situ at 150 ºC, after the Pt-coated AFM probe was held various locations on the crystal.

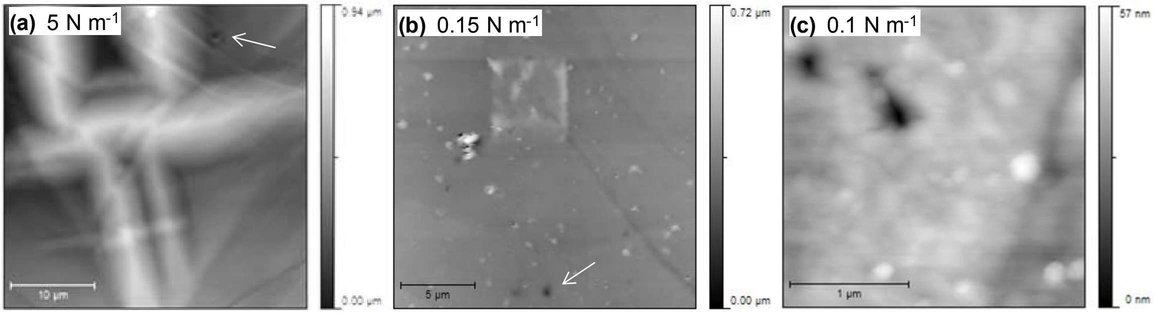

Figure F.20 Additional images of $CsHSO_4$ single-crystal surfaces showing that even probes with nominally low spring constants can damage the sample. (a) fractured crystal surface, (b) fractured crystal surface for which the square region is a damaged from a prior scan window, and (c) as-grown crystal.

Appendix G Pt | $Ba_{3-x}K_xH_x(PO_4)_2$ by Atomic Force Microscopy

G.1 Introduction

A series of compounds with the formula $Ba_{3-x}K_xH_x(PO_4)_2$ for $x \approx 0.5$–1 have been synthesized[24] and shown to crystallize in the trigonal phase. The motivation to synthesize such a compound was based on the structural similarities between the trigonal compound, $Ba_3(PO_4)_2$, and superprotonic solid acid compounds with the stoichiometry, $M_3H(PO_4)_2$, such as $Rb_3H(SeO_4)_2$ which is known to undergo a phase transition from monoclinic to trigonal at ~ 180 ºC. Incorporation of protons into $Ba_3(PO_4)_2$ by substitution of Ba^{2+} with K^+ results in trigonal $Ba_{3-x}K_xH_x(PO_4)_2$ which is stable up to 300 ºC. Thus, unlike its analogs, $Ba_{3-x}K_xH_x(PO_4)_2$ does not undergo a phase transformation. $Ba_{3-x}K_xH_x(PO_4)_2$ possesses the additional advantage of insolubility in water. However, the proton conductivity is two to three orders of magnitude lower than typical solid acid compounds. Specifically, the proton conductivity of $Ba_{2.2}K_{0.8}H_{0.8}(PO_4)_2$ at 250 ºC is 2.4×10^{-5} S cm^{-1}, much lower than the value of 2×10^{-2} S cm^{-1} for CsH_2PO_4.[10]

Although $Ba_{3-x}K_xH_x(PO_4)_2$ exhibits low proton conductivity, it provides several advantages for exploring the spatial variability of electrocatalysis in solid state systems. Preliminary observation of the morphology of $Ba_{3-x}K_xH_x(PO_4)_2$ crystallites reveal smooth faceted surfaces, unlike those typical of water-soluble solid acid compounds, and is suggestive of its ideal mechanical properties for use with a AFM probe as the working electrode. As discussed in Chapter 2 and shown in Figure F.19 and Figure F.20 for $CsHSO_4$, many of the typical solid acid compounds have unfavorable mechanical properties, such plastic deformation of the superprotonic phase, for exploring the correlation between surface structure and electrochemical kinetics. In this section, we attempt to use $Ba_{3-x}K_xH_x(PO_4)_2$ as an electrolyte for studying oxygen electro-reduction kinetics at the Pt | $Ba_{3-x}K_xH_x(PO_4)_2$ interface.

G.2 Experimental

The synthesis of $Ba_{3-x}K_xH_x(PO_4)_2$ powder from two aqueous solutions, one of barium acetate and the other containing dipotassium hydrogen phosphate and potassium hydroxide. The general procedure and starting materials are report elsewhere.[24] For the $Ba_{3-x}K_xH_x(PO_4)_2$ powder used in this work, the synthesis temperature was kept at 80 ºC and the pH of the solution greater than 13. Powders were characterized with X-ray diffraction and scanning electron microscopy with an energy dispersive spectrometer for composition determination.

Because of the relatively low proton conductivity of $Ba_{3-x}K_xH_x(PO_4)_2$, the use of half-cells comprised of thick polycrystalline electrolyte membranes (~ 0.5 mm) in conjunction with a nanoscale working electrode, generated currents too low to be measurable. We verified this by fabricating a macroscale cell comprised of polycrystalline $Ba_{3-x}K_xH_x(PO_4)_2$ electrolyte membrane with a large composite Pt-$Ba_{3-x}K_xH_x(PO_4)_2$ counter electrode, similar to that for polycrystalline $CsHSO_4$ half-cells used in Chapter 4. Electrochemical measurements performed on this cell using a Pt-coated probe yielded zero current for all overpotentials (not shown), indicating that ~ 0.5 mm thick $Ba_{3-x}K_xH_x(PO_4)_2$ electrolytes are too resistive to be useful for electrochemical AFM measurements.

As such, we constructed an electrochemical cell for which the electrolyte membrane is a single micron-sized particle of $Ba_{3-x}K_xH_x(PO_4)_2$ such that the resistance of the electrolyte is small relative electrocatalysis at the Pt | $Ba_{3-x}K_xH_x(PO_4)_2$ interface (Figure G.1). To construct such a geometry, $Ba_{3-x}K_xH_x(PO_4)_2$ powder was first suspended in methanol by sonication. The suspension was allowed to settle for approximately one hour to remove large aggregates of powders, and the remaining suspension of particles was collected and deposited drop-wise onto a Pt-coated silicon substrate (single crystal, 10 mm × 10 mm wafer, 50 nm Pt). To evaluate whether the contact at the $Ba_{3-x}K_xH_x(PO_4)_2$ | Pt-coated wafer (i.e., current collector) interface obtained by this method was sufficient so as to not limiting electrochemical currents, the fabrication procedure was modified as follows. The $Ba_{3-x}K_xH_x(PO_4)_2$ suspension was first dripped onto a bare silicon wafer (Wafer 1), and the resulting wafer was sputtered with 10 nm Pt. This coated substrate was then placed in contact with a second Si substrate (Wafer 2), already pre-coated with Pt, in order to transfer the Pt-coated $Ba_{3-x}K_xH_x(PO_4)_2$ platelets from Wafer 1. Thus, the $Ba_{3-x}K_xH_x(PO_4)_2$ | Pt contact at the counter electrode was guaranteed by the intimate contact imparted by sputter deposition, while the physical contact between metals, specifically between the platinum films on the $Ba_{3-x}K_xH_x(PO_4)_2$ and on the Si wafer, is considered adequate for current collection.

For electrochemical AFM measurements, the wafer was placed on an AFM hotstage, and electrical connection was made to the Pt film counter electrode by clipping a small piece of silver mesh onto the top edge of the Pt-coated wafer. Measurements were carried out at temperatures of 175–220 ºC under flowing synthetic air with ~ 0.03 atm H_2O supplied by flowing the inlet gas through a water bubbler at room temperature. A potentiostat equipped with a frequency response analyze and a femtoammeter (ModuLab by Solartron Analytical) was used to perform cyclic voltammetry measurements (100 mV s^{-1} scan rate between –1.1 and 0.6 V).

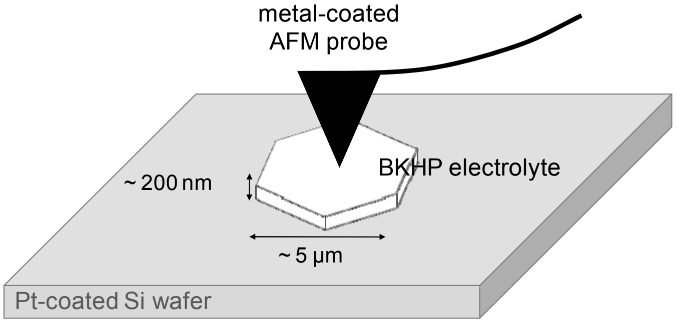

Figure G.1 Schematic of experimental setup for electrochemical AFM measurements of $Ba_{3-x}K_xH_x(PO_4)_2$ electrolytes. Half-cells are comprised of micron-sized hexagonal platelets of $Ba_{3-x}K_xH_x(PO_4)_2$ sitting on a Pt counter electrode. The AFM probe serves as a small working electrode that completes the circuit.

G.3 Results and Discussion

G.3.1 $Ba_{3-x}K_xH_x(PO_4)_2$ Characteristics

The diffraction pattern for the $Ba_{3-x}K_xH_x(PO_4)_2$ powder (not shown) agrees with the trigonal phase, as reported previously.[24] SEM micrographs of the powders (Figure G.2) show a distinct particle microstructure with hexagonal platelets ~ 5 μm wide and ~ 200 nm thick. The observation of a hexagonal shape is consistent with the trigonal symmetry of $Ba_{3-x}K_xH_x(PO_4)_2$. Also visible in the SEM micrograph is the intergrowth of multiple platelets, resulting in aggregates at least several microns in size. Such aggregates, if deposited onto a smooth Si substrate for AFM studies, may cause damage to the probe since the AFM scanner only has a *z*-range of ~ 7 μm. For obtaining a good distribution of individual, flat electrolyte platelets for electrochemical AFM studies, removal of such aggregates from the suspension done so by settling of the suspension.

The morphology of the powders reveal rather smooth surfaces, notable different from typical solid acid powders, such as those for CsH_2PO_4, shown in Figure G.2b for comparison. Unlike $Ba_{3-x}K_xH_x(PO_4)_2$, particles of CsH_2PO_4 are easily agglomerated, with a large range of particle and aggregate sizes. From the energy dispersive spectra, the $Ba_{3-x}K_xH_x(PO_4)_2$ powders used in these studies were determined to have a potassium content (and therefore proton content) of x = 0.75.

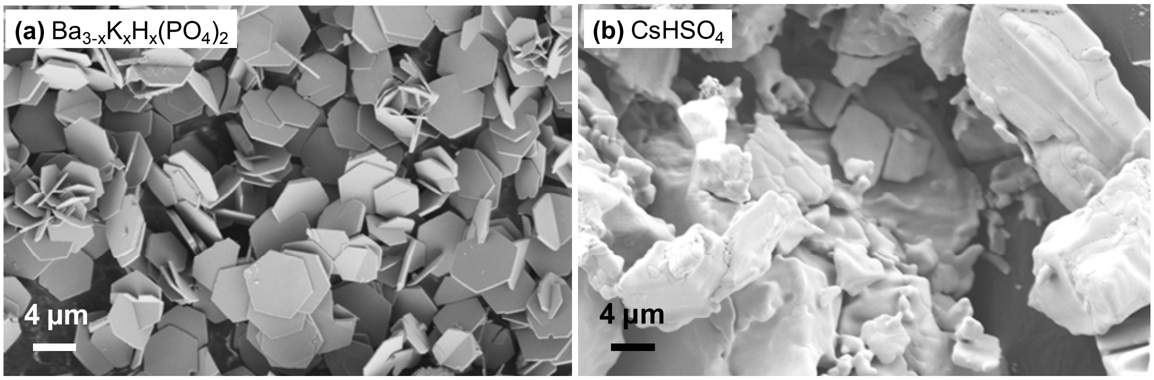

Figure G.2 SEM micrograph of (a) $Ba_{3-x}K_xH_x(PO_4)_2$ powder (x = 0.75) showing typical microstructure obtained for platelet $Ba_{3-x}K_xH_x(PO_4)_2$ powders and (b) as-synthesized $CsHSO_4$ powders, for comparison.

G.3.2 Fabrication of Microscale $Ba_{3-x}K_xH_x(PO_4)_2$ Half-cells

Figure G.3 shows SEM micrographs of $Ba_{3-x}K_xH_x(PO_4)_2$ particles on top of a Pt-coated Si wafer obtained by dripping of a particle-methanol suspension onto the wafer. The distribution across the entire wafer was non-uniform because of methanol evaporation patterns (not shown). On the scale shown in Figure G.3a, the particles are uniformly distributed. Thus, given a maximum scan range of 35 × 35 μm^2 in atomic force microscope, appropriate regions for AFM studies are available and can be examined by proper alignment of substrate and AFM probe. It should be noted that sample alignment is difficult because the AFM system employed in our studies lacks an optical microscope. Thus, we rely on fabrication techniques to obtain a sufficiently high density of platelets such that $Ba_{3-x}K_xH_x(PO_4)_2$ substrates can be found during an AFM scan. Figure G.3b is a higher magnification image showing platelets which were lying on the substrate in the preferred orientation. While Figure G.3 reveals several aggregates of platelets, proper processing, i.e., settling of the larger aggregates in the suspension, was determined to minimize the number of aggregates and therefore reduce the likelihood of damaging the AFM tip during electrochemical measurements. Once the concentration of aggregates in the suspension is minimized, the concentration of individual platelets on the surface of the silicon substrate can be increased by repeated addition of solution onto the wafer.

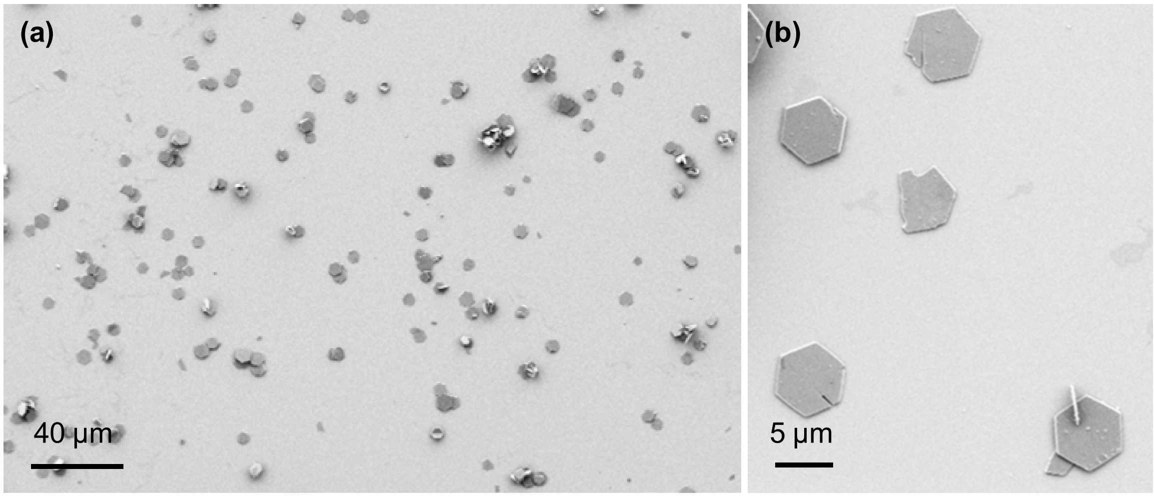

Figure G.3 SEM micrographs of $Ba_{3-x}K_xH_x(PO_4)_2$ platelets on a Pt-coated Si wafer, obtained by dripping a $Ba_{3-x}K_xH_x(PO_4)_2$-methanol suspension. Under an electron beam, $Ba_{3-x}K_xH_x(PO_4)_2$ platelets appear as darker regions due to its poor electrical conductivity relative to the Pt film.

Figure G.4 shows a series of SEM micrographs of $Ba_{3-x}K_xH_x(PO_4)_2$ deposited on silicon, used in the wafer-to-wafer transfer process discussed in the experimental section. The top row contains images of a $Ba_{3-x}K_xH_x(PO_4)_2$ deposited on Wafer 1 (as discussed in the experimental section) after contact was made to Wafer 2, thus depicting missing platelets. The bottom row contains images of Wafer 2 after contact and acquisition of platelets from Wafer 1. Under the electron beam, darker regions are those with relatively poor electronic conductivity compared to brighter regions and corresponds to exposed portions of the Si substrate (Wafer 1, top row) or to uncoated $Ba_{3-x}K_xH_x(PO_4)_2$ platelets (Wafer 2, bottom row). By examining the two substrates, it is clear that a large fraction of the coated $Ba_{3-x}K_xH_x(PO_4)_2$ platelets on Wafer 1 were transferred upon contact to Wafer 2. It was also observed that larger aggregates are often fractured into smaller pieces (Figure G.4f) during the transfer step.

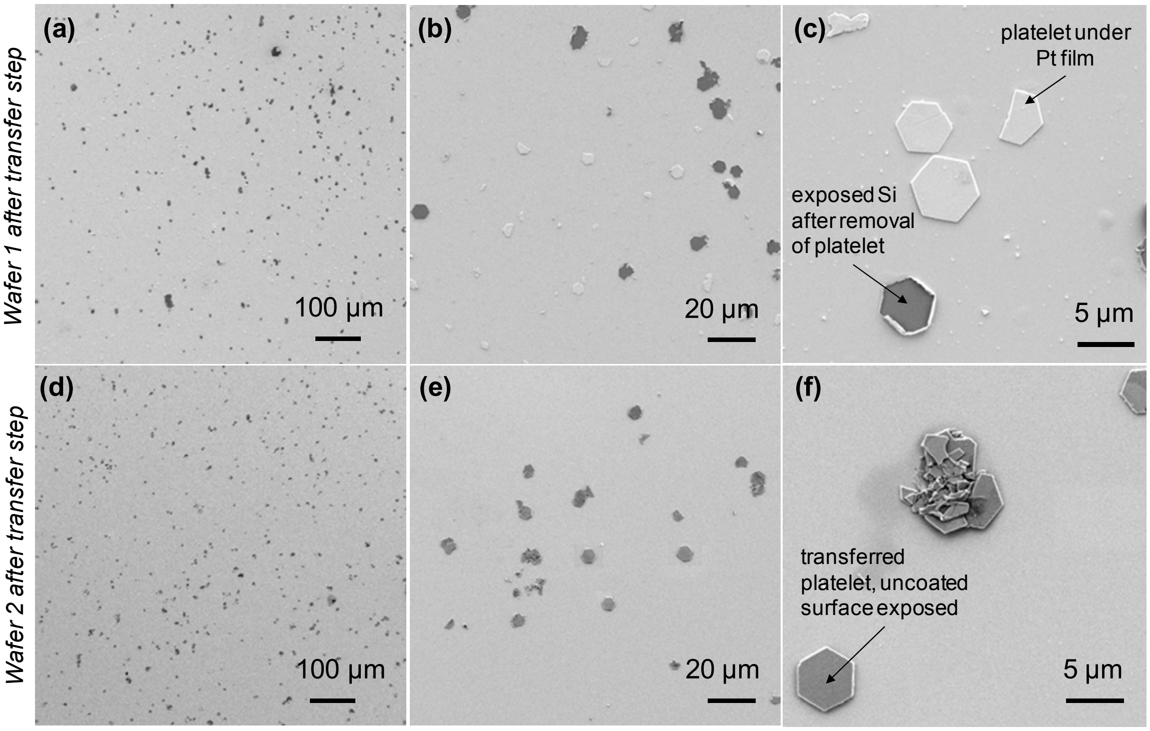

Figure G.4 SEM micrographs of $Ba_{3-x}K_xH_x(PO_4)_2$ platelets on silicon wafer used for the transfer of Pt-coated $Ba_{3-x}K_xH_x(PO_4)_2$ platelets from Wafer 1 (top row) to Wafer 2 (bottom row). (a–c) show $Ba_{3-x}K_xH_x(PO_4)_2$ deposited on a bare silicon substrate (Wafer 1), on top of which is a film of Pt, after contact to Wafer 2. Dark gray hexagonal regions are where $Ba_{3-x}K_xH_x(PO_4)_2$ platelets were transferred off of the wafer, whereas brighter hexagonal regions are un-transferred platelets, coated with Pt. (d–f) shows the transferred $Ba_{3-x}K_xH_x(PO_4)_2$ platelets, sitting on a Pt-coated Si wafer (Wafer 2).

G.3.3 Oxygen Electro-reduction at Pt | $Ba_{3-x}K_xH_x(PO_4)_2$

Figure G.5 shows a topographical image of a $Ba_{3-x}K_xH_x(PO_4)_2$ platelet (uncoated and deposited directly onto a Pt-coated Si wafer) and the corresponding cyclic voltammograms collected at three different positions on the platelet. Although Figure G.5(b–c) shows voltammograms that are reproducible with cycle and consistent with expectations for the Pt | solid acid interface (see Pt | $CsHSO_4$), subsequent measurements (Figure G.5d) display a degradation in current followed by a sharp drop during Cycle 4. While the drop in current shown in Figure G.5d is consistent with degradation and wear of the tip, subsequent measurements with the same probe yielded voltammograms that vary in current, between zero and finite values in a random fashion. Voltammograms collected for the Pt probe in contact with wafer (off of the Ba$_{3-x}$K$_x$H$_x$(PO$_4$)$_2$ platelet) also yielded irreproducible results, displaying zero current for the most part with intermittent high currents (consistent with a metal-metal contact).

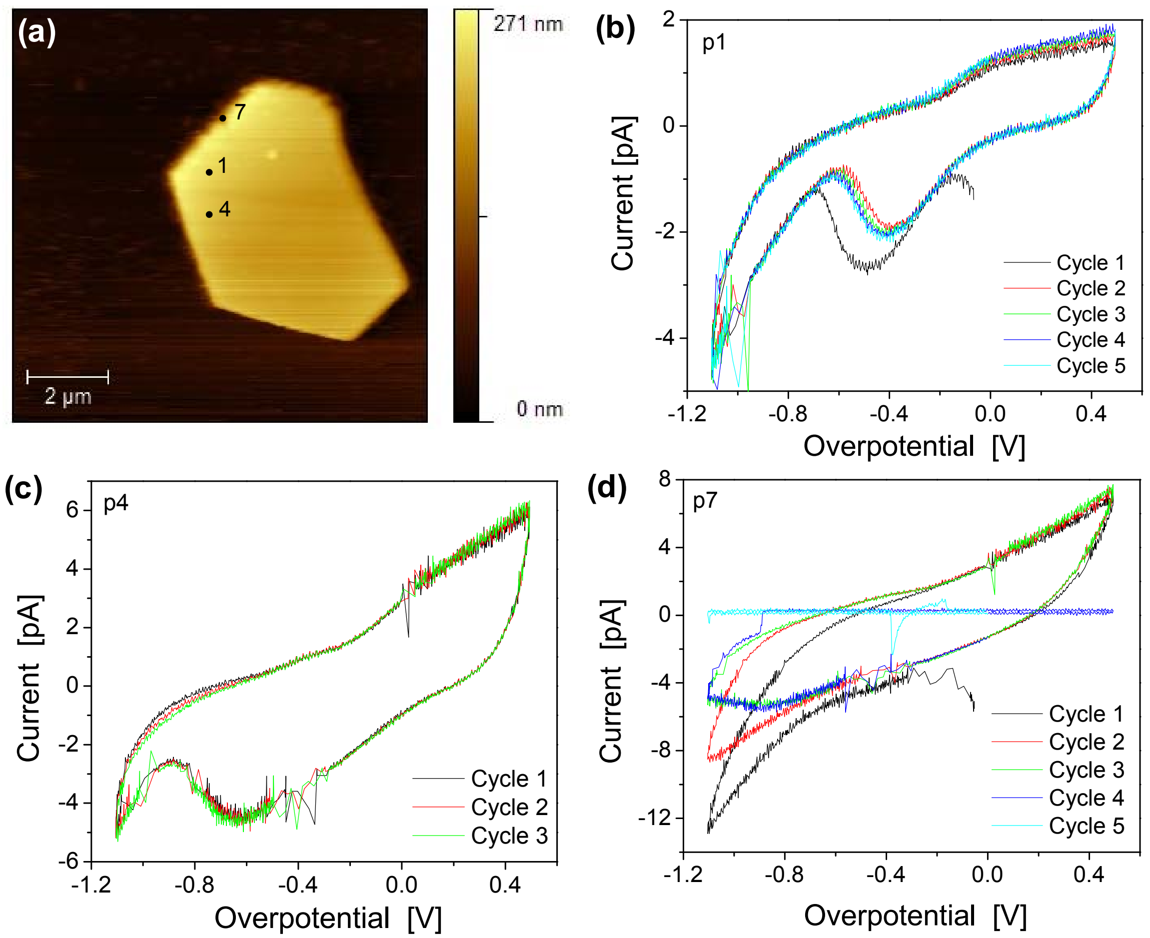

Figure G.5 Electrochemical AFM measurements at Pt | Ba$_{3-x}$K$_x$H$_x$(PO$_4$)$_2$: (a) A topographical AFM image of a Ba$_{3-x}$K$_x$H$_x$(PO$_4$)$_2$ platelet on a Pt-coated silicon wafer and corresponding cyclic voltammograms measured at positions 1, 4, 7 (b–d) for three or more consecutive cycles at 100 mV s^{-1}. Measurements were performed using a commercial Pt coated AFM probe with a spring constant of ~ 5 N m^{-1} at 175 ºC in air with ~ 0.03 atm H$_2$O. While (b) and (c) show reproducible voltammograms, (c) shows a slows a change in the current with cycle number.

To assess whether intermittent current measurements are a result of poor/intermittent contact of $Ba_{3-x}K_xH_x(PO_4)_2$ platelets with the Pt-coated Si substrate (i.e., counter electrode), a substrate with transferred $Ba_{3-x}K_xH_x(PO_4)_2$ platelets (i.e., Wafer 2 in Figure G.4(d–f)) was examined. Figure G.6 shows typical results from this type of sample. Similar to the voltammograms in Figure G.5d, the results reveal currents that vary with position on the $Ba_{3-x}K_xH_x(PO_4)_2$ and with time at the same position. Also evident in these measurements (and in others) is that increasing the temperature from 175 ºC (Figure G.5) to 220 ºC (Figure G.6) yielded no improvements in the electrochemical response. In addition, the detection of current occurs in a random fashion, indicating the degradation of the probe is not likely the problem, as this would yield currents which decrease with experimental time.

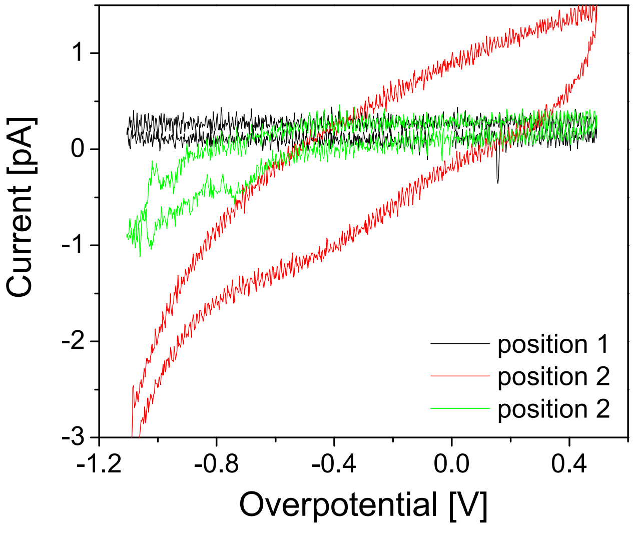

Figure G.6 Cyclic voltammograms collected at 220 ºC in synthetic air with ~ 0.03 atm H_2O for two different positions on a $Ba_{3-x}K_xH_x(PO_4)_2$ platelet, where the counter electrode Pt | $Ba_{3-x}K_xH_x(PO_4)_2$ interface was comprised of Pt sputtered directly onto $Ba_{3-x}K_xH_x(PO_4)_2$.

G.3.4 Troubleshooting

A short-circuit measurement was performed on a bare Pt-coated wafer using a used Pt-coated probe, specifically that used to acquire the results presented in Figure G.6. For comparison purposes, similar measurements were carried out using an Au-coated probe (Figure G.7). The short-circuit correction for the Pt | Pt interface is somewhat unexpected. While the currents are sufficiently high, the response is not ohmic as would be expected for a metal-metal contact. On the other hand, the Au-coated probe gives the expected ohmic response, indicating that the source of the non-ohmic response in the case of Pt is the probe rather than the substrate. Possible explanations for the non-ohmic response of Figure G.7a are the formation of an oxide layer or contamination of the Pt probe.

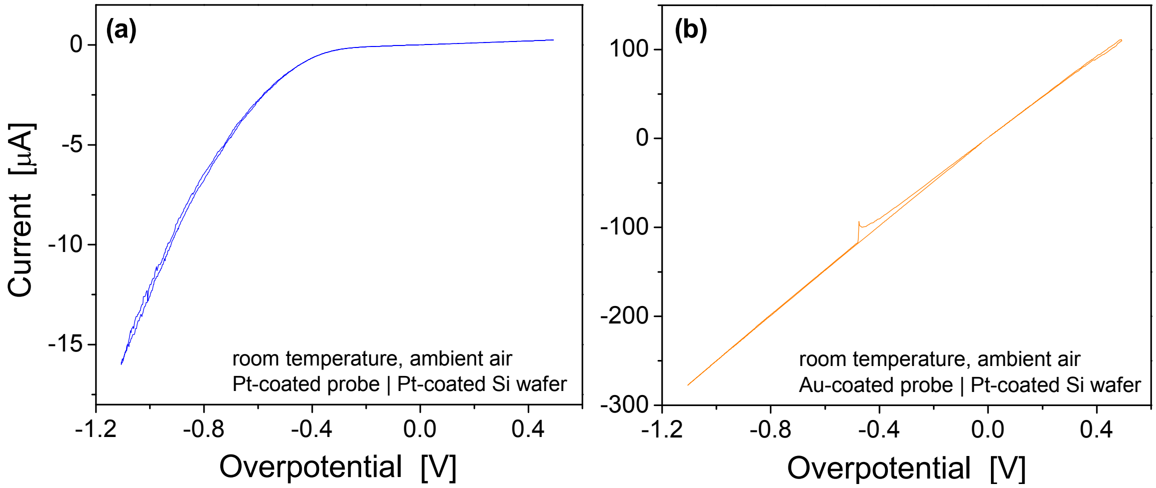

Figure G.7 Short-circuit measurements on Pt-coated silicon wafer at room temperature in ambient air using (a) a used Pt-coated probe from Figure G.5, and (b) a Au-coated probe for comparison.

The effect of residual organics/contaminants, either from the synthesis of $Ba_{3-x}K_xH_x(PO_4)_2$ or from the suspension in methanol was investigated. Figure G.8 shows Raman spectra collected for $Ba_{3-x}K_xH_x(PO_4)_2$ platelets on a Si wafer, as-deposited from methanol and after two 15-min intervals of oxygen plasma (100 W, 250 mTorr O_2). The spectra show shifts characteristic of the silicon substrate (~ 520 cm^{-1}) as well as for symmetric stretches for PO_4 groups.[113] Additionally, a shift at ~ 2900 cm^{-1}, attributed to the C-H stretch in organic compounds, indicates the presence of contaminants. However, the removal of such organics by oxygen plasma was not successful despite the relatively high plasma power and duration. Thus, it is unclear what the source of such organics are and its uniformity across the sample. As shown in the spectra, the presence of organics varies with the specific platelet examined. Specifically, after the second interval of plasma treatment (Figure G.8), the C-H stretch was present in the spectrum for one platelet but not another. Thus, without the capability in the AFM system to identify and target a specific platelet particle which we identified (via Raman spectroscopy) to show no organic signatures, it is presently not possible to use oxygen plasma cleaning to our advantage. Not surprisingly, the samples that were treated by oxygen plasma did not yield any improvements in the electrochemical response (not shown).

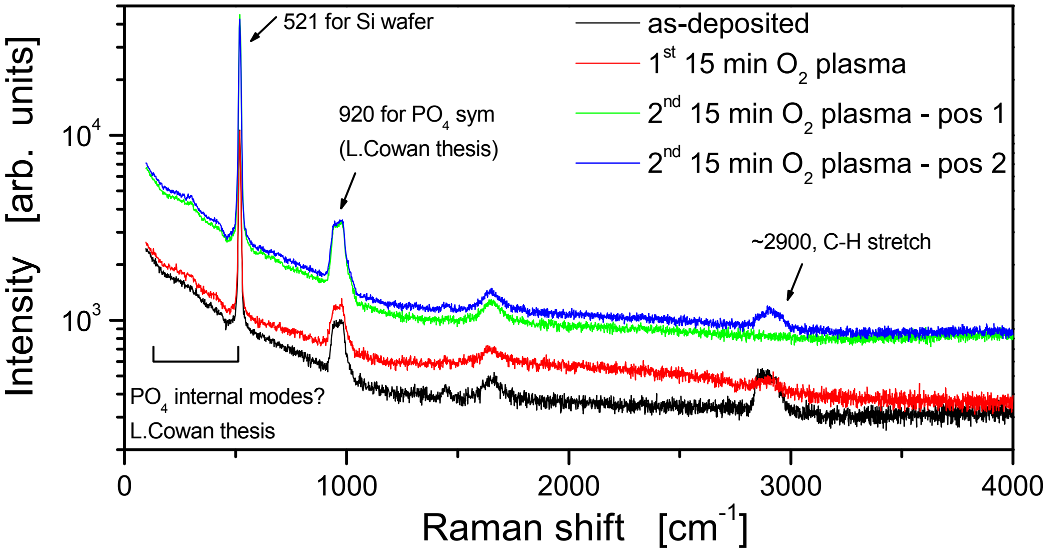

Figure G.8 Raman spectra collected for $Ba_{3-x}K_xH_x(PO_4)_2$ platelets deposited on bare a Si wafer showing shifts for organic compounds, in addition to those expected for $Ba_{3-x}K_xH_x(PO_4)_2$ and Si. Spectra were collected for as-deposited $Ba_{3-x}K_xH_x(PO_4)_2$ and after two 15-min intervals of oxygen plasma treatment, with spectra collected for two different platelets after the second interval of plasma treatment.

G.4 Recommendations for Future Studies

Various attempts to determine the source of intermittent currents measured in electrochemical AFM for the Pt | $Ba_{3-x}K_xH_x(PO_4)_2$ interface have been unsuccessful. Based on the observations made for the $Ba_{3-x}K_xH_x(PO_4)_2$ system thus far, several recommendations are proposed.

1) Determine the effect of contaminants from methanol used in the $Ba_{3-x}K_xH_x(PO_4)_2$ suspension by comparing the voltammograms measured by electrochemical AFM for a bare Pt-coated wafer, and that with methanol deposited on and evaporated from the wafer.

2) Employ Raman spectroscopy (or a similar tool) to determine the presence of contaminants in as-synthesized $Ba_{3-x}K_xH_x(PO_4)_2$ powders and after any subsequent processing steps.
3) $Ba_{3-x}K_xH_x(PO_4)_2$ has a trigonal structure, analogous to $Rb_3H(SeO_4)_2$ which is known to have anisotropic conductivity. By analogy to $Rb_3H(SeO_4)_2$, it is expected that the direction of higher proton conductivity in $Ba_{3-x}K_xH_x(PO_4)_2$ is in the plane of the platelet (Figure 1.4). Thus, while the platelet morphology of $Ba_{3-x}K_xH_x(PO_4)_2$ provides geometric advantages for minimizing ohmic losses, it may be worthwhile to consider synthesizing particles with different microstructures.
4) Eliminate possible wear on the probe. This can be done by using probes with low force constants, optimizing the deposition of $Ba_{3-x}K_xH_x(PO_4)_2$ platelets to obtain high densities on the substrate, and/or obtain an AFM with an optical microscope so that specific $Ba_{3-x}K_xH_x(PO_4)_2$ platelets can be located without repeated topography scans.

Appendix H Pd | $CsHSO_4$ by Atomic Force Microscopy

The palladium-platinum system has been observed to exhibit promising performance as a cathode for solid acid fuel cells.[3] Furthermore, as shown in Appendix D, palladium also displays promising activities for hydrogen electro-oxidation. In this section, we present preliminary results from electrochemical AFM studies of the Pd | $CsHSO_4$ interface to explore its electrocatalytic behavior compared to that for Pt | $CsHSO_4$ (Chapter 4). Although there has been evidence that reaction between Pd oxide and CsH_2PO_4 occurs at 240 ºC[3] (Appendix B), none was detected at 150 ºC, that is, at temperatures relevant for the study of $CsHSO_4$. Therefore, the Pd | $CsHSO_4$ system may be useful for further exploration of the variability of electrochemical kinetics and the correlation of key kinetic parameters, observed in Chapter 3 for Pt | $CsHSO_4$.

In order to make a reliable comparison between Pt and Pd, we examine the spatial variation of electrode kinetics at the Pd | $CsHSO_4$ interface, since it was shown in Chapter 4 that measurements at the nanoscale can vary dramatically across a given $CsHSO_4$ surface.

H.1 Experimental

Half-cells with Pt-based composite counter electrodes, identical to those used in Chapter 4, were employed for Pd studies. Environmental conditions used and electrochemical measurements performed were also the same. Since Pd-coated probes are not available commercially, bare Si-based probes were sputtered in-house with 15 nm of

Pd. (Cressington 208HR, ~ 15 mTorr Ar, 80 mA plasma current). Table H.1 shows the probes used to collect the data presented in this section. To ensure that the electrochemical response of the metal | $CsHSO_4$ interface does not vary with the metal film deposition method, Pt was also sputtered onto Si-based probes using the same procedure as was used for Pd. Qualitative agreement of the DC and AC measurements between the sputtered and commercial Pt probes would indicate that Pd studies can be reliably compared to previous results for Pt.

Table H.1 Description of AFM probes employed for comparing Pd | $CsHSO_4$ and Pt | $CsHSO_4$.

Probe	**Probe coating**	**Cantilever Type**	**Nominal spring constant, *k* [N m^{-1}]**	**Metal deposition**
1	Platinum	rectangular	5	Commercial, from Chapter 4
2	Platinum	triangular	0.5	Sputtered in-house
3	Palladium	rectangular	5	Sputtered in-house
4	Palladium	triangular	0.5	Sputtered in-house

H.2 Results and Discussion

H.2.1 Oxygen Electro-reduction

Figure H.1a shows a typical cyclic voltammetry response for the nano-Pd | $CsHSO_4$ system obtained using Probe 3 in Table H.1. The transient effects, most evident at high scan rates, can be readily distinguished from Faradaic currents. Two reduction peaks are visible at ~ –0.4 and –0.7 V (with an onset voltage for the former being ~ –0.3 V), and a smaller, relative broad oxidation peak occurs on the return sweep at ~ –0.4 V. These are overlaid with an oxygen reduction current that increase dramatically at overpotentials beyond –0.8 V. Impedance spectra collected as a function of overpotential (Figure H.1b) show two convoluted arcs, both of which decrease in size at higher (negative) overpotentials.

From thermodynamic data, the potential for reduction of PdO is –0.36 V at 150 ºC in 0.21 atm O_2, whereas those for $Pd(OH)_2$ and $Pd(OH)_4$ (for which thermodynamic data was available) are –0.21 and –0.11 V. The onset voltage of –0.3 V for the first reduction peak appears to be consistent with reduction of oxidized Pd. However, the identities of the remaining peaks are unclear. We proceed with analysis of oxygen electro-reduction kinetics based on the observation that the oxygen reduction currents are stable over many voltammetry cycles, and thus the processes which generate the unknown transient features do not irreversibly degrade the Pd film or its activity.

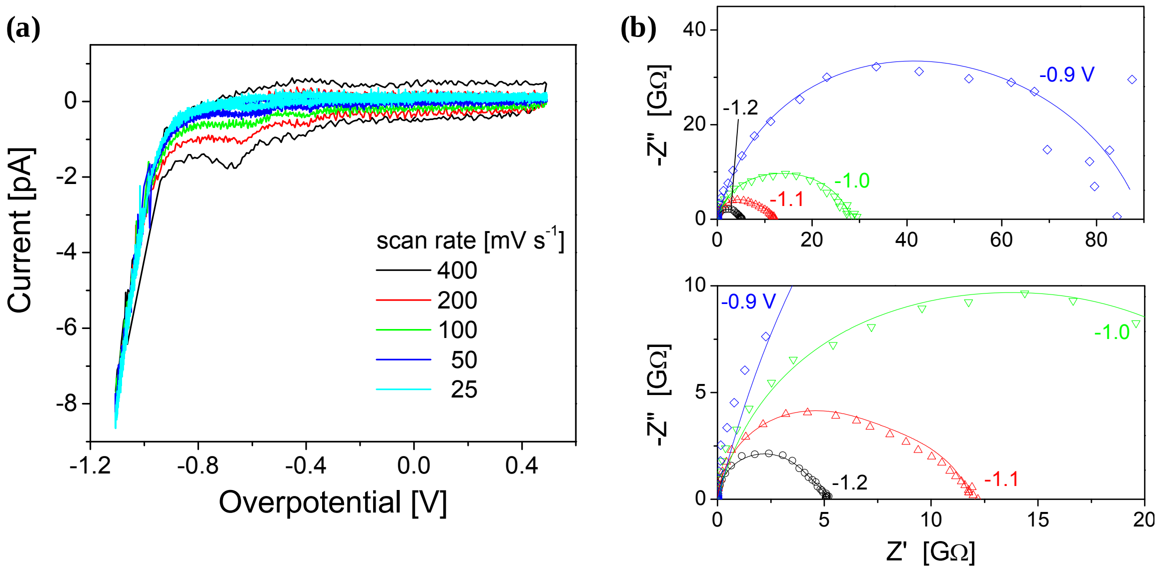

Figure H.1 Electrochemical response of the Pd | $CsHSO_4$ system at ~ 150 ºC in air with ~ 0.03 atm H_2O: (a) cyclic voltammograms for Pd | $CsHSO_4$ measured as a function of scan rate and (b) impedance spectra collected as a function of overpotential. (Probe 3 in Table H.1)

The resistances of the high and low-frequency processes, plotted on a semi-logarithmic plot against overpotential (Figure H.2a), fall along lines with finite slopes, indicating that both processes depend exponentially on the overpotential. The resistance of the low-frequency process, R_{LF}, is greater than that for the high-frequency process, R_{HF}, for overpotentials below ~ –1 V and dominates the total resistance at overpotentials below ~ –0.9 V. Because the low-frequency process depends more strongly on overpotential, the total resistance follows R_{LF} at low overpotentials but deviates at high overpotentials due to R_{HF}. This behavior is qualitatively consistent with DC data obtained from cyclic voltammetry, plotted in Tafel form (Figure H.2b).

The behavior of Pd | $CsHSO_4$ differs slightly from that of Pt | $CsHSO_4$ presented in Chapter 4. While the low-frequency arc appears to behave similarly, that is, R_{LF} depends exponentially on overpotential, the high-frequency process, in the case of Pd, also depends on overpotential, albeit to a lesser extent. (As shown in Figure H.2a, the low-frequency resistance of Pd spans three orders of magnitude across 500 mV, while the high-frequency resistance spans one order.) One might be tempted to attribute the observed dependence of the high-frequency process to error resulting from fitting the impedance spectra, but direct examination of the impedance response (Figure H.1b) indicates that both arcs are indeed changing with overpotential.

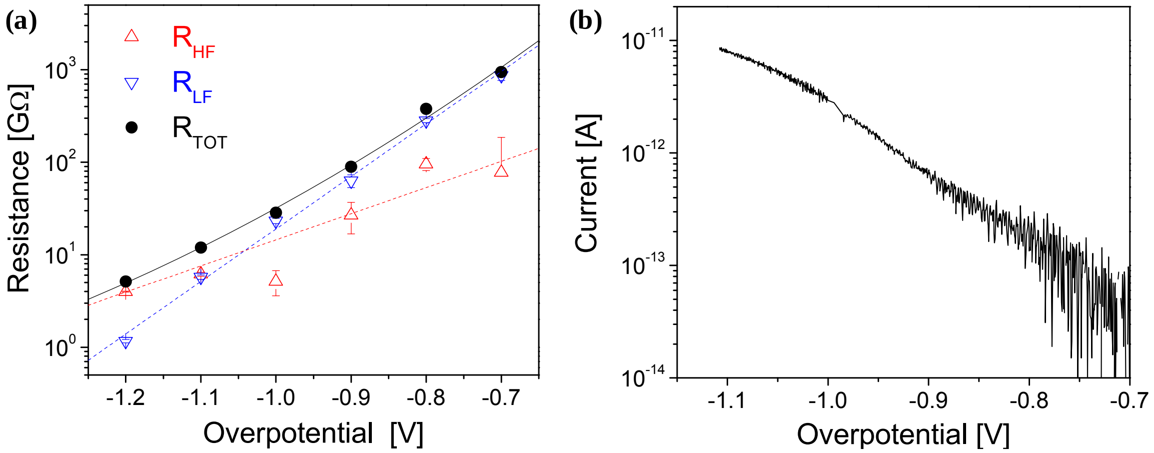

Figure H.2 (a) Resistances of the high-frequency (R_{HF}) and low-frequency (R_{LF}) electrode processes, and their sum, plotted as a function of overpotential. Electrode resistances were extracted from fitting the Nyquist spectra shown in Figure H.1b. (b) Tafel plot for the Pd | $CsHSO_4$ system acquired from the cathodic branch (return sweep) of a cyclic voltammogram collected at 25 mV s^{-1}.

Tafel plots for the Pd | $CsHSO_4$ system as a function of position across the $CsHSO_4$ surface reveal a linear regime at overpotentials below –1 V. At high overpotential, the Tafel plot changes behavior; as the overpotential becomes larger, the slope of Tafel plot increases for some measurements but decreases or remains constant for others. The source of this variation is presently unknown.

Based on results from Figure H.1a and Figure H.2a, we can set the range for Tafel analysis of R_{LF} to be approximately between –1 and –0.7 V, the former being the overpotential beyond which R_{HF} dominates the total response and the latter being the overpotential at which transient effects start to surface. The exchange current, i_0, and exchange coefficient, α, were extracted by fitting the Tafel equation (Equation 4.6) to the plots in this overpotential window. Despite uncertainties in both the electrochemical response at high overpotential as well as the transient behavior of the Pd | $CsHSO_4$ system, the extracted Tafel parameters appear be correlated (Figure H.4). Moreover, the slope of the i_0-α correlation agrees reasonably well with that for the Pt | $CsHSO_4$ system

(Chapter 4) and for data collected using Probes 2 and 4 in Table H.1 (raw data not shown).

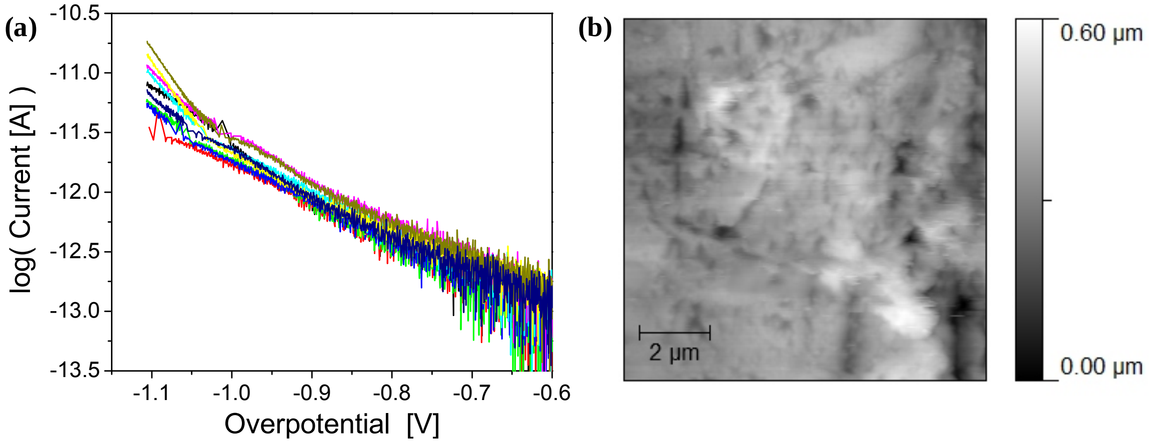

Figure H.3 (a) Select Tafel plots of the cathodic branches (return sweep) of cyclic voltammograms collected at 25 mV s^{-1} at various positions across (b) a 5 × 5 μm^2 $CsHSO_4$ surface.

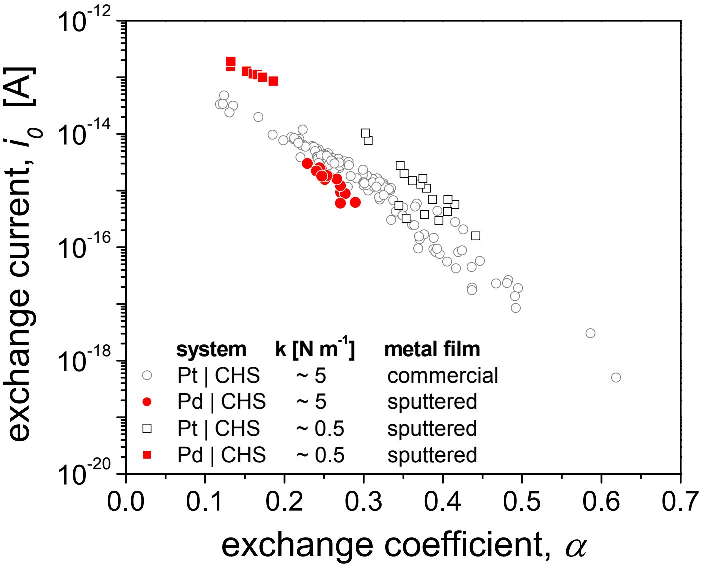

Figure H.4 Exchange current (log scale) plotted against exchange coefficient comparing four metal | $CsHSO_4$ systems using probes shown in Table H.1. CHS = $CsHSO_4$

It is interesting to note that the currents for Probes 2 and 4 ($k = 0.5$ N m^{-1}) have noticeably higher currents, by approximately half an order of magnitude. This is most likely due to the higher contact area between the probe and $CsHSO_4$ (which results in a higher overall current passing through the probe | $CsHSO_4$ interface). AFM topography images of the surface during testing, Figure H.5(a–b), reveal that these probes can severely damage the surface of the sample. It is unclear why these probes exhibited such high forces on the sample, since their nominal spring constants are low compared to those for Probes 1 and 3. Besides the triangular shape of the cantilevers for Probes 2 and 4, the only other difference is their construction from silicon nitride which is a harder material than silicon.

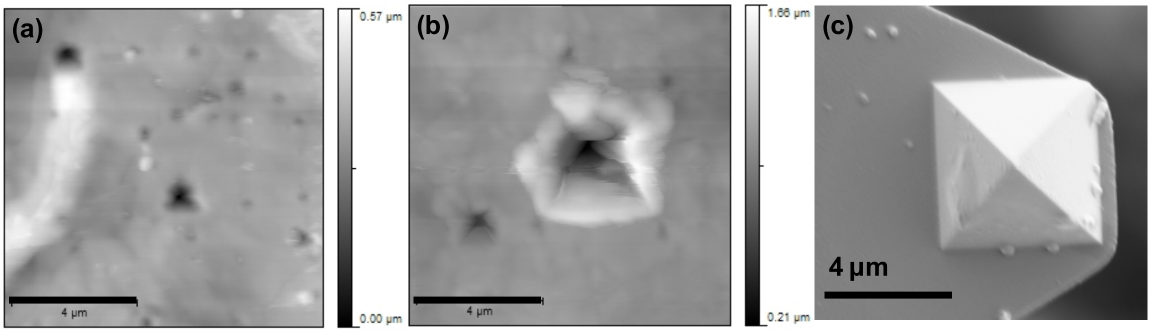

Figure H.5 (a–b) AFM images of a $CsHSO_4$ polycrystalline sample damaged by AFM probes, (Probes 2 and 4 in Table H.1) and (c) SEM micrograph of a probe for comparison.

H.2.2 Transient Behavior of Pd | $CsHSO_4$

We present here the cyclic voltammetry response for the Pd | $CsHSO_4$ collected using Probe 4 (Figure H.6). (This data set does not correspond to data shown in Figure H.4.) Due to the large Pd | $CsHSO_4$ contact area, high currents were measured, enabling exploration of the transient behavior which would otherwise be difficult to capture for the system shown in Figure H.1a. Clearly visible in the voltammogram are two reduction peaks and two oxidation peaks. The former, with peak positions of ~ –0.3 V and –0.4 to

–0.6 V, are denoted Peaks 1 and 2, respectively, and the latter, with peak positions of –0.35 to –0.4 V and –0.05 to 0.05 (depending on the scan rate), are denoted Peaks 3 and 4, respectively. Oxidation peaks (3 and 4) are notably broader than reduction peaks (1 and 2), indicating slower kinetics. The existence of two peaks is consistent with previous Pd measurements (Figure H.1a), although at lower scan rates, a third reduction feature is visible (denoted with asterisks), with a peak position of –0.5 V at a scan rate of 25 mV s^{-1}.

The relative kinetics of the processes can be determined by the shift in the peak position with scan rate. As the scan rate is increased, the peak position of Peak 1 does not vary significantly whereas that for Peak 2 shifts to higher (negative) overpotentials, indicating that the latter process cannot "keep up" with the high scan rates.

The onset voltage of Peak 1 can be estimated at –0.2 V, notably lower than the value expected for the onset of PdO reduction, –0.36 V, but comparable to that for $Pd(OH)_2$, –0.21 V.

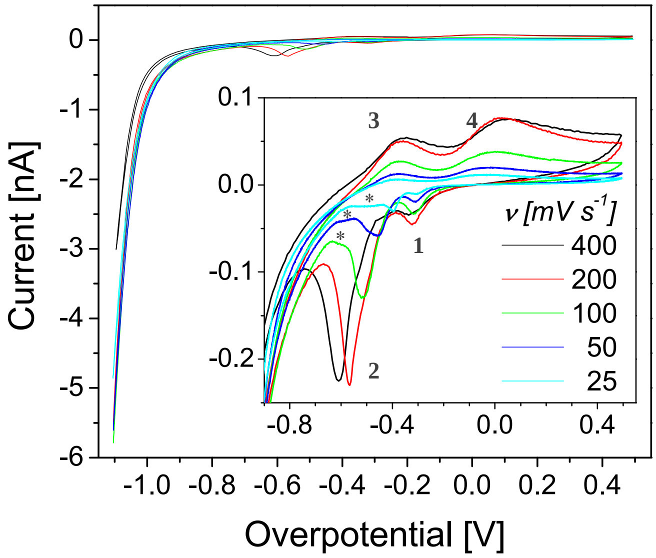

Figure H.6 Cyclic voltammograms for Pd | $CsHSO_4$, collected at 150 °C in air with ~ 0.03 atm H_2O, showing the transient behavior.

H.2.3 Palladium Oxidation

We examined the reduction behavior of Peaks 1 and 2 as a function of oxidation time in air at applied voltages of 0 V and 0.5 V, conditions that allow for chemical and electrochemical oxidation of Pd, respectively (Figure H.7). In the case of chemical oxidation (dwelling with no voltage applied), the peak positions for both Peaks 1 and 2 shifted to larger overpotentials with dwell time, with the two peaks becoming completely convoluted for a 10 min dwell time (Figure H.7). The steady-state current at –1 V increases with dwell time, with some scatter. In the case of electrochemical oxidation (0.5 V applied voltage), the current-voltage curves are much less noisy, with the current at –1 V clearly increasing with dwell time (Figure H.7b). Peak 1 shrinks with dwell time, disappearing completely after 10 min, while Peak 2 increases, with the peak position shifting to higher overpotentials. The disappearance of Peak 1 and the increase in the area of Peak 2 suggests that electrochemical oxidation favors the formation of species which are subsequently reduced via Peak 2. This is also true in the case of chemical oxidation but to a much lesser extent, as indicated by the presence of Peak 1 even after 5 min dwell time (Figure H.7b). It is important to keep in mind that these peaks might not necessarily correspond to oxides of Pd. For example, solid products which could result from reaction between Pd and $CsHSO_4$ at oxidative conditions would be electro-reduced once sufficiently negative overpotentials are applied. Another process which could generate transient features in the voltammograms is the insertion of hydrogen into Pd, that is, under reducing currents, protons from $CsHSO_4$ are reduced by electrons to hydrogen atoms which are then inserted into Pd. This insertion/charging process could surface as an peak in cyclic voltammetry as interstitial sites in Pd are being filled.

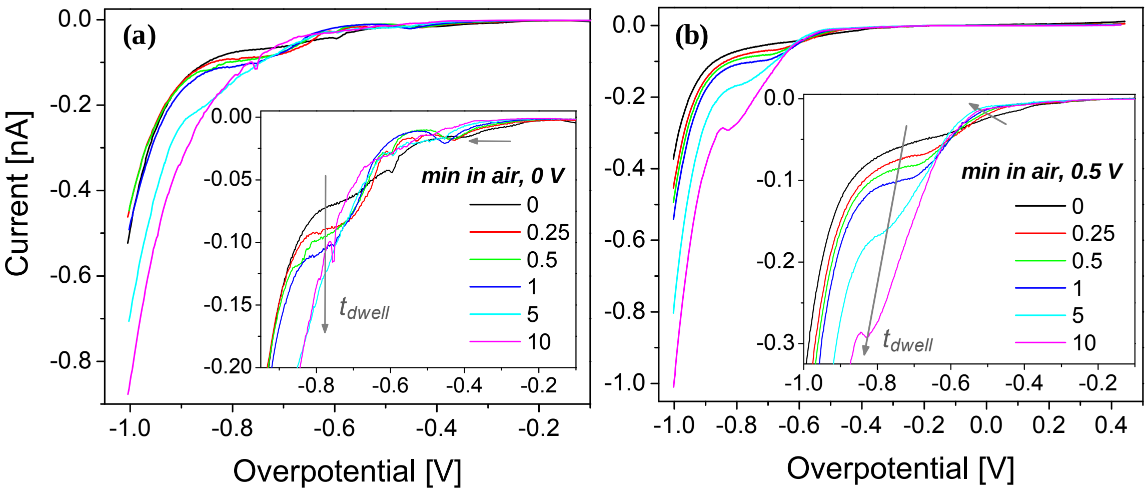

Figure H.7 Behavior of reduction peaks in Pd | CsHSO$_4$ (ν = 100 mV s^{-1}) collected at 150 ºC in flowing air with ~ 0.03 atm H$_2$O, after dwelling for various times (a) with no voltage applied, for chemical oxidation of Pd and (b) 0.5 V applied, for electrochemical oxidation of Pd.

H.2.4 Stability of Pd | CsHSO$_4$

Despite electrochemical characterization of Pd | CsHSO$_4$ at ~ 150 ºC for several hours, during which cyclic voltammograms (between –1.1 and 0.5 V) were routinely collected and oxidation tests performed, the steady-state electrochemical currents did not appear to degrade significantly with time. As shown in (Figure H.8a) for data collected at various positions across the CsHSO$_4$ surface, the current at –1.1 V fluctuated randomly with time (and position) while that at –0.8 V increases slightly with time (and position). The latter can also be seen in Figure H.8b for three select voltammograms collected at arbitrary positions/times; the increase in steady-state current appears to be correlated with the transient features which also increase in size. This behavior generally implies that the contact area has increased. In contrast to the behavior at –1.1 V, the increase in current at –0.8 V with time outweighs any changes in current due to spatial heterogeneity.

The observation that the currents do not degrade significant is an indication that Pd (oxide) does not react with $CsHSO_4$ in a way that is detrimental to the oxygen reduction kinetics. Although Pd (presumably the oxide form) was observed to react with CsH_2PO_4 at temperatures near ~ 240 ºC, reaction at ~ 150 ºC was not observed even after 48 h (Appendix B). This is consistent with, though not necessarily evidence of, the observed stability of the Pd | $CsHSO_4$ system.

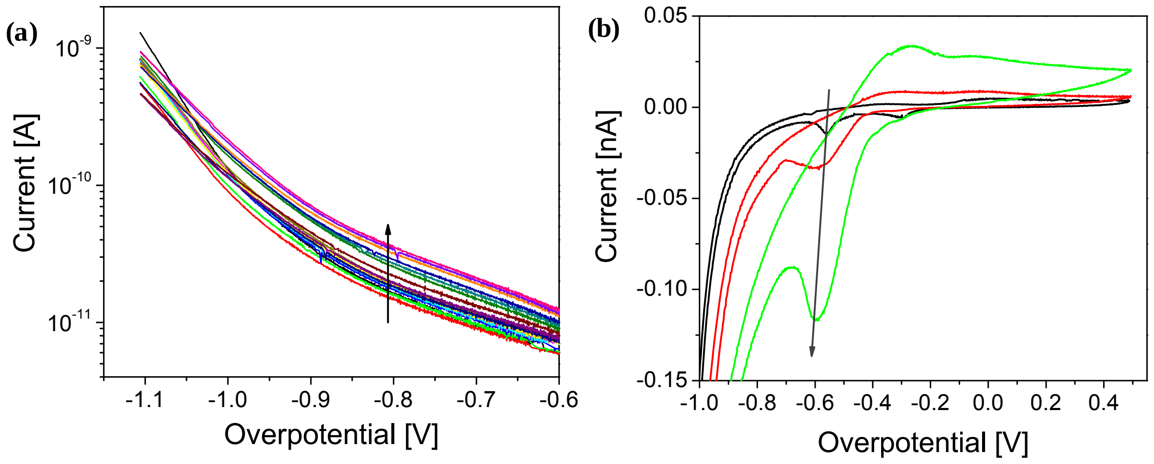

Figure H.8 Spatial variation of Pd | $CsHSO_4$ at $T = 150$ ºC in air with ~ 0.03 atm H_2O: (a) Tafel behavior as a function of position (and time), taken from voltammograms collected at 25 mV s^{-1} and (b) three voltammograms (100 mV s^{-1}) collected at beginning, middle and end of the spatial variation studies in (a).

H.3 Summary

1) A correlation of i_0 and α was observed for Pd, using probes similar to those used for the Pt | $CsHSO_4$ system presented in Chapter 4.
2) Despite having nominally low spring constants, triangular-type silicon nitride probes appeared to cause more damage to $CsHSO_4$ than rectangular-type silicon probes. In general, probes of the same design should be used when comparing different metal coatings.

3) Pd | $CsHSO_4$ displayed two primary transient features for which both the reduction and corresponding oxidation peaks were visible. These peaks may be related to oxide formation but are not necessarily, themselves representative of PdO or related oxides. This is because any charging/discharging process in series with an electrochemical step can manifest itself as a peak in the voltammogram.
4) Pd does not appear to react significantly (if at all) with $CsHSO_4$.
5) Across five different Pd | $CsHSO_4$ (not all presented in this section), we frequently observed an increase in the Tafel slope at high overpotentials. It is unclear whether the intermediate-to-high overpotential regime has some contribution from kinetically slow transient processes, even at a 25 mV s^{-1}, which would generate artifacts in the Tafel plot.

Appendix I Crystallographic Compatibility in $Cs_{1-x}Rb_xH_2PO_4$

I.1 Visualization of the Cubic-to-Monoclinic Transformation in CsH_2PO_4

The cubic-to-monoclinic transformation for CsH_2PO_4 is depicted in Figure I.1. From examination of the lattice parameters (Table I.1 and Table I.2) and the geometry of the two unit cells, the relationship between the two structures can be determined as follows. A tetragonal cell is constructed by connecting the face diagonals of four adjacent cubic unit cells (Figure I.1a). A shift in this cell in the –3 direction (Figure I.1b), while not necessary for this analysis, aids with visualization of atom movement during the transformation. The tetragonal cell is subsequently stretched unequally along its three axes (not shown) and the Cs atoms shifted to keep two units of CsH_2PO_4 in the cell (Figure I.1c). Finally, the top face is sheared along the *c* direction to increase the angle β from 90º to 107.7º (Figure I.1d). Appropriate shifts of the atoms result in the final monoclinic structure.

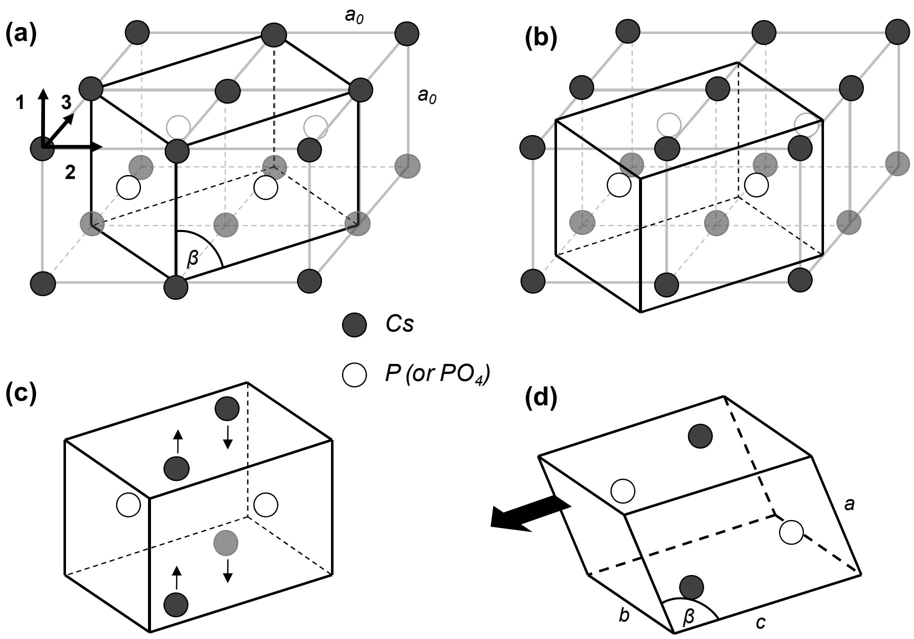

Figure I.1 Visualization of the phase transformation in CsH_2PO_4 with only P and O atoms drawn. The contents of a monoclinic cell can be obtained from (a–b) a shifted tetragonal sub-lattice obtained from four cubic unit cells. (c) The Cs cation is shifted off the *bc* planes to keep two Cs atoms per lattice, and (c–d) the *bc* plane is sheared along the *c* direction to obtain the *β* angle.

Table I.1 Lattice parameters and atomic positions for the low-temperature monoclinic structure of CsH_2PO_4.[68]

$P2_1/m$ (#11)

$a = 4.8788$ Å, $b = 6.3848$ Å, $c = 7.9091$ Å, $\alpha = \gamma = 90°$, $\beta = 107.71°$

Atom	*Multiplicity*	*Occupancy*	*x*	*y*	*z*
Cs	2	1	0.0351(1)	0.25	0.26564(4)
P	2	1	0.5290(3)	0.75	0.2370(2)
O(1)	2	1	0.3883(7)	0.75	0.3912(5)
O(2)	2	1	0.8461(9)	0.75	0.3228(6)
O(3)	4	1	0.4188(7)	0.5528(5)	0.1270(4)
H(1)	1	1	0.195	0.75	0.348
H(2)	1	1	0.5	0.5	0

Table I.2 Lattice parameters and atomic positions for the high-temperature cubic structure of CsH_2PO_4.[117]

Pm–3m (#221)

$a_0 = 4.9549(4)$ Å, $\alpha = \beta = \gamma = 90°$

Atom	*Multiplicity*	*Occupancy*	*x*	*y*	*z*
Cs	1	1	0	0	0
P	1	1	0.5	0.5	0.5
O	24	1/6	0.322	0.248	0.5
H	48	1/24	—	—	—

I.2 Calculation of Transformation Matrix

This section follows procedures outlined by Bhattacharya[115] and details on how to compute the transformation matrix described by Equation 5.2. For some transformations (including that for CsH_2PO_4), the homogeneous deformation of the lattice vectors to transform between the austenite and martensite phases does not yield a transformation that is symmetric. In this case, the direct mapping of the lattice vectors of the cubic and monoclinic cases is

$$\mathbf{e}_\mathbf{i}^\mathbf{m} = \mathbf{T}_\mathbf{1}\mathbf{e}_\mathbf{i}^\mathbf{a} \tag{I.1}$$

where $\mathbf{e}_\mathbf{i}^\mathbf{a}$ and $\mathbf{e}_\mathbf{i}^\mathbf{m}$ are given by Equation 5.3 and 5.4, respectively. $\mathbf{T_1}$, the homogeneous deformation, can be computed readily by matrix algebra.

$$\mathbf{T}_1 = \begin{pmatrix} \frac{a}{a_0} & \frac{c}{2a_0}\cos\beta & \frac{c}{2a_0}\cos\beta \\ 0 & \frac{c\sin\beta + b}{2a_0\sqrt{2}} & \frac{c\sin\beta - b}{2a_0\sqrt{2}} \\ 0 & \frac{c\sin\beta - b}{2a_0\sqrt{2}} & \frac{c\sin\beta + b}{2a_0\sqrt{2}} \end{pmatrix} \tag{I.2}$$

By convention, the definition of the transformation matrix should be positive-definite and symmetric, and therefore, the deformation $\mathbf{T_1}$ is modified to obtain the symmetric, positive-definite matrix $\mathbf{U_1}$. To obtain $\mathbf{U_1}$, $\mathbf{T_1} = \mathbf{QU_1}$ is decomposed such that $\mathbf{Q}$ is a rotation; because of frame-indifference, a rotation leaves the state of the lattice unchanged. The procedure for computing $\mathbf{U_1}$ is:

1) Find the matrix, $\mathbf{C} = \mathbf{T}_\mathbf{1}^\mathbf{T}\mathbf{T}_\mathbf{1}$. $\mathbf{C}$ is a positive-definite matrix.
2) Compute the eigenvalues $\{\gamma_1, \gamma_2, \gamma_3\}$ and the eigenvectors $\{\mathbf{u}_1, \mathbf{u}_2, \mathbf{u}_3\}$ of $\mathbf{C}$.

3) Take the positive root of each eigenvalue, $\mu_i = \sqrt{\gamma_i}$ for i = 1, 2, 3. Note γ_i is positive since **C** is a positive-definite matrix.

4) The Bain matrix, $\mathbf{U_1}$, with eigenvalues $\{\mu_1,\ \mu_2,\ \mu_3\}$ and eigenvectors $\{\mathbf{u_1}, \mathbf{u_2}, \mathbf{u_3}\}$, is given by:

$$\mathbf{U_1} = \mu_1 \mathbf{u_1} \otimes \mathbf{u_1} + \mu_2 \mathbf{u_2} \otimes \mathbf{u_2} + \mu_3 \mathbf{u_3} \otimes \mathbf{u_3} \tag{I.3}$$

Once $\mathbf{U}_1$ is known, all other variants can be obtained by applying the rotations of the cubic austenite lattice to this matrix. Variants, $\mathbf{U}_1$, $\mathbf{U}_2$, …, $\mathbf{U}_\mathrm{N}$ have the form

$$\mathbf{U_j} = \mathbf{R^T U_1 R} \tag{I.4}$$

where **R** is a rotation in the point group of the austenite. The relative symmetries of the austenite and martensite phases, some rotations of $\mathbf{U_1}$ will not give a unique variant, and precisely *N* distinct variants will exist, where *N* is given in Equation 5.1.

I.3 Calculation of Compatible Variant Pairs: Twinning Modes

In this section, we present a calculation of the twinning modes in CsH_2PO_4 which can occur on cooling from the cubic phase. We assume a simple microstructure comprised of one type of twin, that is, there exists no special microstructures such as twins within twins. To calculate the twinning modes of a given transformation, crystallographically compatible variants are first identified. Figure I.2 shows a schematic diagram of twins formed between a pair of variants $\mathbf{U_j}$ and $\mathbf{U_i}$. $\mathbf{U_i}$ and $\mathbf{U_j}$ can form a twin if they satisfy the twinning equation

$$\mathbf{QU_i} - \mathbf{U_j} = \mathbf{a} \otimes \mathbf{n} \tag{I.5}$$

for some rotation **Q** and unit vector **n** normal to the twinning interface. The twinning equation is a statement of the kinematic compatibility condition which requires the existence of an invariant plane, described by **n**, at the interface between two regions that have undergone continuous deformation.

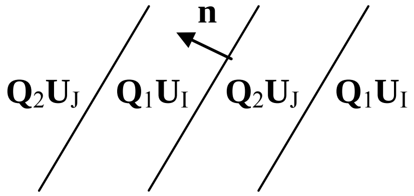

Figure I.2 Parallel twins separating two alternating variants, $\mathbf{U_J}$ and $\mathbf{U_I}$. $\mathbf{Q_1}$ and $\mathbf{Q_2}$ denote rotations.

The twinning equation (I.5) has two solutions if Equation (I.4) is satisfied for some 180º rotation $\mathbf{R} = -\mathbf{I} + 2\mathbf{v} \otimes \mathbf{v}$ about unit vector v:

$$\mathbf{a} = 2\left(\frac{\mathbf{U}_j^{-T}\mathbf{v}}{\left|\mathbf{U}_j^{-T}\mathbf{v}\right|^2} - \mathbf{U}_j\mathbf{v} \right), \qquad \mathbf{n} = \mathbf{v} \tag{I.6}$$

$$\mathbf{a} = \rho\mathbf{U}_j\mathbf{v}, \qquad \mathbf{n} = \frac{2}{\rho}\left(\mathbf{v} - \frac{\mathbf{U}_j^T\mathbf{U}_j\mathbf{v}}{\left|\mathbf{U}_j\mathbf{v}\right|^2} \right) \tag{I.7}$$

where ρ is non-zero and chosen such that $|\mathbf{n}| = 1$. The solution given by Equation (I.6) describes a Type I twin (i.e., the twinning plan is the plane of symmetry in the austenite), whereas the solution given by Equation (I.7) describes a Type II twin (i.e., the direction of shear is the direction of symmetry in the austenite). In the case where there are two distinct 180° rotations, $\mathbf{R_1}$ and $\mathbf{R_2}$, which satisfy Equation (I.4) for the same variant pair, Equations (I.6) and (I.7) yield two distinct solutions, each of which can be described as

Type I and Type II twins. (Specifically, the Type I solution using $\mathbf{R_1}$ corresponds to the Type II solution using $\mathbf{R_2}$ and vice versa.) These are called Compound twins.

If Equation (I.4) cannot be satisfied for a pair of variants and a two-fold rotation, it is necessary to calculate matrix $\mathbf{D} = \mathbf{U_J^{-T} U_I^T U_I U_J^{-1}}$. If $\mathbf{D}$ is the identity matrix, then the twinning equation has no solution. Otherwise, the eigenvalues of $\mathbf{D}$, $\{\lambda_1,\ \lambda_2,\ \lambda_3\}$, corresponding to eigenvectors, $\{\mathbf{e_1},\ \mathbf{e_2},\ \mathbf{e_3}\}$, must satisfy

$$\lambda_1 \le 1, \quad \lambda_2 = 1, \quad \lambda_3 \ge 1 \tag{I.8}$$

If Equation (I.8) holds, then the two solutions to the twinning equation are given by

$$\mathbf{a} = \rho\left(\sqrt{\frac{\lambda_3(1-\lambda_1)}{\lambda_3-\lambda_1}}\mathbf{e_1} + \kappa\sqrt{\frac{\lambda_1(\lambda_3-1)}{\lambda_3-\lambda_1}}\mathbf{e_3}\right) \tag{I.9}$$

$$\mathbf{n} = \frac{\sqrt{\lambda_3}-\sqrt{\lambda_1}}{\rho\sqrt{\lambda_3-\lambda_1}}\left(-\sqrt{1-\lambda_1}\,\mathbf{U_J^T e_1} + \kappa\sqrt{\lambda_3-1}\,\mathbf{U_J^T e_3}\right) \tag{I.10}$$

where $\kappa = \pm 1$, and ρ is non-zero and chosen such that $|\mathbf{n}| = 1$. As with Equations (I.6) and (I.7) two solutions (one for $\kappa = 1$ and one for $\kappa = -1$) are expected.

I.4 Calculation of the Austenite-Martensite Interface

Figure I.3 shows a schematic diagram of a simple austenite-martensite interface which is formed between the pure austenite phase and a twinned microstructure of two variants.

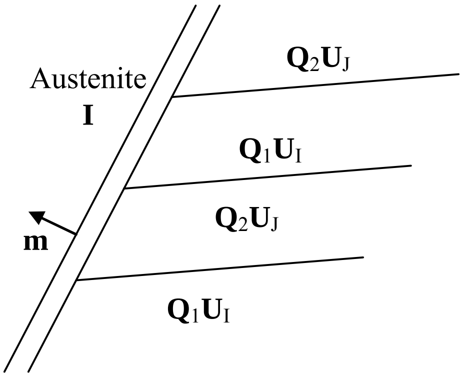

Figure I.3 Schematic of the interface between the austenite and two variants of martensite. **m** is the normal vector to the interface.

The interface is defined by the solution to both the twinning equation (I.5) *and* the austenite-martensite interface equation:

$$\mathbf{Q}'\left(\lambda\mathbf{Q}\mathbf{U}_{\mathbf{j}}+(1-\lambda)\mathbf{U}_{\mathbf{i}}\right)=\mathbf{I}+\mathbf{b}\otimes\mathbf{m} \tag{I.11}$$

where λ is some scalar satisfying $0 \le \lambda \le 1$ and **m** is the unit vector normal to the austenite-martensite interface. Once a solution to Equation (I.5) for matrix $\mathbf{U}_\mathbf{i}$ is found — given by either Equations (I.6)–(I.7) and/or (I.9)–(I.10) — the existence of a solution to Equation (I.11) is determined by the values of δ and η.

$$\delta=\mathbf{a}\cdot\mathbf{U}_{\mathbf{i}}\left(\mathbf{U}_{\mathbf{i}}^{2}-\mathbf{I}\right)^{-1}\mathbf{n} \qquad \text{and} \qquad \eta=\operatorname{tr}(\mathbf{U}_{\mathbf{i}}^{2})-\det(\mathbf{U}_{\mathbf{i}}^{2})-2+\frac{|\mathbf{a}|^{2}}{2\delta} \tag{I.12}$$

An austenite-martensite interface exists if and only if

$$\delta\le-2 \qquad \text{and} \qquad \eta\ge 0 \tag{I.13}$$

If the conditions in Equations (I.13) are satisfied, the interface is described by

$$\mathbf{b}=\rho\left(\sqrt{\frac{\lambda_3(1-\lambda_1)}{\lambda_3-\lambda_1}}\mathbf{e}_1+\kappa\sqrt{\frac{\lambda_1(\lambda_3-1)}{\lambda_3-\lambda_1}}\mathbf{e}_3\right) \tag{I.14}$$

$$\mathbf{m} = \frac{\sqrt{\lambda_3} - \sqrt{\lambda_1}}{\rho\sqrt{\lambda_3 - \lambda_1}}\left(-\sqrt{1-\lambda_1}\,\mathbf{e_1} + \kappa\sqrt{\lambda_3 - 1}\,\mathbf{e_3}\right) \tag{I.15}$$

where $\kappa = \pm 1$, ρ is chosen such that $|\mathbf{m}| = 1$, and $\lambda_1 \leq \lambda_2 \leq \lambda_3$ are the eigenvalues corresponding to the eigenvectors, $\{\mathbf{e_1}, \mathbf{e_2}, \mathbf{e_3}\}$, of matrix **E** defined as

$$\mathbf{E} = (\mathbf{U_i} + \lambda\mathbf{n} \otimes \mathbf{a})(\mathbf{U_i} + \lambda\mathbf{a} \otimes \mathbf{n}) \tag{I.16}$$

and

$$\lambda = \frac{1}{2}\left(1 - \sqrt{1 + \frac{2}{\delta}}\right) \tag{I.17}$$

If $\delta < -2$, another pair of solutions is obtained by replacing λ in Equation (I.16) with $(1 - \lambda)$. For each allowable variant pair, two types of twins can form, each of which has four possible solutions for the austenite-martensite interface. Therefore, there are up to eight solutions expected for a given variant pair.

I.5 Results for CsH_2PO_4

All calculations shown in this section are based on lattice parameters shown in Table I.1 and Table I.2. The twelve variants of martensite, obtained using Equation (I.4) are shown in Table I.3. Each variant was obtained by a rotation of $\mathbf{U_1}$ by the angle and about the axis indicated. Note that the choice of symmetry operation on $\mathbf{U_1}$ is not unique, as different rotations applied to $\mathbf{U_1}$ can yield the same result.

Table I.3 Martensite variants for the cubic-to-monoclinic transition of CsH_2PO_4 and the corresponding rotation angle and axes about which to rotate to obtain $\mathbf{U}_2$–$\mathbf{U}_{12}$ from $\mathbf{U}_1$.

Variant	**Rotation Angle & Axis**	**Variant**	**Rotation Angle & Axis**
$\mathbf{U}_1 = \begin{pmatrix} \gamma & \varepsilon & \varepsilon \\ \varepsilon & \alpha & \delta \\ \varepsilon & \delta & \alpha \end{pmatrix}$		$\mathbf{U}_7 = \begin{pmatrix} \alpha & -\varepsilon & -\delta \\ -\varepsilon & \gamma & \varepsilon \\ -\delta & \varepsilon & \alpha \end{pmatrix}$	120° (1–11)
$\mathbf{U}_2 = \begin{pmatrix} \gamma & -\varepsilon & -\varepsilon \\ -\varepsilon & \alpha & \delta \\ -\varepsilon & \delta & \alpha \end{pmatrix}$	180° (100)	$\mathbf{U}_8 = \begin{pmatrix} \alpha & \varepsilon & -\delta \\ \varepsilon & \gamma & -\varepsilon \\ -\delta & -\varepsilon & \alpha \end{pmatrix}$	180° (110)
$\mathbf{U}_3 = \begin{pmatrix} \gamma & -\varepsilon & \varepsilon \\ -\varepsilon & \alpha & -\delta \\ \varepsilon & -\delta & \alpha \end{pmatrix}$	180° (010)	$\mathbf{U}_9 = \begin{pmatrix} \alpha & \delta & \varepsilon \\ \delta & \alpha & \varepsilon \\ \varepsilon & \varepsilon & \gamma \end{pmatrix}$	180° (–101)
$\mathbf{U}_4 = \begin{pmatrix} \gamma & \varepsilon & -\varepsilon \\ \varepsilon & \alpha & -\delta \\ -\varepsilon & -\delta & \alpha \end{pmatrix}$	180° (001)	$\mathbf{U}_{10} = \begin{pmatrix} \alpha & \delta & -\varepsilon \\ \delta & \alpha & -\varepsilon \\ -\varepsilon & -\varepsilon & \gamma \end{pmatrix}$	240° (1–11)
$\mathbf{U}_5 = \begin{pmatrix} \alpha & \varepsilon & \delta \\ \varepsilon & \gamma & \varepsilon \\ \delta & \varepsilon & \alpha \end{pmatrix}$	180° (–110)	$\mathbf{U}_{11} = \begin{pmatrix} \alpha & -\delta & \varepsilon \\ -\delta & \alpha & -\varepsilon \\ \varepsilon & -\varepsilon & \gamma \end{pmatrix}$	180° (101)
$\mathbf{U}_6 = \begin{pmatrix} \alpha & -\varepsilon & \delta \\ -\varepsilon & \gamma & -\varepsilon \\ \delta & -\varepsilon & \alpha \end{pmatrix}$	120° (11–1)	$\mathbf{U}_{12} = \begin{pmatrix} \alpha & -\delta & -\varepsilon \\ -\delta & \alpha & \varepsilon \\ -\varepsilon & \varepsilon & \gamma \end{pmatrix}$	240° (11–1)

where

$$\gamma = \frac{a(\sqrt{2}a + c\sin\beta)}{a_0\sqrt{2a^2 + c^2 + 2\sqrt{2}ac\sin\beta}}$$

$$\varepsilon = \frac{1}{\sqrt{2}a_0}\left(\frac{ac\cos\beta}{\sqrt{2a^2 + c^2 + 2\sqrt{2}ac\sin\beta}}\right)$$

$$\alpha = \frac{1}{2\sqrt{2}a_0}\left(\frac{c(c + \sqrt{2}a\sin\beta)}{\sqrt{2a^2 + c^2 + 2\sqrt{2}ac\sin\beta}} + b\right)$$

$$\delta = \frac{1}{2\sqrt{2}a_0}\left(\frac{c(c + \sqrt{2}a\sin\beta)}{\sqrt{2a^2 + c^2 + 2\sqrt{2}ac\sin\beta}} - b\right)$$

In the case of CsH_2PO_4, the variant pairs that form twins satisfied Equation (I.4) for a two-fold rotation and, therefore, Equations (I.6)–(I.7) were used determine the twinning modes. The variant pairs which are not related by a two-fold rotation did not satisfy Equation (I.8), and therefore, do not form twins. The twinning modes are summarized in Table I.4. Compatible variant pairs are denoted by “Y” and incompatible by “N”. The variants pairs $\mathbf{U_1}$–$\mathbf{U_2}$, $\mathbf{U_3}$–$\mathbf{U_4}$, $\mathbf{U_5}$–$\mathbf{U_6}$, $\mathbf{U_7}$–$\mathbf{U_8}$, $\mathbf{U_9}$–$\mathbf{U_{10}}$, and $\mathbf{U_{11}}$–$\mathbf{U_{12}}$ form compound twins, denoted by “C” in the table. An example of the two solutions to the twinning equation (I.5) for the $\mathbf{U_1}$–$\mathbf{U_3}$ variant pair is

$$\mathbf{a} = \left(0.4378, -0.0809, -0.3799\right) \qquad \mathbf{n} = \left(0, 1, 0\right) \tag{I.18}$$

and

$$\mathbf{a} = \left(-0.0709, 0.6285, 0.06380\right) \qquad \mathbf{n} = \left(0.7329, 0, -0.6804\right) \tag{I.19}$$

Table I.4 Allowed twinning modes of CsH_2PO_4 martensite. Y indicates a pair of variants capable of forming a twin boundary, N indicates that a pair of twins cannot form a twin boundary, and C indicates a compound twin.

Variant	**1**	**2**	**3**	**4**	**5**	**6**	**7**	**8**	**9**	**10**	**11**	**12**
1		C	Y	Y	Y	N	N	Y	Y	N	Y	N
2	C		Y	Y	N	Y	Y	N	N	Y	N	Y
3	Y	Y		C	N	Y	Y	N	Y	N	Y	N
4	Y	Y	C		Y	N	N	Y	N	Y	N	Y
5	Y	N	N	Y		C	Y	Y	Y	N	N	Y
6	N	Y	Y	N	C		Y	Y	N	Y	Y	N
7	N	Y	Y	N	Y	Y		C	Y	N	N	Y
8	Y	N	N	Y	Y	Y	C		N	Y	Y	N
9	Y	N	Y	N	Y	N	Y	N		C	Y	Y
10	N	Y	N	Y	N	Y	N	Y	C		Y	Y
11	Y	N	Y	N	N	Y	N	Y	Y	Y		C
12	N	Y	N	Y	Y	N	Y	N	Y	Y	C	

For each solution to the twinning equation, given by Equations (I.6)–(I.7), we can determine whether the twins can form a compatible interface with the austenite phase, using the criteria stated in Equation (I.13). Table I.5 is a summary of the variant pairs that can form an austenite-martensite interface.

Table I.5 CsH_2PO_4 martensite variant pairs that are capable of forming an interface with the austenite phase: Y indicates that an interface between the austenite phase and the twins of a specified variant pair is possible, N indicates that it is not possible, and " / " indicates that twinning boundaries are not allowed so an interface with the austenite phase is not possible.

Variant	**1**	**2**	**3**	**4**	**5**	**6**	**7**	**8**	**9**	**10**	**11**	**12**
1		N	Y	Y	Y	/	/	N	Y	/	N	/
2	N		Y	Y	/	N	Y	/	/	N	/	Y
3	Y	Y		N	/	Y	N	/	N	/	Y	/
4	Y	Y	N		N	/	/	Y	/	Y	/	N
5	Y	/	/	N		N	Y	Y	Y	/	/	N
6	/	N	Y	/	N		Y	Y	/	N	Y	/
7	/	Y	N	/	Y	Y		N	N	/	/	Y
8	N	/	/	Y	Y	Y	N		/	Y	N	/
9	Y	/	N	/	Y	/	N	/		N	Y	Y
10	/	N	/	Y	/	N	/	Y	N		Y	Y
11	N	/	Y	/	/	Y	/	N	Y	Y		N
12	/	Y	/	N	N	/	Y	/	Y	Y	N	

If a pair of variants can form an interface with the austenite phase, there are up to eight ways such an interface can exist, four for each twin type. In the case of CsH_2PO_4, Equation (I.13) is never satisfied for both of the twin types. Therefore, if a solution exists, it is described by 4 rather than 8 vector pairs, **b** and **m.** For the $\mathbf{U_1}$–$\mathbf{U_3}$ variant pair, the austenite-martensite interface is described by Equations (I.20)–(I.23). These four solutions correspond to the Type II twin.

$$\mathbf{b} = \left(0.0667,\ 0.0778,\ 0.2028\right) \qquad \mathbf{m} = \left(-0.9523,\ 0.3042,\ 0.0226\right) \tag{I.20}$$

$$\mathbf{b} = \left(0.2188,\ -0.0585,\ 0.0183\right) \qquad \mathbf{m} = \left(-0.1874,\ -0.3811,\ -0.9053\right) \tag{I.21}$$

$$\mathbf{b} = \left(0.2188,\ 0.0585,\ 0.0183\right) \qquad \mathbf{m} = \left(-0.1874,\ 0.3811,\ -0.9053\right) \tag{I.22}$$

$$\mathbf{b} = \left(0.0667,\ -0.0778,\ 0.2028\right) \qquad \mathbf{m} = \left(-0.9523,\ -0.3042,\ 0.0226\right) \tag{I.23}$$

Although 42 variant pairs can form martensite twins, only 24 can form austenite-martensite interfaces, resulting in a total of 96 solutions. It should be noted that the variant pairs that form compound twins in monoclinic CsH_2PO_4 cannot form an interface with the cubic austenite phase.

Appendix J Microstructure of Solid Acid Compounds: Supplemental

J.1 Additional Images

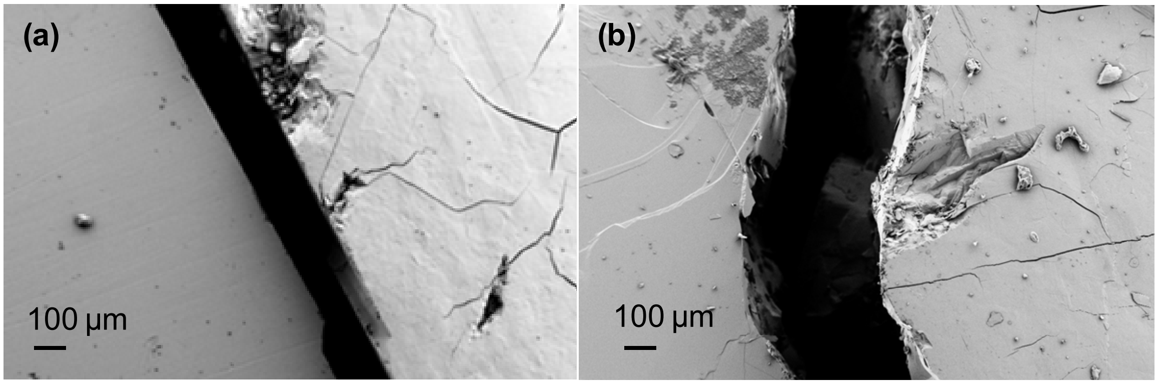

Figure J.1 SEM micrographs of CsH_2PO_4 single crystals, side by side, before and after heat treatment to superprotonic temperatures. Crystal surfaces were prepared by either (a) uni-directional polishing or (b) fracture, then broken in half. For each image, the surfaces on the left and right correspond to two halves of the crystal, before and after heat treatment, respectively.

Figure J.2 SEM micrograph of a polished CsH_2PO_4 single-crystal showing features (running from upper-left to lower-right of image) that appear after heating to superprotonic temperatures. Polishing lines run along a different direction (lower-left to upper-right).

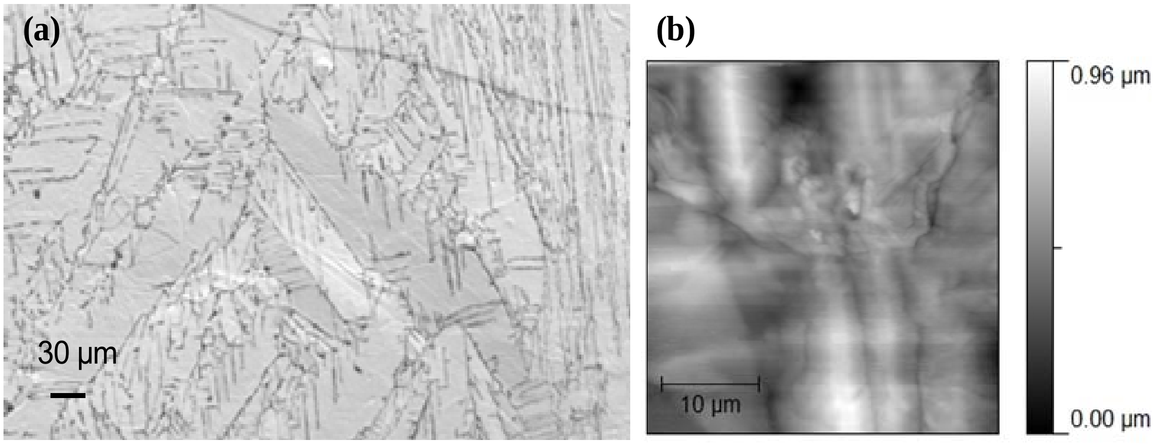

Figure J.3 (a) SEM micrograph of polished $CsHSO_4$ surface after heating to 155 ºC in ambient air, and (b) AFM image of a fractured $CsHSO_4$ surface at 149 ºC. Image was taken after ~ 5 h at superprotonic temperatures and still reveals twinning.

Appendix K Pt | CsH_2PO_4 | Au as a Mixed Potential Hydrogen Sensor

K.1 Introduction

Solid state electrochemical sensors have been developed for the detection of a wide variety of gases, including H_2, CO, NO_x, and hydrocarbons.[128–129] Potentiometric sensors offer several advantages over amperometric sensors since generated voltages across potentiometric cells are independent of sensor dimensions. Furthermore, potentiometric sensors that are governed by the mixed potential effect[130–131] can generate a measurable voltage in a single uniform gas, allowing for simpler operation and design. The mixed potential effect has been discussed in literature in the context of both dual chamber and single chamber mode. In the dual chamber mode, evidence of the mixed potential effect was the observation of open-circuit voltages deviating from the computed Nernst voltage[132–133] while in the single chamber mode, a measurable voltage can be generated when using dissimilar electrodes.[131, 134–138]

The response behavior of the mixed potential has been shown to depend on the kinetics of the electrochemical reactions at hand, for example, whether the reaction kinetics are limited by charge transfer or mass transport.[130–131, 139] Consequently, the characteristics of a mixed potential sensor are governed by a large number of parameters including environmental factors such as gas composition and temperature as well as sensor characteristics such as the choice of electrolyte and electrode. What is more, electrode properties such as surface area, microstructure, and activity for the sensing gas play a significant role in the sensor response. In this work, we demonstrate the mixed potential effect for a sensor based on the solid acid electrolyte, CsH_2PO_4.

K.2 Mixed Potential Effect

In uniform H_2-H_2O-Ar atmospheres, H_2 and H_2O can reach equilibrium via the reaction

$$H_{2(g)} + 1/2\, O_{2(g)} \rightleftharpoons H_2O_{(g)} \tag{K.1}$$

However, in the presence of an electrode | electrolyte interface, the following reactions can proceed:

$$H_{2(g)} \rightleftharpoons 2H^+ + 2e^- \tag{K.2}$$

$$1/2\, O_{2(g)} + 2H^+ + 2e^- \rightleftharpoons H_2O_{(g)} \tag{K.3}$$

with the electrons generated by (K.2) being consumed by (K.3). Graphically, this is depicted by the intersection of the current-voltage curves for (K.2) and (K.3), as shown in Figure K.1a. (Note that Equations (K.2) and (K.3) also apply in H_2-H_2O-air atmospheres.) At the point of intersection, the reducing and oxidizing currents on a given metal electrode are equal, resulting in what is termed the mixed potential, denoted as E_{Au} and E_{Pt} for Au and Pt metals, respectively. The difference between the mixed potential established at each metal corresponds to the voltage measured across the Pt | electrolyte | Au cell. A change in the gas composition causes a shift in the curves (Figure K.1a) and therefore a change in the voltage measured across the cell. As evident in Figure K.1, the voltage existing across the cell depends on the shape of the current-voltage curves. Therefore, it is common to use metals with sufficiently differing activities for the electrochemical reactions of interest as this would yield the largest difference in mixed potential across the two metals. It is important to note that, depending on the gas environment, additional reactions can contribute to the mixed potential effect.

Because the mixed potential is established by kinetics, electrode microstructure and geometric factors play a role in the response by changing the net current that can flow at each metal. For example, in Figure K.1b, we schematically show the effect of mass transport limitations (for oxygen gas, in this case). A shift in the current-voltage curves due to a gas composition change results in a different voltage response than in the case of no mass transport limitations (Figure K.1a).

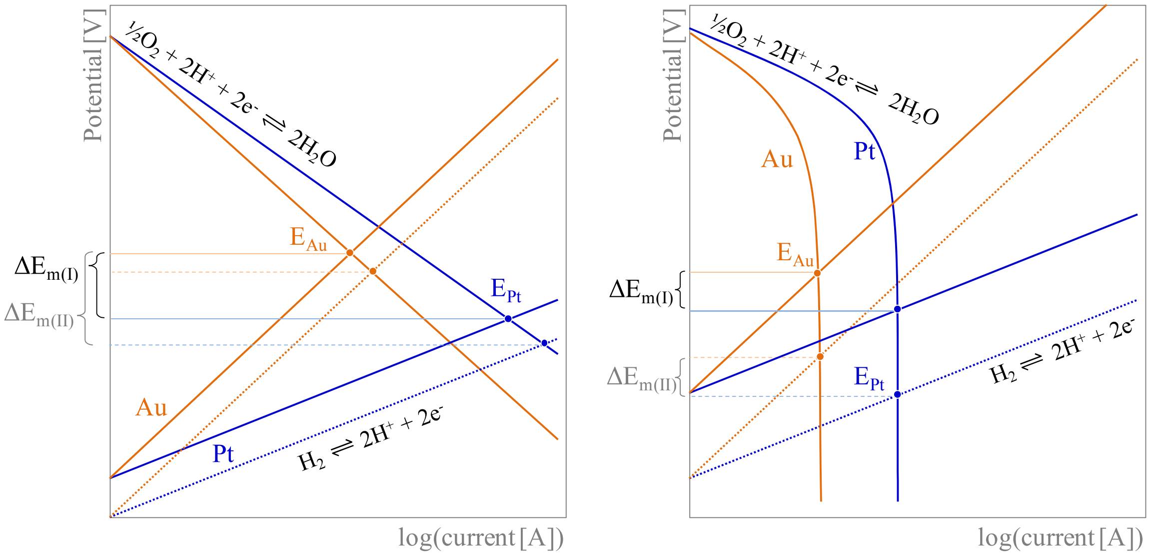

Figure K.1 Schematic polarization curves for determining mixed potentials (a) with and (b) without mass transport limitations. E_{Au} and E_{Pt} denote the mixed potentials established at each metal, and ΔE_m corresponds to the voltage measured across the sensor. Subscripts I and II denote before and after a shift in the gas composition (or current-voltage curves).

K.3 Experimental

CsH_2PO_4 powders were prepared from aqueous solutions of Cs_2CO_3 (99.9%, Alfa Aesar, 12887) and H_3PO_4 (85%, Mallinckrodt, 2796). The resulting solution was added to methanol to induce rapid precipitation, and the precipitate was dried at 100 ºC. The powder was uni-axially pressed (491 MPa for 20 min) into polycrystalline CsH_2PO_4 discs 9.3 mm in dia. and ~ 1 mm thick. Disc surfaces were mechanically polished (grit size 600) before deposition of Pt and Au films. Sensors were prepared by sputtering Au and Pt films (AJA International) on opposing sides of CsH_2PO_4 discs which were masked at its edges by tape during deposition. The sputtering time was controlled to obtain metal films ~ 75 nm thick.

Electrical contact to the metal films was made by sandwiching the cell between two sheets of Toray carbon paper which, in turn, were mechanically contacted to silver ring current collectors. The response behavior of the sensor was examined at 235 ºC under uniform H_2-Ar-H_2O atmospheres with a total flow rate of 200 mL min^{-1}. The hydrogen partial pressures examined, 0.0005–0.5 atm, were achieved by mixing appropriate flow rates of 100%, 2%, and 0.1% H_2 gas (ultra-high purity grade with Ar balance) via calibrated digital mass flow controllers. A water partial pressure of ~ 0.5 atm was maintained by bubbling inlet H_2-Ar through a heated water bath and monitored by a humidity sensor (Rotronic Instrument Corp.). The open-circuit voltage of the cell was measured using a Keithley 617 electrometer.

For each composition examined, appropriate flow rates of 100, 2, and/or 1% H_2 in Ar were used. Due to limitations in the reactor design, these gases were not pre-mixed before entering the reactor. Between measurements of the sensor response for each hydrogen partial pressure (values between 0.001 and 0.5 atm), the gas composition was returned to baseline of 5 × 10^{-4} atm H_2.

Films before and after sensor characterization were examined by scanning electron microscopy (LEO 1550VP, Carl Ziess SMT) and X-ray diffraction (Phillips X'Pert Pro). Film characteristics are typical of those reported for Pt thin films (Chapter 3 and Appendix C) and, therefore, are not shown here.

K.4 Results and Discussion

K.4.1 Sensor Response

The response of the Pt | CsH_2PO_4 | Au sensor is shown in Figure K.2 in which each feature corresponds to the change in cell voltage due to a different hydrogen partial pressure, as labeled. The measured voltage is greater at lower partial pressure, with the baseline pH_2 of 5 × 10^{-4} atm H_2 yielding a voltage over –200 mV. At the highest pH_2 of 0.5 atm, the open-circuit voltage is approximately –20 mV. Given the cell configuration employed (which the positive lead of the electrometer attached to Pt), the negative voltages measured implies that the mixed potential established at Pt is lower than that at Au.

The lack of reproducibility in the shape of the transient response is likely due to the low gas velocities used, that is, despite the large volumetric flow rate of 200 mL min^{-1}, the gas velocity near the sensor was ~ 16 cm min^{-1} due to the large cross-section of the reactor. At low pH_2 levels, the response overshoots before reaching to the steady-state value when pH_2 is increased from or decreased back to the baseline value. At high pH_2 levels, the response appears to be more stable, displaying a small overshoot and a gradual increase to the steady-state value when the pH_2 is increased from the baseline value. On return to the baseline value, the voltage decays gradually. There is no apparent correlation between the observed transient behavior and the gas source used (i.e., mixture of 100, 2, and/or 0.1% H_2) to obtain the desired composition. Thus, the most plausible explanation is that compositional variations in the gas stream, due to poorly mixed source gases, cause fluctuations in the measured voltage.

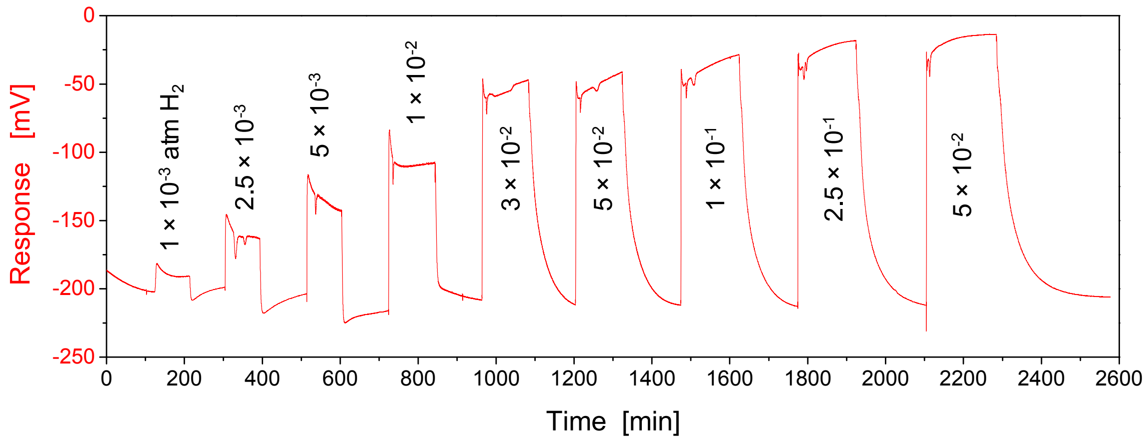

Figure K.2 Plot of measured open-circuit voltage (response) as a function of time for a Pt | CsH_2PO_4 | Au sensor at 235 ºC in H_2-H_2O-Ar atmospheres with 0.5 atm H_2O and various hydrogen partial pressures (as labeled). The baseline composition was arbitrarily set to 5×10^{-4} atm H_2.

Steady-state values of the response, estimated by extrapolation from Figure K.2, are plotted in Figure K.3. The response, as indicated previously, ranges between –200 mV and –20 mV for hydrogen partial pressures spanning three orders of magnitude (0.0005–0.5 atm pH_2). There appears to be two distinct regimes; the slope of the plot is ~ 75 mV dec^{-1} for $pH_2 < 0.01$ atm and ~ 23 mV dec^{-1} for $pH_2 > 0.01$ atm, indicating a higher sensitivity to gas compositions at lower hydrogen partial pressures.

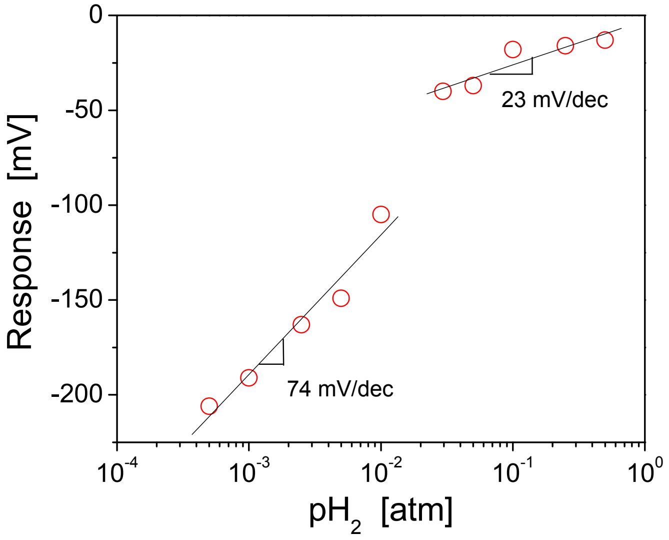

Figure K.3 Mixed potential response of Pt | CsH_2PO_4 | Au sensor for various hydrogen partial pressures at 235 °C in H_2-H_2O-Ar atmospheres with 0.5 atm H_2O. This plot corresponds to data shown in Figure K.2.

An abrupt change in the measured voltage (plotted against composition) is commonly attributed to mass transport limitations.[130] Depicted in Figure K.4 is the case in which both oxygen reduction and hydrogen oxidation are limited by mass transport, the former being true for all compositions and the latter when low hydrogen partial pressures are employed. At relatively high pH_2, the limiting current is higher and, therefore, the mixed potential occurs outside of the mass transport limited regime for hydrogen oxidation. However, as pH_2 is lowered, a sudden jump in the mixed potential occurs, as depicted between E_{m2} and E_{m3}, with the latter potential lying within the mass-transport limited regime.

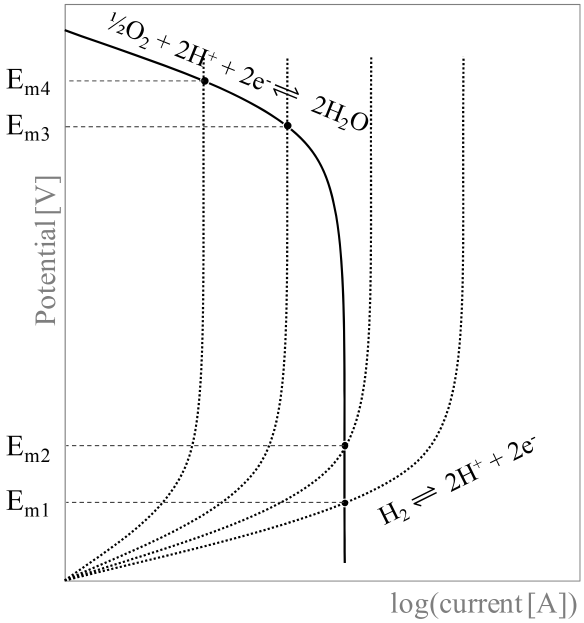

Figure K.4 Schematic showing how mass transport limitations can result in a large change in the mixed potential for a small change the gas composition. E_{m1}–E_{m4} indicate the mixed potentials established on a metal as the pH_2 gas composition is varied.

Additional tests reveal large variations in the response. Shown in Figure K.5 are data for two additional cells, plotted alongside data from Figure K.3 (denoted as HS-CDP07). Figure K.5 shows that not only do different samples yield drastically different responses, but even a given cell, tested on two different days (HS-CDP07, expt 1 vs. expt 2), yields significantly different results. Figure K.6 is a voltage-time plot corresponding to HS-CDP09 (Figure K.5). Immediately clear are differences in the transient behavior compared to that in Figure K.2; the steady-state values are attained relatively quickly, indicating faster response times. Furthermore, the measured voltages are close to zero (–1 mV) for a large range of partial pressures.

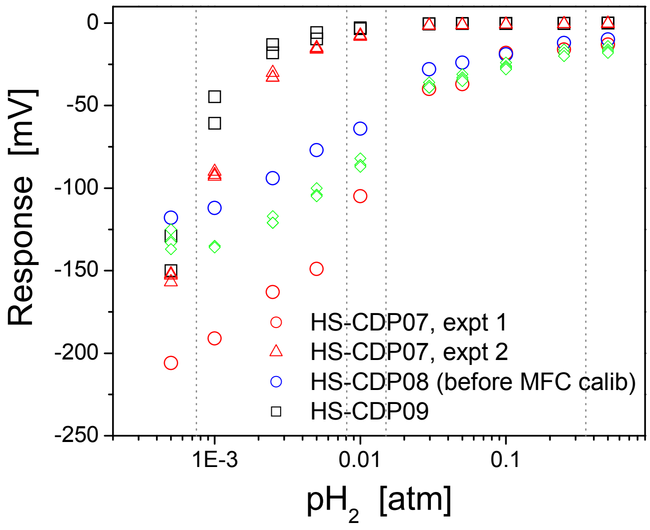

Figure K.5 Mixed potential response of various Pt | CsH_2PO_4 | Au sensors for varying hydrogen partial pressures at 235 °C in H_2-H_2O-Ar atmospheres with 0.5 atm H_2O. Dotted lines indicates a change the gas source used to obtained the desired partial pressure.

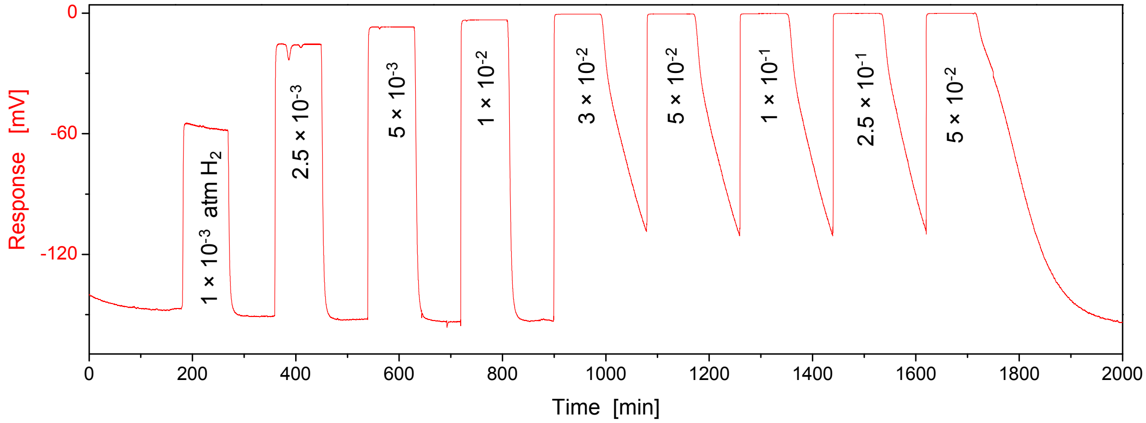

Figure K.6 Plot of measured open circuit voltage (response) as a function of time for a Pt | CsH_2PO_4 | Au sensor (HS-CDP09 in Figure K.5) at 235 °C in H_2-H_2O-Ar atmospheres with 0.5 atm H_2O and various hydrogen partial pressures (as noted). The baseline composition was set to 5×10^{-4} atm H_2.

K.4.2 Variability in the Sensor Response

Poor mixing of gases (due to low gas velocities), while expected to influence the transient response, should not cause irreproducibilities in the steady-state voltage across the cell. The observed variability in the Pt | CsH_2PO_4 | Au sensor response is most likely due to microstructural variations in the films which can influence both response time and the mixed potential.

Mass transport effects may also play a role. The gas atmosphere contains high hydrogen and water contents and therefore an extremely low oxygen concentration (significantly lower than the lowest pH_2 used in this study). Thus, small fluctuations in pO_2, due to leaks and/or changes in the H_2 and H_2O content, may influence the value of the mixed potential. Moreover, the low pO_2 levels in the system mean that O_2 is mass transport limited and the reaction shown in (K.3) lies far to the left. It should be noted that although the gas flow rate is kept constant for the data presented in this work, observation of changes in the sensor response with gas flow rate (not shown) indicates that mass transport limitations play a role. The water partial pressure changes by a maximum amount of 0.03 atm when the gas composition is changed (most notable when the gas atmosphere is switched from the low-pH_2 baseline composition to a high pH_2 composition) due to variations in the amount of water vapor that Ar and H_2 gases collect during passage though the water bubbler. For pH_2O fluctuations about a set point value of 0.5 atm used in this study, the sensitivity to water vapor content was negligible.

K.5 Summary and Recommendations

We have established that, at temperatures relevant for solid acid electrolytes, the mixed potential effect can be observed. In inert environments, larger voltages (approximately –200 mV) were measured at lower hydrogen partial pressures. The sensor response appeared to be irreproducible across samples and even within the same sample; this is attributed to microstructure variations.

Future studies should be carried out with small reactors with low cross-sectional area. Given the results of Chapter 3, metal films need not be 75 nm. Improved response times may result from thinner (~ 10 nm) films for which the equilibration of hydrogen within the film is minimized. Also, it is possible to use particulate electrodes, for example, carbon powder, rather than the relatively expensive Au as the relatively inert electrode.

It is important to note that sensing of H_2 in air is more practical as this is most likely the environment in which a sensor would operate. In this case, for safety reasons, it is necessary to keep the hydrogen partial pressures relatively low. Measurements in a balance of air are expected to yield a different sensor response from those in inert atmospheres due to the significantly higher oxygen content compared to that established by H_2-H_2O mixtures. Furthermore, the higher oxygen content may lead to more reproducible sensor responses. Note that for operation in air, it is necessary to consider additional reactions that may contribute to the mixed potential. For example, it has been suggested that the electrochemical oxidation of metal (for example, Pt via the reaction, $\mathrm{Pt_{(s)} + H_2O_{(g)} \rightleftharpoons PtO_{(s)} + 2H^+ + 2e^-}$) can participate in establishing the mixed potential.